THE SCATTERING AND ABSORPTION OF LIGHT BY AEROSOL PARTICLES: MEASUREMENT AND MODELLING

by
Julia Marshall

SUBMITTED IN PARTIAL FULFILLMENT OF THE
REQUIREMENTS FOR THE DEGREE OF
DOCTOR OF PHILOSOPHY

AT

DALHOUSIE UNIVERSITY
HALIFAX, NOVA SCOTIA
OCTOBER, 2005

Your file Votre référence
ISBN: 978-0-494-16699-4
Our file Notre référence
ISBN: 978-0-494-16699-4

DALHOUSIE UNIVERSITY

To comply with the Canadian Privacy Act the National Library of Canada has requested that the following pages be removed from this copy of the thesis:

Preliminary Pages

Examiners Signature Page (pii)

Dalhousie Library Copyright Agreement (piii)

Appendices

Copyright Releases (if applicable)

Table of Contents

List of Tables

List of Figures

Abstract

In July, 2002, atmospheric aerosol measurements were conducted over the north-east Pacific Ocean. The size distribution and size-segregated chemical composition of the aerosols were measured, along with scattering and backscattering coefficients at three wavelengths, and the absorption coefficient at one wavelength. Using Mie theory to calculate the aerosol scattering and absorption coefficients from the size distribution and chemical measurements, closure with the measured scattering coefficients is not attained. Discrepancies exist between the calculated and measured scattering and backscattering coefficients because the nephelometer measures scattering only between 7°and 170°, largely missing the prevalent forward-scatter lobe from coarse aerosols. During this study the majority of the total scattering and backscattering in the marine boundary layer of this region was from coarse particles consisting mostly of sea salt. To examine scattering at higher altitudes in the marine environment, another closure study was carried out based upon measurements taken during five flights in October, 2003, over the waters surrounding Nova Scotia. The same quantities were measured, with the exception of the absorption coefficient. In this case closure is attained for more than 70% of the total scattering measurements, but is not attained for the backscattering coefficients. Coarse particles are found to account for roughly half of the total scattering and 70% of the backscattering for altitudes up to ~1000 m. The contribution of coarse particles calculated from on-board measurements is underestimated due to substantial inlet losses for particles larger than 2 μm. The final part of the thesis involves the modelling of absorption by black carbon (BC) particles within cloud droplets. Based upon the volume fraction of activated BC, the effective radius of the cloud, and the wavelength band, the single-scattering albedo of the cloud is calculated. The Maxwell-Garnett mixing rule is used to calculate the index of refraction of the composite droplet. These results are compiled in a look-up table of representative values, which is tested using a 1-D radiation model.

List of Acronyms

AGCM - Atmospheric General Circulation Model
AMS - Aerosol Mass Spectrometer
APS - Aerodynamic Particle Sampler
BC - black carbon or soot
CCCma - Canadian Centre for Climate Modelling and Analysis
CCN - cloud condensation nuclei
C-SOLAS - Canadian Surface Ocean Lower Atmosphere Study
CW-CRD - Continuous Wave Cavity Ring-Down
FSSP - Forward Scattering Spectrometer Probe
HYSPLIT - HYbrid Single-Particle Integrated Trajectory
LWC - Liquid Water Content
MOUDI - Multiple Orifice Uniform Deposit Impactor
MSA - Methanesulfonic acid
MSC - Meteorological Service of Canada
OD - outer diameter
PCASP - Passive Cavity Aerosol Spectrometer Probe
PSAP - Particle Soot Absorption Photometer
SERIES - Subarctic Ecosystem Response to Iron Enrichment Study
SMPS - Scanning Mobility Particle Sizer
SSM/I - Special Sensor Microwave Imager
UTC - Coordinated Universal Time

List of Symbols

BC_y - soluble black carbon

c - correction factor

C_x - scattering, absorption or extinction cross section, depending on subscript [m^{-2}]

D_a - aerodynamic diameter of the particle [μm]

D_g - geometric diameter of the particle [μm]

f - volume fraction of black carbon to water

F - fraction of cloud droplets containing absorbing aerosols

F_x - irradience, either incident or transmitted, depending on subscript [W m^{-2}]

HGF - hygroscopic growth factor

k - imaginary coefficient of index of refraction

λ - wavelength of incident radiation

m - complex index of refraction in air

N - complex index of refraction in vacuo

n - real part of index of refraction

Q_x - efficiency of scattering, absorption or extinction, depending on subscript

RH - relative humidity [%]

ρ - density [g m^{-3}]

σ_x - coefficient of scattering, absorption or extinction, depending on subscript [m^{-1}]

x - size parameter

ω - single-scattering albedo

$\overline{\omega}$ - single-scattering co-albedo

Acknowledgements

I would like to begin by thanking my supervisor, Ulrike Lohmann, for introducing me to the field of atmospheric science, and communicating a real excitement about research. She was incredibly reliable at providing prompt, thoughtful feedback, especially impressive as I was often requesting this help while pushing deadlines to the limit, and while separated from her by many time zones.

I would also like to thank Richard Leaitch for the opportunity to take part in the field campaigns which provided the data for my thesis. I benefitted greatly from the practical training, as well as from Richard's considerable experience in organizing field campaigns and working with the data afterward. He was also very good about meeting with me to discuss my problems no matter where I happened to track him down.

My other committee member, Tom Duck, provided helpful feedback on the written thesis, particularly in discussing statistical analysis and uncertainties. My external examiner, Norm O'Neill, also contributed excellent suggestions, improving the overall thesis in the process. His fresh set of eyes was able to pick up on problems that I could no longer even begin to see.

Nicole Shantz, Lisa Phinney and Pam Lehr, all of whom took part in the field campaigns with me, certainly deserve to be recognized. In addition to their work in the field they were all willing and able to help me with data processing and editing, and they made the whole process much more fun.

I would also like to acknowledge the good folks out at CCCma in Victoria, notably Knut von Salzen, for providing me with a place to work and people to work with while I "visited" during the past year.

On a more personal level, I'd like to thank my family for their support throughout, even supplying a cheering section at my defence. And finally, Jeremi, for providing me with unfailing understanding and patience, not to mention hot meals at all hours of the night, throughout the long process of writing up.

Chapter 1

Introduction

1.1 Aerosols and Climate

Aerosols are particles of submicron to micron scale, of solid or liquid composition, suspended in the atmosphere. They are of both natural and anthropogenic origin, with concentrations ranging from tens of particles per cm^3 at the surface for a pristine marine atmosphere to $\sim 10^4$ cm^{-3} in urban regions. Typical composition includes sulfate, sea salt, dust, black carbon, nitrate, and organic carbon. Aerosol particles are of climatic interest due to their ability to influence the radiative budget through a variety of effects, both directly and indirectly.

Aerosols may scatter incoming shortwave radiation back to space, thereby reducing the radiation incident at the surface and cooling the atmosphere. This is known as the direct effect of aerosols. Some aerosols, such as black carbon (BC) or dust, absorb shortwave radiation in addition to scattering it, which also reduces the radiation at the surface while causing local heating This can have complex feedbacks on the formation and lifetime of clouds which are dependent upon the location of the aerosol layer, leading to either an increase or decrease in the liquid water content of low clouds [Johnson et al., 2004, Penner et al., 2003]. As such, the sign of this forcing is not even certain, and can change based upon the assumptions made. The effect of the absorbing aerosol on the surrounding clouds is known as the semi-direct effect of aerosols [Hansen et al., 1997].

In addition to their radiative impact as particles suspended in air, aerosol particles can also affect radiative balance through their role as cloud condensation nuclei (CCN). When water condenses onto an aerosol particle to form a cloud droplet, that aerosol is said to be activated, and is acting as a CCN. If, in a region with relatively few aerosols (such as the marine boundary layer), the number of available CCN increases but the total amount of condensate is unchanged it can result in a

cloud with a greater number of smaller cloud droplets. This reduction in cloud droplet radius leads to an increase in the albedo of the cloud, resulting in a cooling effect as more shortwave radiation is reflected. This is known as the first indirect effect or the Twomey effect [Twomey, 1977]. The reduced cloud droplet radius of the first indirect effect might also lead to the suppression of precipitation and an increase in cloud lifetime, known as the second indirect effect or the cloud lifetime effect [Albrecht, 1989]. This is also a cooling effect, as an increase in cloud lifetime increases the amount of radiation reflected by the clouds.

Some activated aerosols (aerosols acting as CCN) may affect the radiative balance in yet another way if they contain an optically absorbing material, such as BC or dust. These particles, while acting as CCN, may absorb solar radiation, thus leading to a heating of the surrounding air and the evaporation of cloud droplets. While all absorbing aerosols can lead to local heating, the location of the aerosols within the cloud droplet may enhance this effect. In fact, Chýlek et al. [1996] have found the specific absorption of BC within a cloud droplet to be 2-2.5 times greater than that of unactivated BC aerosols. As such, the effect of black carbon within cloud droplets may contribute significantly to aerosol climate effects.

1.2 Measurement and Modelling of Aerosol Optical Properties

Because of their short temporal and spatial scales and variable composition it is very difficult to characterize global aerosol fields. Since measurements of aerosols are generally limited in spatial and/or temporal scales, numerical models of aerosol optical properties are often the only practical way to assess present-day global aerosol radiative effects. They also provide a basis for the estimation of aerosol effects in the past or future based upon emission scenarios.

Measurements of ambient aerosols allow for estimates to be made regarding the input of aerosol fields into climate models. In addition to this, reliable measurements from field campaigns allow for comparison between measured parameters and those computed from models. Thus the model may be tested against the measured data in order to evaluate the model's performance in the reproduction of the optical properties of ambient aerosols. This comparison is a sort of "closure test"

[Quinn et al., 1996]. An agreement between the model and the measurements indicates that the model reasonably represents the observed system, and closure is attained. This agreement allows for greater confidence in both the accuracy of the measurements and the reliability of the model, while a lack of agreement indicates that the situation must be further examined.

If such studies are carried out on a variety of distinct regional aerosol types, both with and without anthropogenic influence, they can allow for a greater confidence in calculating the radiative impact of aerosols, as well as constraining the uncertainties associated with these calculations. This can provide a greater degree of confidence when estimating the radiative impact of aerosols on past, present and future climates.

The two main types of optical closure studies are point closure and column closure. In the former, measurements and calculations at one point in time and space are compared for consistency. In the latter, measurements along a vertical profile are required, as well as an independent measurement or calculation of total or layer aerosol optical depth. In order to carry out a point optical closure study for the scattering and absorbing properties of the aerosols it is necessary to have direct measurements of the optical properties of the aerosol, the number size distribution, the size-distributed chemical composition, and the ambient temperature and relative humidity [Fridlind and Jacobson, 2003]. Such measurements were collected as part of both a research cruise and a series of research flights in marine environments, and these data are analyzed for optical closure as part of this thesis.

1.3 Modelling Absorption due to Activated Black Carbon

While a number of studies have attempted to estimate the global magnitude and direction of the semi-direct effect considering only non-activated BC [Cook and Highwood, 2004, Lohmann and Feichter, 2001, e.g.], not as much work has been done looking at the impact of BC within cloud droplets. Chýlek et al. [1996] examined the possibility that BC in cloud droplets was responsible for the measured "anomalous absorption" by clouds (eg. Pilewskie and Valero [1995], Stephens and Tsay [1990]), on the order of 20-30 W m^{-2}. Though their estimates for BC content

within a droplet indicated that the decrease in cloud albedo due to the presence of BC could not account for the large difference in calculated and measured absorption, they estimated that it could contribute a few (1-3) W m^{-2}. Chuang et al. [2002] parameterized the effect of BC absorption within clouds in a GCM, using carbon fields to determine the BC content within the cloud droplets, and found the effect to be largely localized around BC sources, around which there was a warming of 0.7 W m^{-2}.

The present work attempts to analyze the effect of BC within cloud droplets, and to assess how this might contribute to the aerosol semi-direct effect.

1.4 Statement of Purpose

As the oceans cover most of the surface of the earth, a good characterization of marine aerosols is necessary to develop a reasonable assessment of the role of aerosols in our climate. Sea salt is ubiquitous in these regions, and dominates the aerosol contribution to clear-sky albedo in marine environments [Haywood et al., 1999]. Scattering by aerosols also has a stronger climatic impact over the low surface albedo of the ocean than over surfaces with higher albedos [Penner et al., 2003]. Studying pristine marine environments can also provide a baseline against which anthropogenically influenced regions may be compared.

In July 2002 a research cruise took place in the northeast Pacific as part of an iron-enrichment experiment through C-SOLAS (Canadian Surface Ocean Lower Atmosphere Study). On board the ship were a suite of instruments measuring a wide variety of aerosol characteristics, including optical properties. This dataset provides the necessary tools to measure the optical properties of aerosol particles in this remote marine environment, and to test these measurements against the optical properties calculated using Mie scattering theory with the measured size, number and composition of the aerosols.

However, these measurements were all taken near the surface, and give little insight into the optical properties of the marine aerosol throughout the column. For analysis of the scattering properties as a function of altitude it is necessary to look to data measured along a profile, such as that from the SOLAS flight campaign

in October 2003.

Six project flights were carried out from October 13 to 17, 2003, above the waters surrounding Nova Scotia. The research platform was the National Research Council's Institute for Aerospace Research Convair 580. Measurements were taken in and around marine stratocumulus, at altitudes as low as 150 m above sea level. A variety of aerosol instruments were on board the aircraft, providing similar measurements to those on board the research cruise, with the exception of the absorption coefficient of the aerosols. Again, an optical closure study can be undertaken, this time looking at the change in contribution to scattering coefficients as a function of altitude.

Particularly in the case of the shipborne measurements, these data describe primarily natural aerosols with very weak absorptive properties. In contrast, other regions have much higher incidences of absorptive, optically dark aerosols such as dust, both natural and anthropogenic, and BC or soot, from fossil fuel combustion and biomass burning. It is estimated that more than half of the submicron mass of aerosol particles is anthropogenic, principally sulfate and carbonaceous aerosols from fossil fuel combustion and biomass burning [Seinfeld and Pandis, 1998].

BC is produced only through combustion, and most of the emissions are initially hydrophobic, estimated at 80% [Croft et al., 2005]. Over time, compounds may become attached to the surface of the BC aerosol, increasing its solubility. This process is known as ageing. Once the BC particle is aged it is able to become activated and act as a CCN, resulting in cloud droplets containing small amounts of BC. Its presence within a cloud droplet may increase the amount of solar radiation that the BC is able to absorb per unit mass [Chýlek et al., 1996], which may speed the dissipation of the cloud through local heating.

In order to examine the contribution of activated BC to the semi-direct aerosol effect it is important to determine (1) how much BC is assumed to be activated and (2) what effect this may have on the radiative properties of the cloud. In this work, the former is estimated based upon the volume of hydrophylic BC predicted from the condensation-coagulation-oxidation ageing scheme of Croft et al. [2005], while the latter is an adaptation of a method developed by Chuang et al. [2002], which

in turn is derived from work by Chýlek and Videen [1998].

From this, a look-up table is derived to assess the perturbation in the single-scattering albedo (ω) of the cloud due to the presence of the activated BC, based upon (a) the volume ratio of BC to water, (b) the effective radius of the cloud droplets, and (c) the wavelength of light. The effect of this table is first assessed within one dimensional radiation models based upon the scheme of Dobbie et al. [1999], which is that used in the CCCma AGCM (Canadian Centre for Climate modelling and analysis Atmsopheric General Circulation Model).

1.5 Research Outline

Following this introductory chapter is a review of some of the theory behind the direct aerosol effect, and an introduction to Mie scattering. In the third chapter the data from the research cruise in the northeast Pacific are introduced, and the fourth chapter outlines the optical closure study carried out upon these data. The fifth chapter introduces the data collected during the research flights over the waters surrounding Nova Scotia, and the sixth chapter looks at the analysis of these data for optical closure. The seventh chapter introduces the problem of absorbing aerosols within cloud droplets, and outlines the modelling of this phenomenon and the development of a look-up table describing its effects on the single-scattering albedo of a water cloud. Chapter eight outlines the implementation of the look-up table in the one-dimensional radiation model, with sensitivity tests. Finally, the conclusions of this thesis are included in chapter nine.

Chapter 2

The Direct Effect

When radiation is incident upon a particle, the electric charges within the particle begin to oscillate through excitation. Some of this energy may be converted into heat through absorption, while some is reradiated in different directions through scattering. For spherical particles of known composition the exact nature of this scattering and absorption, known collectively as extinction, can be solved explicitly.

If we consider the spectral irradiance of a collimated beam of incident radiation (in W m^{-2} μm^{-1}), F_0, the spectral energy lost to absorption, due to a single particle, is given by Equation 2.1:

$$\tilde{F}_{abs} = C_{abs} F_0, \tag{2.1}$$

where $\tilde{F}_{abs}$ is in W μm^{-1} and C_{abs} is the absorption cross section, in m^{-2}. Likewise the energy lost to scattering, $\tilde{F}_{scat}$, is proportional to the incident irradiance and the scattering cross section, C_{scat}:

$$\tilde{F}_{scat} = C_{scat} F_0 \tag{2.2}$$

The extinction cross section of the particle, C_{ext} is then given as the sum of the scattering and absorption cross sections:

$$C_{ext} = C_{scat} + C_{abs} \tag{2.3}$$

Though sharing the name and units of the geometrical cross section, the extinction cross section can be much greater or less than the area of the particle's profile, depending upon the properties of the particle, the medium in which it is suspended, and the wavelength of the incident radiation. A unitless efficiency is derived by dividing the extinction cross section by the geometrical cross-sectional area of the sphere, A, as shown in Equation 2.4:

$$Q_{ext} = \frac{C_{ext}}{A} = \frac{C_{scat}}{A} + \frac{C_{abs}}{A}, \tag{2.4}$$

with the two latter terms being expressions of the scattering and absorption efficiencies, Q_{scat} and Q_{abs}, respectively.

Based upon the ratio of the diameter of the particle, D_g, to the wavelength of the incident radiation, λ, and the complex index of refraction of the particle and the medium, N and N_0 respectively, these efficiencies may be computed through the use of Mie scattering theory, also known as Mie-Debye-Lorenz theory [Seinfeld and Pandis, 1998].

Though the complex index of refraction of the particle, $N = n + ik$, as well as that of the non-absorbing medium, N_0, are required, the medium in question is the atmophere, where N_0 essentially equals unity. As such, the normalized form of $m = \frac{N}{N_0}$ shall be used to describe the complex index of refraction of the particle hereafter.

The mathematical formalism of Mie theory is a solution to the problem for elastic scattering involving all values of D_g and λ, but the problem can be simplified for certain cases. These are grouped according to the magnitude of the dimensionless size parameter, x, defined as the ratio of the particle's circumference to the wavelength of the light:

$$x = \frac{\pi D_g}{\lambda} \tag{2.5}$$

When $x << 1$, the Rayleigh regime applies, governing such things as the scattering of visible light off of air particles, the reason why the sky appears blue. When $x >> 1$, the geometric scattering regime applies, which can explain the appearance of such optical phenomena as parahelia and rainbows due to the scattering of visible light off of ice crystals and rain droplets, respectively. However when $x \sim 1$, only Mie theory applies. It is this last category which is relevant for scattering of shortwave radiation (λ from 0.3-5 μm) by aerosol particles (D_g from 0.01 μm to a few μm).

The scattering and absorption efficiencies can be calculated exactly based upon Equations 2.6 and 2.7:

$$Q_{scat}(m, x) = \frac{2}{x^2} \sum_{k=1}^{\infty} (2k + 1)[|a_k|^2 + |b_k|^2] \tag{2.6}$$

$$Q_{abs}(m,x) = \frac{2}{x^2}\sum_{k=1}^{\infty}(2k+1)Re[a_k + b_k] \tag{2.7}$$

where a_k and b_k are defined according to:

$$a_k = \frac{x\psi_k\prime(y)\psi_k(x) - y\psi_k\prime(x)\psi_k(y)}{x\psi_k\prime(y)\zeta_k(x) - y\zeta_k\prime(x)\psi_k(y)} \tag{2.8}$$

$$b_k = \frac{y\psi_k\prime(y)\psi_k(x) - x\psi_k\prime(x)\psi_k(y)}{y\psi_k\prime(y)\zeta_k(x) - x\zeta_k\prime(x)\psi_k(y)} \tag{2.9}$$

where $y = xN$, and the functions $\psi_k(z)$ and $\zeta_k(z)$ are the Riccati-Bessel functions [Watson, 1944]. These are given in Equations 2.10 and 2.11:

$$\psi_k(z) = \left(\frac{\pi z}{2}\right)^{\frac{1}{2}} J_{k+\frac{1}{2}}(z) \tag{2.10}$$

$$\zeta_k(z) = \left(\frac{\pi z}{2}\right)^{\frac{1}{2}} [J_{k+\frac{1}{2}}(z) + i(-1)^k J_{-k-\frac{1}{2}}(z)] \tag{2.11}$$

wherein J_x is the Bessel function of order x.

Finally, the computed value of Q_{scat} can be converted to the scattering coefficients, σ_{scat}, with units m^{-1}:

$$\sigma_{scat} = \frac{N_p \pi D_g^2 Q_{scat}}{4} \tag{2.12}$$

wherein N_p is the number concentration (particles per unit volume) of the aerosol particles at the given diameter. (Equivalent expressions can be formed for σ_{ext} and σ_{abs} through the substitution of the appropriate efficiency value.) But Equation 2.12 holds only for a monodisperse aerosol; in general one is looking at a size distribution of various aerosols, and one must calculate the contributions to the scattering coefficient from the entire size distribution. As such, the integral expression is:

$$\sigma_{scat} = \frac{\pi}{4}\int_{D_g=D_{min}}^{D_{max}} N_p(D_g) D_g^2 Q_{scat}(D_g) dD_g, \tag{2.13}$$

where the integration is carried out across the aerosol size spectrum, from the smallest diameter, D_{min} to the largest, D_{max}. Both the N_p and Q_{scat} vary with diameter.

Once the extinction coefficient has been determined, one can determine the unitless optical depth, τ:

$$\tau = \int_0^H \sigma_{ext}(z) dz, \tag{2.14}$$

where H is the total depth of the layer and z is the height within the layer. This can then be substituted into Equation 2.15, the Beer-Lambert law [Seinfeld and Pandis, 1998], to determine the irradiance, F, at depth H into the layer, assuming an incident irradiance of F_0:

$$F = F_0 e^{-\tau} \tag{2.15}$$

In the atmosphere, the total extinction coefficient (σ_{ext}) is determined by absorption and scattering by both gas molecules and aerosol particles, as given by Equation 2.16:

$$\sigma_{ext} = \sigma_{sp} + \sigma_{ap} + \sigma_{sg} + \sigma_{ag} \tag{2.16}$$

where σ_{sp} is the scattering coefficient by aerosol particles and σ_{ap} is the absorption coefficient due to aerosol particles; σ_{sg} and σ_{ag} are the same quantities, but due to the effects of gas molecules, in the Rayleigh regime.

The scattering phase function, characteristic of particular values of x and m, describes the proportion of scattering in each direction. The normalized phase function determines the proportion of scattered intensity F at a given angle θ, measured from the beam of incident radiation, to the total scattered intensity at all angles, as is given in Equation 2.17 [Seinfeld and Pandis, 1998]:

$$P(\theta, x, m) = \frac{F(\theta, x, m)}{\int_0^\pi F(\theta, x, m) sin\theta d\theta} \tag{2.17}$$

This equation integrates over the scattering plane, which is any plane parallel to the beam of incoming radiation. The scattering is symmetrical with respect to the azimuthal angle, ϕ.

In order to determine the hemispheric backscattering coefficient, β, one must consider the fraction of the scattered intensity that is redirected into the backward hemisphere of the particle. This is given in Equation 2.18:

$$\beta = \frac{\int_{\frac{\pi}{2}}^\pi P(\theta) sin\theta d\theta}{\int_0^\pi P(\theta) sin\theta d\theta} \tag{2.18}$$

This can then be used to calculate the hemispheric backscattering coefficient, σ_{bsp}, using Equation 2.19.

$$\sigma_{bsp} = \sigma_{sp}\beta \tag{2.19}$$

This quantity is desirable as it can be measured directly by an integrating nephelometer, and how well the measured and calculated values agree can give some indication of the sphericity of the particles [Fridlind and Jacobson, 2003].

Another useful quantity is the single-scattering albedo of a particle, ω, which can be thought of as the probability that light lost to extinction by the particle is scattered rather than absorbed. Thus, it is simply the ratio of the scattering efficiency to the extinction efficiency, as: $\omega = \frac{Q_{scat}}{Q_{ext}}$. This can be extended to describe the single-scattering albedo of a distribution of particles, by using the scattering and extinction coefficients calculated based upon the particle size spectrum:

$$\omega = \frac{\sigma_{scat}}{\sigma_{ext}} \tag{2.20}$$

Equivalently, the probability of light being absorbed rather than scattered is given by the single-scattering co-albedo, $\overline{\omega}$, in Equation 2.21:

$$\overline{\omega} = \frac{\sigma_{abs}}{\sigma_{ext}} = 1 - \omega \tag{2.21}$$

Chapter 3

The Cruise Data

3.1 Introduction

In a closure experiment an aerosol property is measured in one or more ways, and then calculated from a model based upon independently measured data [Quinn et al., 1996]. In the optical closure study described here, the aerosol properties in question are the scattering, backscattering, and absorption coefficients of the marine aerosol. The comparison between the calculated and measured values is a basis for the level of confidence in both the measurements and the model. In order to perform an optical closure study, it is necessary to know the chemical composition of the aerosols, their complex refractive indices, their size distributions, and their observed optical properties.

Such an optical closure study is performed here by comparing the measured aerosol particle scattering and absorption coefficients with those calculated from Mie theory using the measurements of the aerosol particle size distribution and the size-resolved chemical constituents as inputs to the model. A schematic of the closure study is presented in Figure 3.1.

The cruise measurements provide optical data for the remote environment of the northeast Pacific, in the region of 50.37°- 51.41°N, 142.23°- 145.00°W. The path of the ship during the sampling period is shown in Figure 3.2. According to assessments of single-scattering albedo measurements [Liousse et al., 1996, Heintzenberg et al., 1997], this is part of a region with notably scarce data.

3.2 Measurements

The cruise data were collected as part of the Sub-arctic Ecosystem Response to Iron Enrichment Study (SERIES), an experiment of the Canadian Surface Ocean

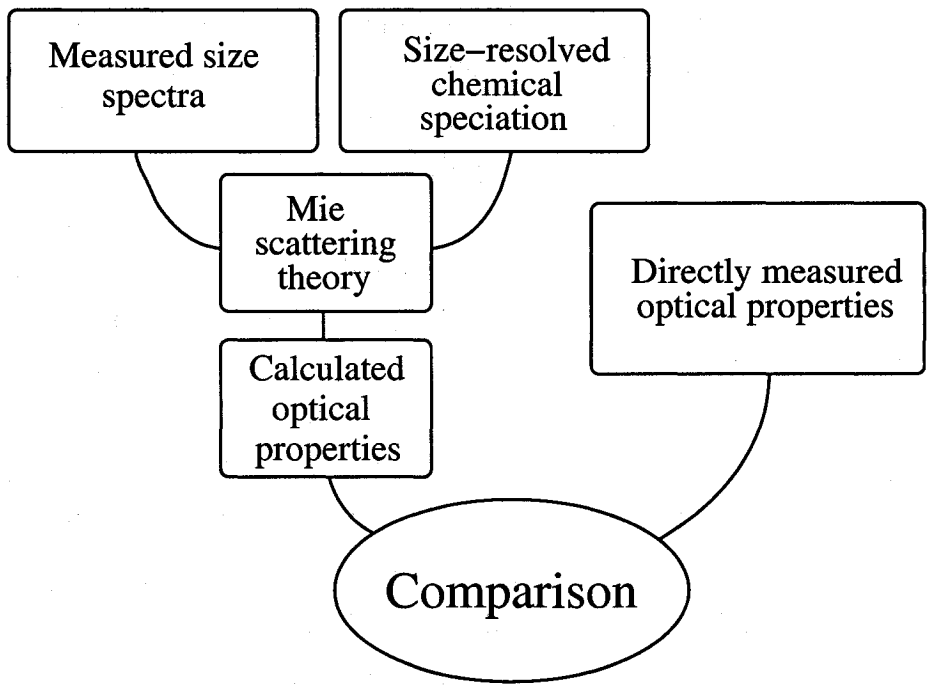

Figure 3.1: A schematic of an optical closure test, with the direct measurements of the aerosol optical properties on the right-hand branch, and the calculated values determined from independent measurements on the left.

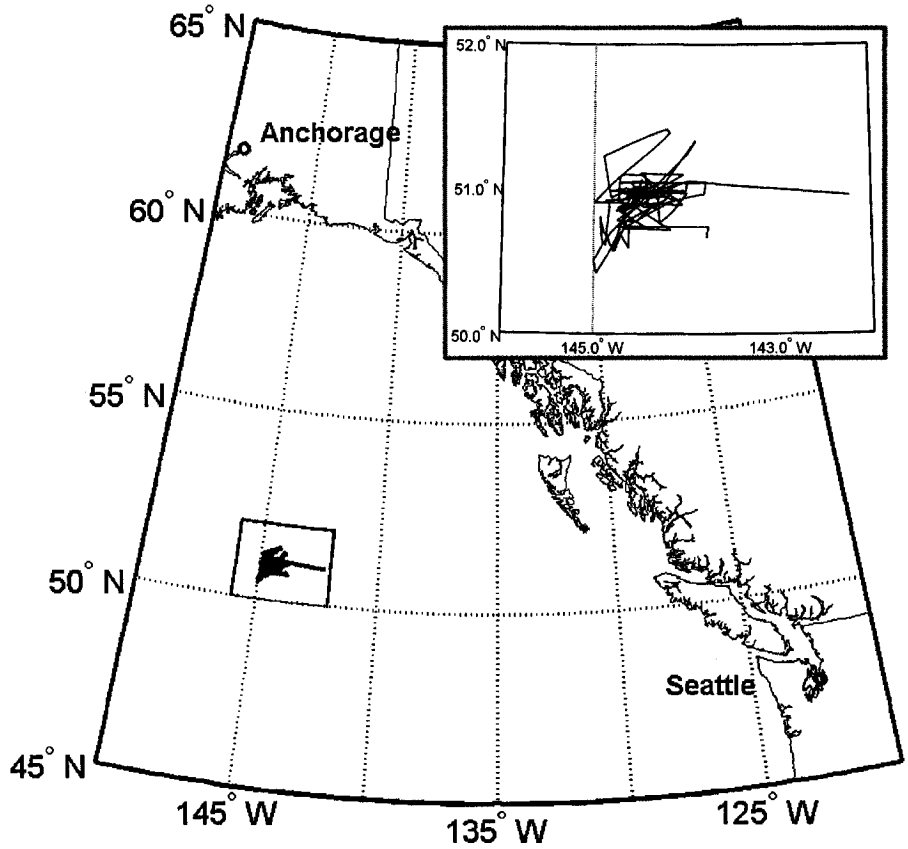

Figure 3.2: The region of the Pacific where the cruise took place, off the west coast of Canada. The path of the ship is plotted as a red line. The inset in the upper right is a higher-resolution map of the boxed region in the lower left.

Lower Atmosphere Study (C-SOLAS) program. The platform was the Mexican research vessel El Puma, which left from Sidney, British Columbia on July 2, 2002, for the study region approximately 1400 km into the north-eastern Pacific. The data were collected over the course of the cruise, from July 5 to July 30, 2002. In this thesis only the data collected from July 20 to July 30 will be considered since the instruments were fully functional during that time period only.

The measurements relevant to this study are the size spectra of the aerosols, their chemical constituents, and the scattering and absorption coefficients of the aerosols. The inlets for all the measurements involved were located at approximately 12 m above sea level.

The size spectra were measured with a TSI Scanning Mobility Particle Sampler (SMPS), a PMS Passive Cavity Aerosol Spectrometer Probe (PCASP), and a PMS Forward Scattering Spectrometer Probe (FSSP). These instruments have dameter ranges of 0.008-0.32 μm, 0.15-3.0 μm and 2.0-47.0 μm, respectively. The inorganic chemical data used here were collected with a 10 stage MOUDI (Multiple Orifice Uniform Distribution Impactor), with midpoint diameters ranging from 0.06 μm to 18 μm. The MOUDI was used in a static as opposed to rotating mode. Further chemical information was provided by the Aerosol Mass Spectrometer (AMS), which measures submicron size-segregated chemical composition of non-refractory species as a function of time. The scattering and backscattering coefficients were measured with a TSI 3563 Integrating Nephelometer, and the absorption coefficient was measured with a Particle Soot Absorption Photometer (PSAP). The nephelometer measures scattering and backscattering coefficients at three different wavelengths (blue: λ=450 nm, green: λ=550 nm, and red: λ=700 nm), while the PSAP measures the absorption coefficient at 565 nm only. Finally, the concentration of SO_2 was measured by a Pulsed Fluorescent Ambient SO_2 Analyzer in order to detect the presence of ship exhaust in the samples. These instruments are summarized in Table 3.1.

All the data were interpolated to a 10-minute time step, with the exception of the MOUDI filter data that were integrated over sampling periods ranging from 6 to 16 hours (mean of approximately 9 hours). Other than the MOUDI data, all

Table 3.1: A summary of the instruments used during the cruise, the size range over which they operate and a description of their function.

SMPS – Scanning Mobility Particle Sizer [Sioutas et al., 1999]	
Size range	0.008-0.32 μm with 26 size bins
Description	Charges particles and sizes them based on their mobility within an electric field.
PCASP – Passive Cavity Aerosol Spectrometer Probe [Liu et al., 1992]	
Size range	0.15-3.0 μm with 15 size bins
Description	An intrusive optical particle counter (OPC) which sizes particles based on the amount of light each one scatters.
FSSP – Forward Scattering Spectrometer Probe [Jaenicke and Hanusch, 1993]	
Size range	2.0-47.0 μm with 15 size bins
Description	A non-intrusive OPC, using the forward scattered light from an incident laser to determing the size of the larger particles.
MOUDI – Micro-Orifice Uniform Deposit Impactor [Marple et al., 1991]	
Size range	0.03-18.0 μm in 12 stages
Description	A 12 stage impactor using teflon filters as the collection surface at each stage. Particles collected on each filter are subsequently analyzed by ion chromatography.
AMS – Aerosol Mass Spectrometer [Jayne et al., 2000]	
Size range	0.06-0.6 μm vacuum aerodynamic diameter at 100% efficiency; efficiency drops outside this range
Description	Aerosols are sized by vacuum time-of-flight measurements then vapourized, ionized, and passed through a mass spectrometer. This determines the size distribution and mass concentration of non-refractive aerosol species.
PSAP – Particle Soot Absorption Photometer [Bond et al., 1999]	
Size range	$>$ 0.01 μm
Description	Absorption is based on the attenuation of green light (0.565 μm) by the particles collected on a filter.
Integrating Nephelometer [Anderson et al., 1996]	
Size range	$>$ 95% of particles with an aerodynamic diameter from 0.05 to 5.0 μm, with collection efficiency falling after that
Description	Measurement of the light scattered by a defined volume of particles at three wavelengths (0.45 μm, 0.55 μm, 0.70 μm).
Pulsed Fluorescent Ambient SO_2 Analyzer [Luke, 1997]	
Description	Pulsating ultraviolet light is focused into a fluorescence chamber filled with sample air, thereby exciting SO_2 molecules into higher energy states. These molecules then emit a characteristic radiation as these energy states decay. This radiation is filtered and measured by a photomultiplier tube.

the data were filtered to remove the presence of ship exhaust in the data. To determine when ship exhaust was present measurements of SO_2 were employed, as it is a byproduct of the combustion of sulfur containing fuels. The SO_2 levels were measured every minute. Whenever the concentration of SO_2 rose above 1 ppb the data were considered to be tainted by ship exhaust and were removed from the study.

The MOUDI filters were only employed when the air was considered to be free from exhaust. Still, some contamination of the filters occured. Any filters which were severely influence by ship exhaust were not considered in the analysis. Ten sets of usable MOUDI filters were collected over the time period in question, and three blanks, for the purposes of calibration.

The averaged data for the MOUDI filters is shown in Figure 3.3. The composition of the aerosol as a function of diameter is a necessary input to the Mie calculations in order to carry out the optical closure study. The MOUDI analysis separates the inorganic constituents into the following categories: Cl^-, NO_2^-, Br^-, NO_3^-, $SO_4^=$, $C_2O_4^=$, Na^+, NH_4^+, K^+, Mg^{++}, Ca^{++}, and methanesulfonic acid (MSA). For the purposes of this study, these were grouped into ($Na^+ + Cl^-$), ($NO_2^- + NO_3^-$), ($NH_4^+ + SO_4^=$), MSA, and other, based upon Li et al. [1998]. The coarse particle mass was dominated by ($Na^+ + Cl^-$), whereas the fine particle mass was predominantly ($NH_4^+ + SO_4^=$). Phinney et al. [2005] demonstrate that the submicron sulfate results agree well with the measurements from an Aerodyne Aerosol Mass Spectrometer (AMS). No comparison could be made for the levels of ($Na^+ + Cl^-$) as the AMS evaporator does not operate at a sufficiently high temperature to volatilize sea salt. Though the AMS inorganic data were measured at a higher time resolution than the MOUDI data, they are not used in this study due to the inability of the AMS to measure supermicron aerosols and sea salt.

The AMS is able to measure the organic fraction of the aerosol, though it provides little information on the individual species. This makes it difficult to estimate the optical properties of the organics. Because the organic concentration is relatively low during the period of interest, as shown in Figure 3.4, and because their optical properties are not known, the organic fraction is not included in the

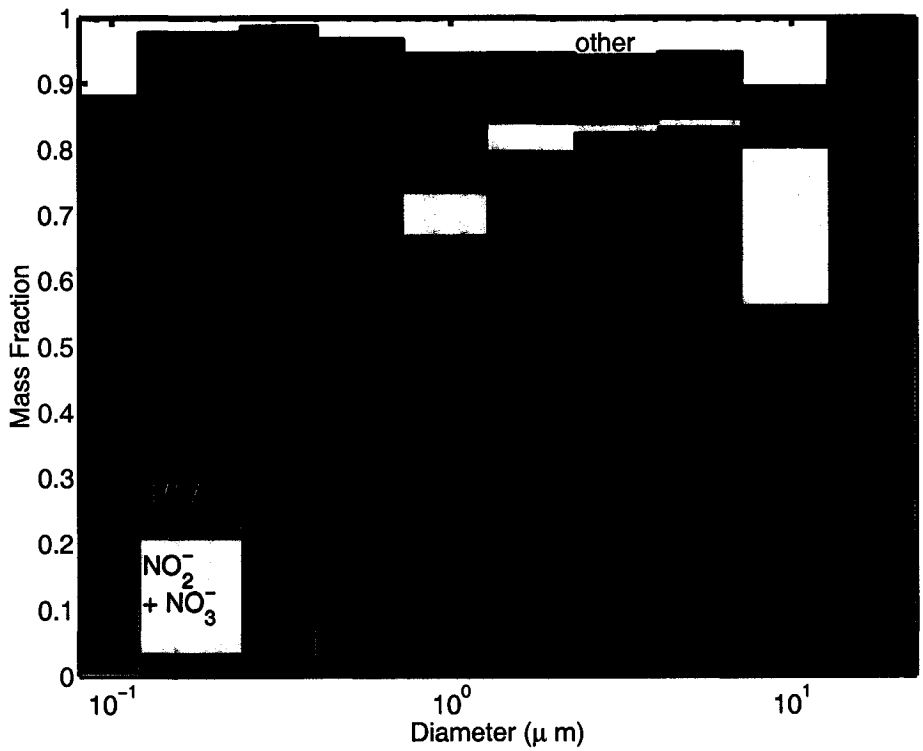

Figure 3.3: The average fractional concentration of chemical constituents as measured by the MOUDI filters.

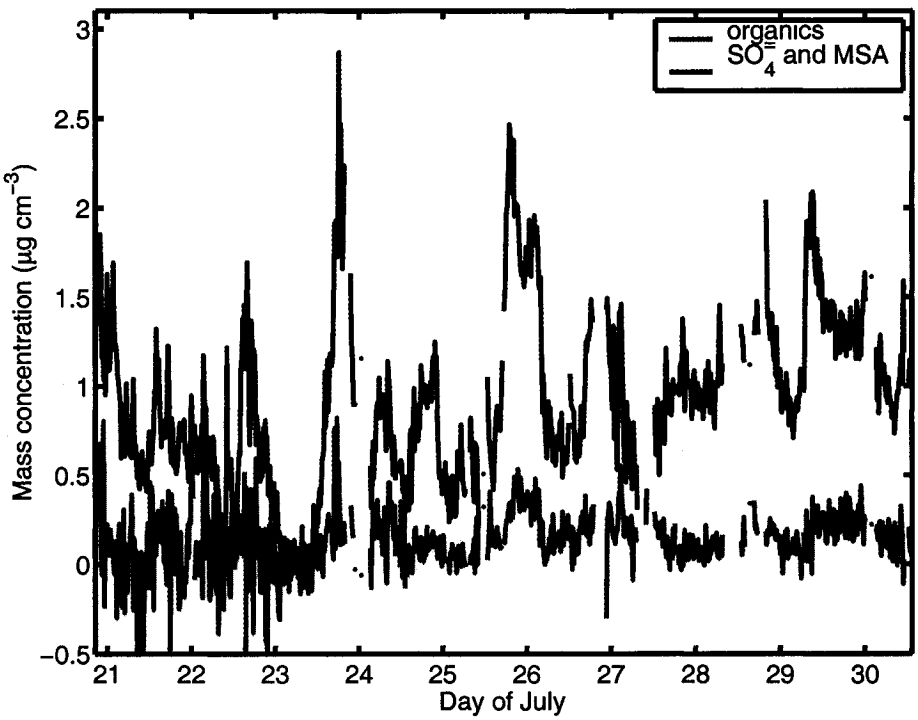

Figure 3.4: The mass concentration of organics (in green) and sulfur species ($SO_4^=$ + MSA – in red) as measured by the AMS. Over the time period samples the organic fraction of the aerosol represented only a small fraction of the mass as compared to the sulfur species.

calculations. Including the organics and assuming that they have the same optical properties as sulfate changes the results by less than 4% throughout. The complex indices of refraction for ammonium sulphate and sea salt (Tang [1996]; Toon et al. [1976]) are used as inputs to the calculations.

Figure 3.5 shows both differential number density and differential surface area density averaged over the period in which the data are being analyzed. Though the number concentration maximum is firmly in the submicron range, the surface area maximum is in the coarse mode, which is typical for marine aerosols [Seinfeld and Pandis, 1998].

The scattering coefficients measured with the nephelometer are shown in Figure 3.6. The blue wavelength has the highest scattering and backscattering coefficient, followed by the green and the red. This is consistent with Mie theory, as

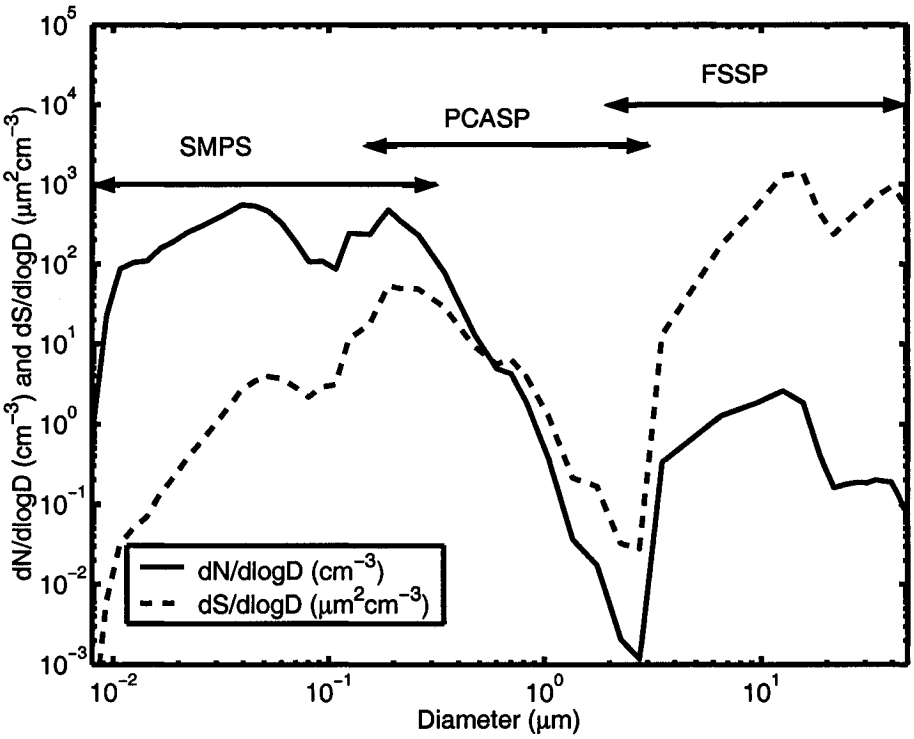

Figure 3.5: Lognormal number (solid line) and surface area (dashed line) concentrations as a function of diameter. The sampling range of each instrument (SMPS, PCASP and FSSP) is indicated.

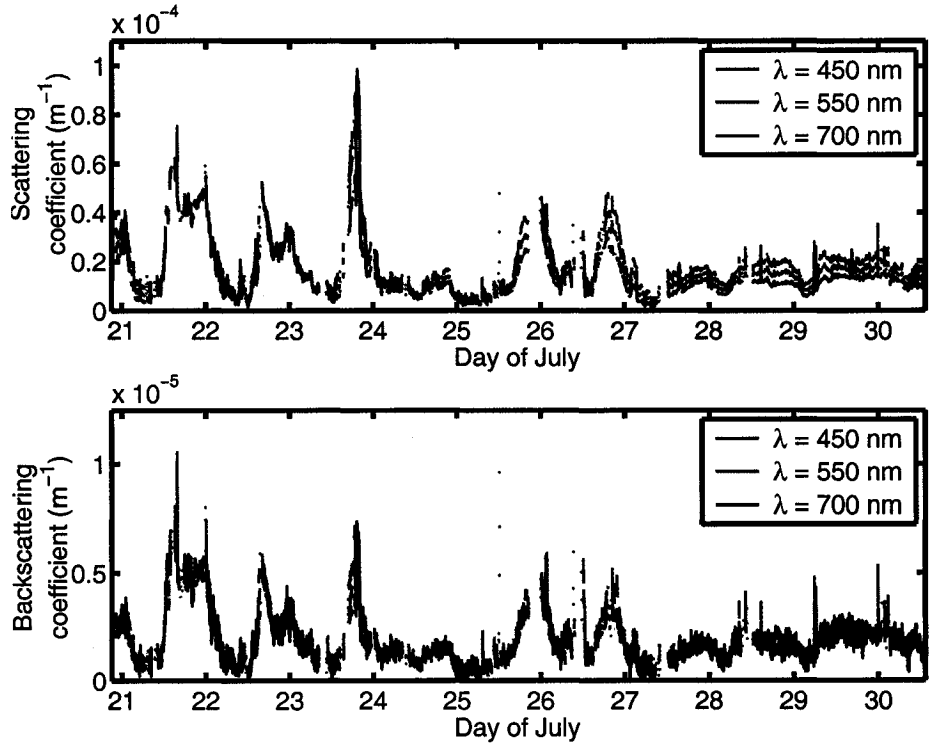

Figure 3.6: (a) The top three curves represent the scattering coefficients (σ_{sp}) for the three different wavelengths of light measured by the integrating nephelometer. (b) The same information, but for backscattering coefficients (σ_{bsp}).

smaller wavelengths result in a larger size parameter for the same size scatterer, as shown in Equation 2.5 [Bohren and Huffman, 1998].

The cruise averages of the scattering coefficients are 20 ± 3, 17 ± 3 and 14 ± 2 Mm^{-1} for blue, green and red light, respectively. For the backscattering coefficients the averages are 2.1 ± 0.4, 1.9 ± 0.4 and 1.6 ± 0.3 Mm^{-1}. The ± values are based on the uncertainty in the nephelometer measurement, estimated here to be ±15% after Fridlind and Jacobson [2003] and Quinn and Coffman [1998].

Chapter 4

The Closure Experiment

4.1 Analysis

4.1.1 Mie Calculations

The optical model used here is an adaptation of the Mie code outlined in Bohren and Huffman [1998], integrating over specific angular contributions so as to account for the angular truncation of the nephelometer. All the chemical constituents are assumed to be externally mixed. This assumption should not greatly affect the results, due to the dominance of sea salt and ammonium sulphate and the scarcity of BC [Tang, 1997], [Li et al., 1998].

The inputs for the Mie calculations were the time series of the aerosol size spectra and the time series of the size-segregated chemical constituents as measured by the MOUDI filters. The time steps of these two sets of data are very different, but the MOUDI values were assumed to be constant over each sampling period until the next sampling period began, while the size spectra changed every ten minutes. The Mie calculations were carried out for each 10-minute time step.

The calculated and measured scattering coefficients for the green wavelength are shown in Figure 4.1. Similar results are found for red and blue light. When compared to the value calculated using Mie theory, the nephelometer signal is smaller by more than an order of magnitude throughout most of the time series. This is largely due to the angular truncation in the measurement; as a result of the geometry of the nephelometer scattering is only measured between 7°and 170°. Much better agreement was attained by incorporating this angular limitation into the Mie calculations. With this limitation accounted for, the measurable theoretical curve agrees fairly well, and the two are usually within about 15% of each other, as shown in Figure 4.2. The times when this ceases to be true are the evenings of

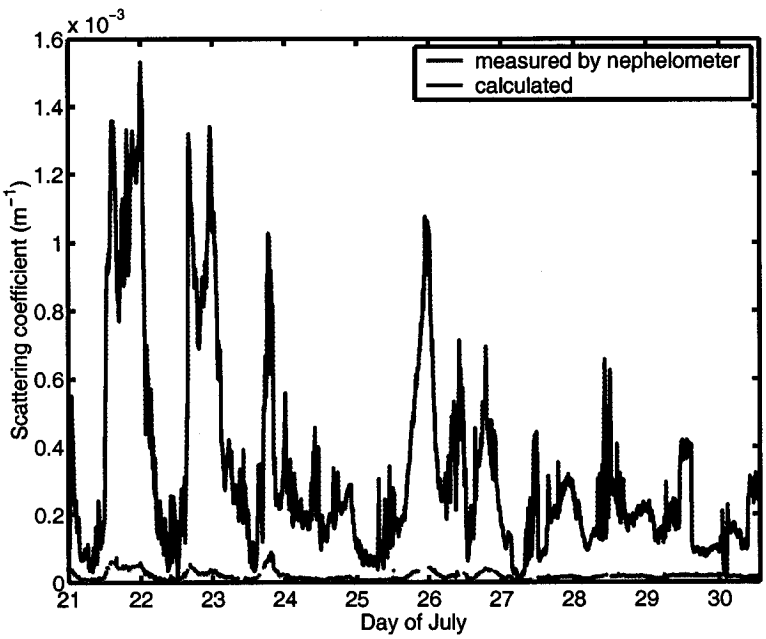

Figure 4.1: The green line shows the measured scattering coefficient (σ_{sp}) for green light, while the blue line shows the calculated value (σ_{spc}) based upon the size spectra and the chemical information.

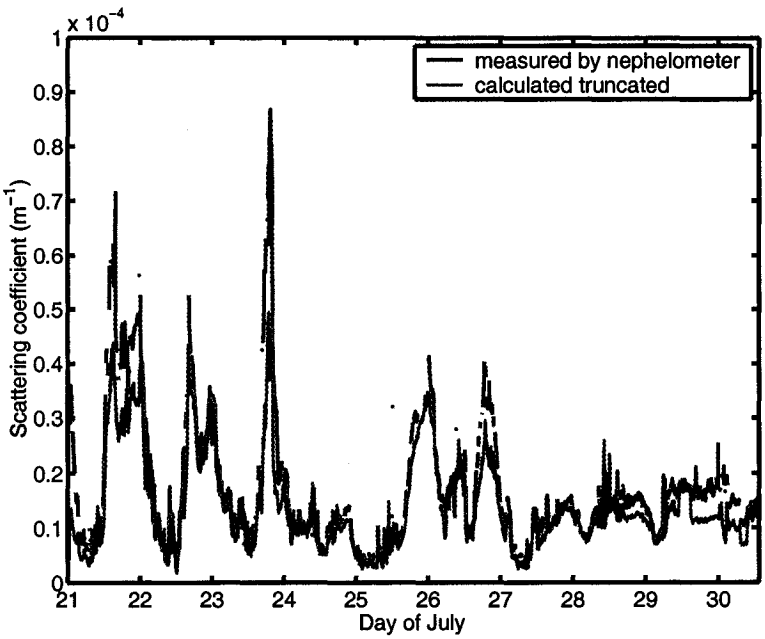

Figure 4.2: The measured scattering coefficient by aerosol particles (σ_{sp}) is shown with a green line, and the calculated truncated value based upon the angular limitations of the nephelometer (σ_{spt}) is plotted in orange.

21 July and 23 July, when the measured scattering was exceptionally high.

Angular truncation is a well-recognized limitation of the nephelometer [Anderson et al., 1996], and is discussed at length by Anderson and Ogren [1998]. Their suggested correction factor for total scattering coefficient for sampling without a size cut (λ = 0.55 nm) of 1.29 $\pm$ 0.23 is much smaller than the correction factor necessary in this case.

The disagreement between the measured scattering coefficient and the calculated value can be largely attributed to the dominant forward scattering signal of the coarse aerosol particles. The phase function for larger scatterers is concentrated in one large central lobe, which is largely missed when neglecting the contribution between 0°and 7°. This can be seen in a diagram of phase functions, in Figure 4.3. Here the region that cannot be measured by the nephelometer is demarcated with solid lines. Clearly, for large scatterers, relatively little of the signal can be measured.

To examine the measurable backscattering, the effects of the forward and backward angular truncations were separated. Figure 4.4 shows the calculated σ_{bspc} (from 90°to 180°) as a function of scatterer diameter, along with the calculated truncated value, σ_{bspt}, due to the backward truncation between 170°and 180°. Not only is the angular truncation significant, but about half the signal is missed for scatterers larger than one micron.

Applying these results to the measured data yields Figure 4.5. Again, the calculated value from Mie theory is much larger than that measured by the nephelometer. However, when the angular correction is applied the agreement is even better than for the total scattering, with no systematic underestimation. Similar results were found when the analysis was repeated for the other two wavelengths. The findings are summarized in Table 4.1.

The uncertainties given on the numbers in Table 4.1 are based upon estimated uncertainties in the instruments. The estimated uncertainty in the measured value is assumed to be $\pm$15%, based on the upper limit proposed by Fridlind and Jacobson [2003] and Quinn and Coffman [1998]. The uncertainty in the calculated value is estimated at $\pm$20%. This is based upon the combination of the estimated error in

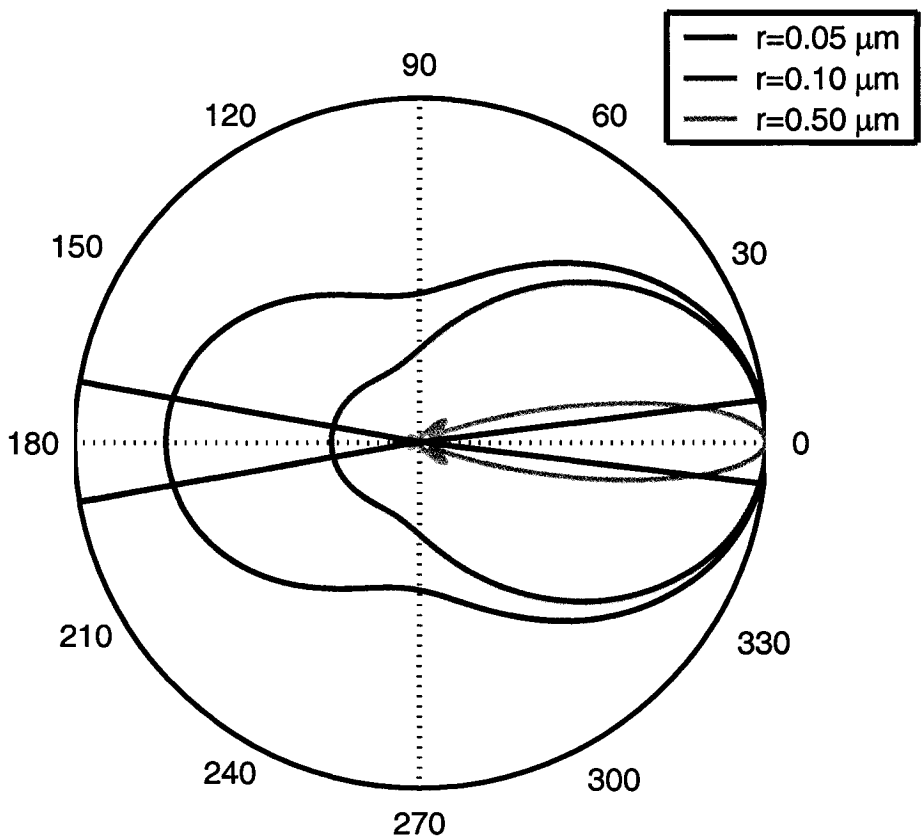

Figure 4.3: Scattering phase functions for a variety of particle radii. All calculations here assumed that $\lambda = 0.55$ μm, and $m = 1.55 + 0i$, representing SiO_2. The phase functions are normalized in the forward scattering direction for ease of display. The regions delineated in red cannot be measured by the nephelometer.

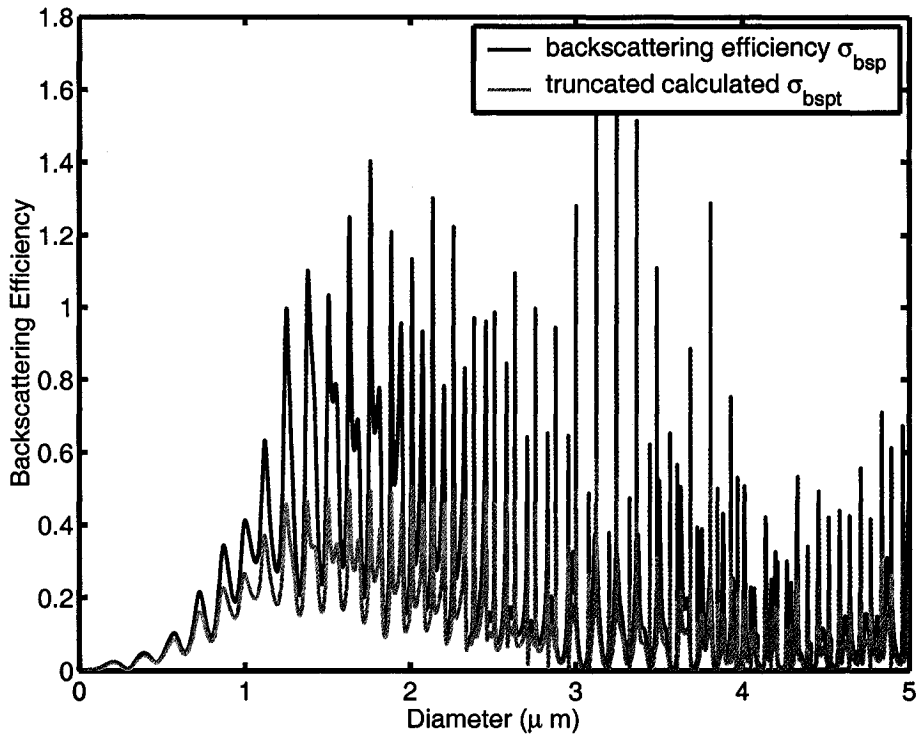

Figure 4.4: The backscattering efficiency for particles, Q_{bspc}, as a function of scatterer diameter (dark blue) and the calculated truncated backscattering efficiency, Q_{bspt}, due to angular truncations (light blue).

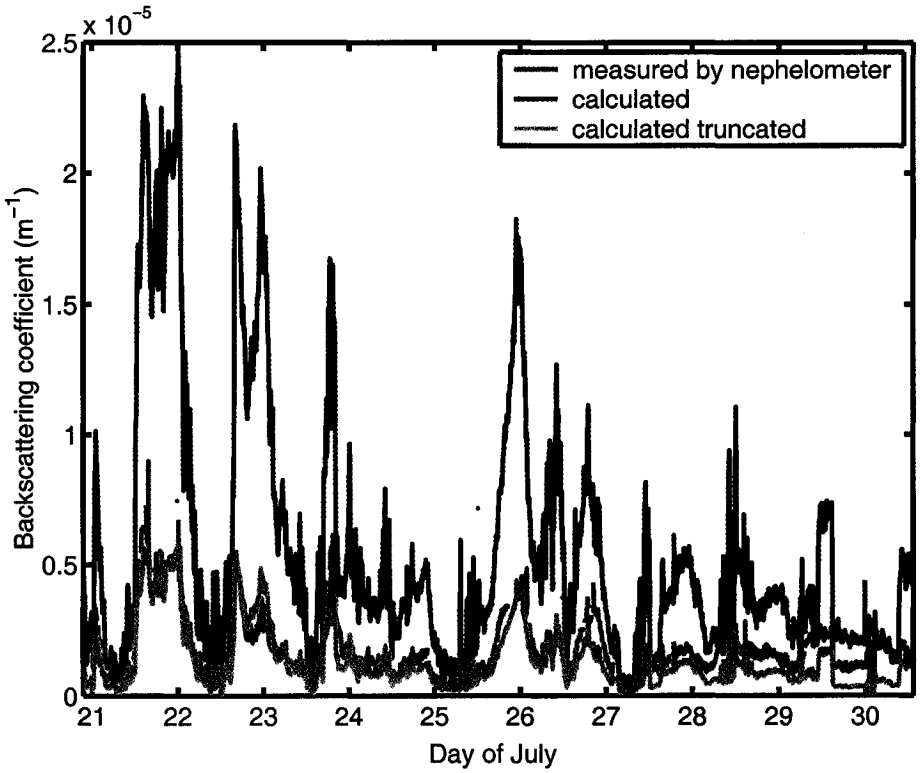

Figure 4.5: The measured value (σ_{bsp}) for green light is shown in green, the calculated value (via Mie theory based upon size and chemical information) (σ_{bspc}) is in blue, and the calculated truncated value (σ_{bspt}) is plotted in orange.

the following measurements: particle counting (±10%), uncertainties in the flow rate (± <10%), particle sizing (±2-10%), and chemical speciation (± <5%). The uncertainty in the particle sizing is defined as half the bin width divided by the midpoint diameter. These uncertainties are determined by calculating the result at both the upper and lower boundary of the estimated values for each of the measured quantities, and then adding the errors in quadrature. The resultant estimated error in the calculated quantities is then approximately ±20%. This uncertainty in the mean is larger than one standard error of all measurements acquired over the 21 to 30 July sampling period, and is the value used here.

The absorption coefficient measured by the PSAP was corrected for flow, spot size, and uncertainties in the instrument, as outlined in Bond et al. [1999]. After

Table 4.1: A summary of the scattering and backscattering coefficient, averaged over the total measurement period; measured, calculated and calculated truncated values for all three wavelengths. The given errors are based upon the estimated uncertainties in each of the quantities – ±15% for the measured value and ±20% for the calculated values.

Total scattering coefficients (Mm^{-1})			
λ (μm)	measured σ_{sp}	calculated σ_{spc}	truncated σ_{spt}
0.45	20 ± 3	320 ± 60	15 ± 3
0.55	17 ± 3	320 ± 60	13 ± 3
0.70	14 ± 2	320 ± 60	12 ± 2
Backscattering coefficients (Mm^{-1})			
λ (μm)	measured σ_{bsp}	calculated σ_{bspc}	truncated σ_{bspt}
0.45	2.1 ± 0.3	5.4 ± 1.1	2.1 ± 0.4
0.55	1.9 ± 0.3	4.6 ± 0.9	1.9 ± 0.4
0.70	1.6 ± 0.2	2.7 ± 0.5	1.6 ± 0.3

these corrections the mean absorption coefficient (σ_{ap}) measured with the PSAP was 1.3 ± 0.6 Mm^{-1}, with the uncertainty derived from the correction factors in Bond et al. [1999]. The calculated value, based only on the absorption by the inorganic species, is 1.3 ± 0.3 Mm^{-1}, based upon an uncertainty of ~20% in the calculation. These values agree within the estimated uncertainties, which suggests that BC was not a significant factor in this particular environment.

Given the scattering and absorption coefficients, one can estimate the aerosol optical depth, τ, of the marine boundary layer, using Equation 2.14. If we use the calculated values of σ_{spc} and σ_{apc}, and assume a well-mixed boundary layer of depth H = 300 m, this yields a τ of approximately 0.1 at 550 nm. The estimated value for the depth of the marine boundary layer is consistent with estimated height of the cloud base observed throughout much of the cruise. The resultant value of τ compares well with the findings of Smirnov et al. [1995], who give a τ of 0.09 to 0.12 for air over the Pacific with similar synoptic conditions, though integrated over the whole atmosphere. The implication of the agreement is that sea

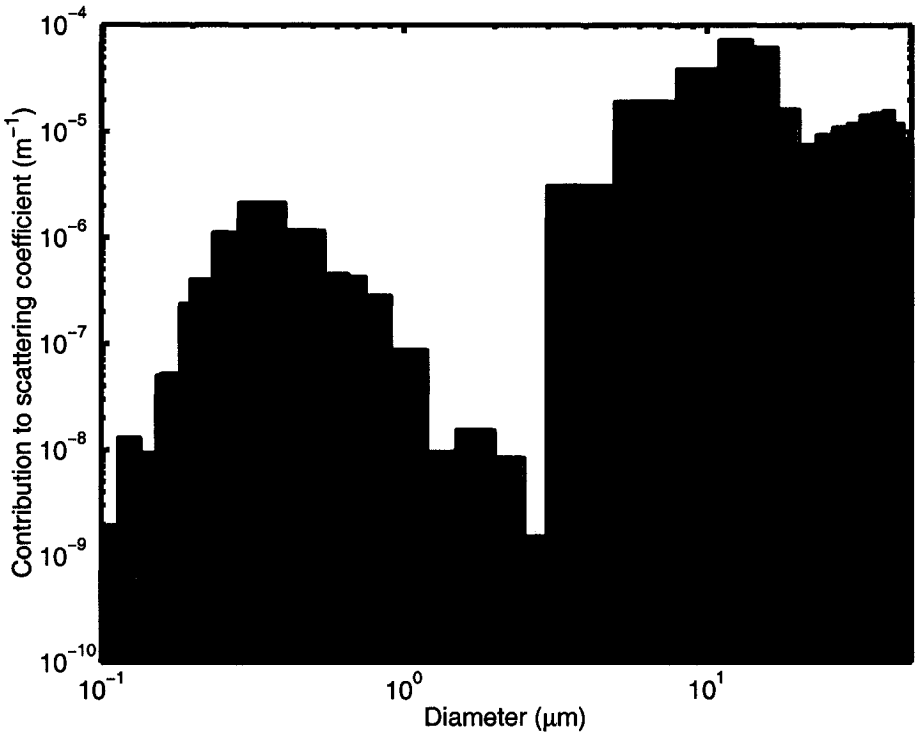

Figure 4.6: The calculated scattering coefficient, σ_{spc} (blue), and the truncated calculated scattering coefficient, σ_{spt} (red), both as a function of diameter.

salt in the marine boundary layer may often dominate the aerosol optical depth of the troposphere over the North Pacific [Marshall et al., 2005]. Indeed, in the next section it is shown that the sea-salt dominated coarse mode is the principal optical contributor.

4.1.2 Attribution of Scattering by Size

There was no separate sampling of submicron and supermicron aerosols with the nephelometer, so it is necessary to analyze the data after the fact to attempt to apportion the scattering based upon size. The contribution of each size bin to the scattering is shown in Figure 4.6. These data are based purely upon the calculated results from the measured size spectra and chemical information.

The calculated scattering coefficient, σ_{spc}, indicates that the vast majority of the scattering is due to particles in the coarse mode, particularly around 10 μm. The

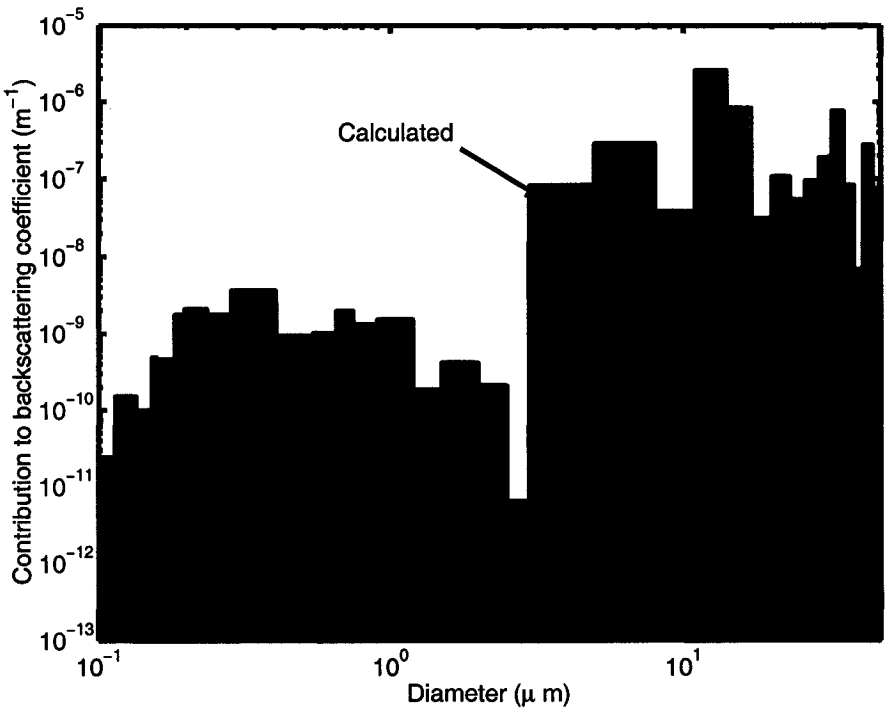

Figure 4.7: The calculated backscattering coefficient, σ_{bspc}, as a function of diameter (blue), and the same calculation including angular truncation, σ_{bspt} (red).

values calculated when considering the angular truncation are much lower in the coarse mode, whereas the contribution to scattering from the fine mode changes relatively little. The truncated calculated scattering coefficient (σ_{spt}) is more evenly distributed between the two modes.

The same analysis was carried out for the backscattering coefficients, and is shown in Figure 4.7. Again, most of the backscattering is from the coarse particles due to their dominance during the cruise. The fine mode is even less evident than in the case of total scattering. The gap between the calculated value and the calculated truncated value is considerably smaller.

The fractional contribution to σ_{spc} and σ_{bspc} from the fine particles including extinction at all angles is 0.020 ± 0.006 and 0.0029 ± 0.0008 respectively at a wavelength of 550 nm. When one repeats the procedure having taken the angular truncation into account, the data indicate fine fractions of 0.4 ± 0.1 and 0.010 ± 0.003

Table 4.2: The fine fraction of light scattering and backscattering; given for calculated and calculated truncated values for all three wavelengths. The uncertainties are based on the uncertainties in the calculated values (~20%) combined in quadrature in the calculation.

	Total scattering		Backscattering	
λ (μm)	Fine fraction of σ_{spc} (calculated)	Fine fraction of σ_{spt} (truncated)	Fine fraction of σ_{bspc} (calculated)	Fine fraction of σ_{bspt} (truncated)
0.45	0.023 ± 0.006	0.5 ± 0.1	0.007 ± 0.002	0.013 ± 0.004
0.55	0.020 ± 0.006	0.4 ± 0.1	0.0029 ± 0.0008	0.010 ± 0.003
0.70	0.010 ± 0.003	0.21 ± 0.06	0.0020 ± 0.0006	0.004 ± 0.001

for the scattering and backscattering respectively. These can be compared to measured results in the marine boundary layer at Cape Grim, Tasmania [Carrico et al., 1998], given as 0.23 ± 0.06 for total scattering and 0.17 ± 0.06 for backscattering. The different data sets do not agree, but the inclusion of the effects of angular truncation produces values much closer to those of Carrico et al. [1998]. Similar results are obtained for the other two wavelengths, as summarized in Table 4.2.

4.1.3 Analysis of Hygroscopic Effects

The correction factor as a function of relative humidity (RH) is examined in order to determine how hygroscopic effects may affect the difference between the calculated and measured scattering signals. When a soluble aerosol is exposed to air at a relative humidity lower than that required to form a cloud droplet it may still take up some water. This leads to an increase in the size of the particle, known as hygroscopic growth. This larger particle may then scatter more light, though its index of refraction will also be changed by the presence of the water. This uptake of water only occurs at relative humidities higher than the crystallization point of the aerosol material, ~45% in the case of sea salt [Maßling et al., 2003].

The relative humidity of the ambient (outdoor) air was measured, as was the

relative humidity of the nephelometer sample after it had undergone partial drying due to heating within the instrument. This sample relative humidity was recorded by a relative humidity sensor within the nephelometer. Particles sampled by the SMPS and PCASP are essentially dried based on some degree of heating above ambient temperature before the particles are detected, as well as by the drying of the sheath air by both instruments using a desiccant. Although the FSSP is a non-intrusive probe and thus does not dry the sample at all, it was located inside the same small shelter as the nephelometer. The shelter was heated relative to the ambient by the various pumps and instruments. Thus, the sample reaching the FSSP was at a RH similar to that of the nephelometer.

Figure 4.8 shows the ambient relative humidity and that measured inside the nephelometer plotted with the total scattering coefficient measured by the nephelometer for green light. Some correlation between the sample RH and the total scattering coefficient is evident. If hygroscopic effects were solely responsible for the large correction factors then one would expect much smaller correction factors at the lowest relative humidities.

To test this, the data are sorted into different regimes of the sample relative humidity in the nephelometer. For each of these subsets of data a new correction factor is calculated. These results are shown in Table 4.3. The correction factor increases with increasing relative humidity, indicating that water very likely influenced the particle sizing at least at relative humidities above 30%. This can also be seen in the dependence of the mean particle size measured by the FSSP on the RH (the last column of Table 4.3), with the increase in size due to uptake of water. At relative humidities below 30%, well below the crystallization relative humidity of sea salt, the correction factors are still an order of magnitude above those suggested in the literature. This discrepancy indicates that the high number concentration of supermicron aerosols is not mererly due to the hygroscopic swelling of submicron aerosols shifting the size distribution to larger sizes. In fact, the high observed number concentration of large sea salt aerosols is more likely due to a high source function, that is, the rate at which aerosols are produced. This conclusion is further supported by the clear demarcation between the fine and coarse

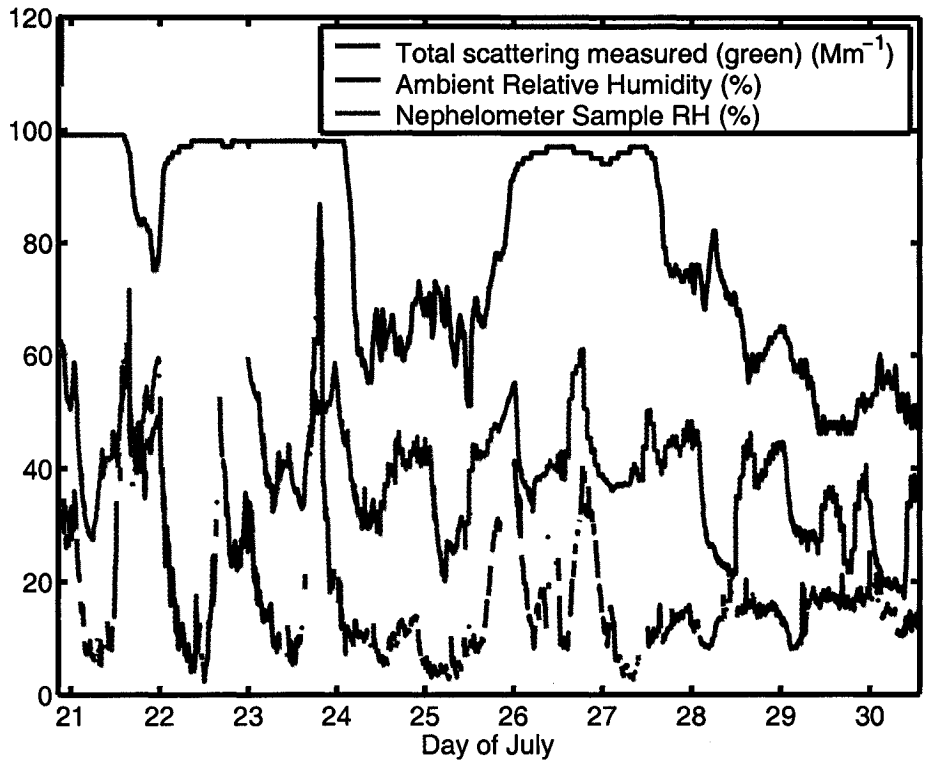

Figure 4.8: The ambient relative humidity (dark blue), nephelometer sample relative humidity (light blue), and measured scattering coefficient (green) plotted together. No sample relative humidity data were collected on 22 July.

Table 4.3: The calculated correction factor based upon the sample relative humidity as measured by the nephelometer.

Relative Humidity range (%)	Correction factor	Hours of data in this range	Mean diameter of aerosol measured by FSSP (μm)
>60	45 ± 9	5	16.12
50-60	30 ± 6	104	11.48
40-50	24 ± 5	137	11.20
30-40	19 ± 4	141	10.51
20-30	17 ± 3	68	9.86
<20	16 ± 3	11	9.20

modes seen in Figure 3.5. Had hygroscopic growth been primarily responsible for the large number of coarse particles, the fine mode would simply have been shifted to larger diameters.

The major factor influencing the number concentration of coarse marine aerosols is wind speed. The coarse particles are dominated by sea salt, and the rate of droplet production, the main source of sea salt aerosols, is a strong function of wind speed (e.g. Gong et al. [1997]). The concentration of coarse particles measured by the FSSP is plotted alongside the wind speed in Figure 4.9. The wind data were collected with an anemometer mounted approximately 10 m above sea level and corrected for ship speed and course over ground, after Smith et al. [1999].

Some correlation between the two can be seen, though there are a few notable exceptions, such as the spike in the FSSP numbers on the evening of 23 July, preceding the increase in wind speeds. This splike corresponds to a high level of sulfur species measured by the AMS, as seen in Figure 3.4. It is possible that these high FSSP counts are due to species other than sea salt. The other anomalous period is July 28 to July 29, when there are high wind speeds but low FSSP concentrations. The reason for this is unclear. Unfortunately no wind data were recorded from the evening of July 29 onward. Throughout the cruise high wind speeds were seen,

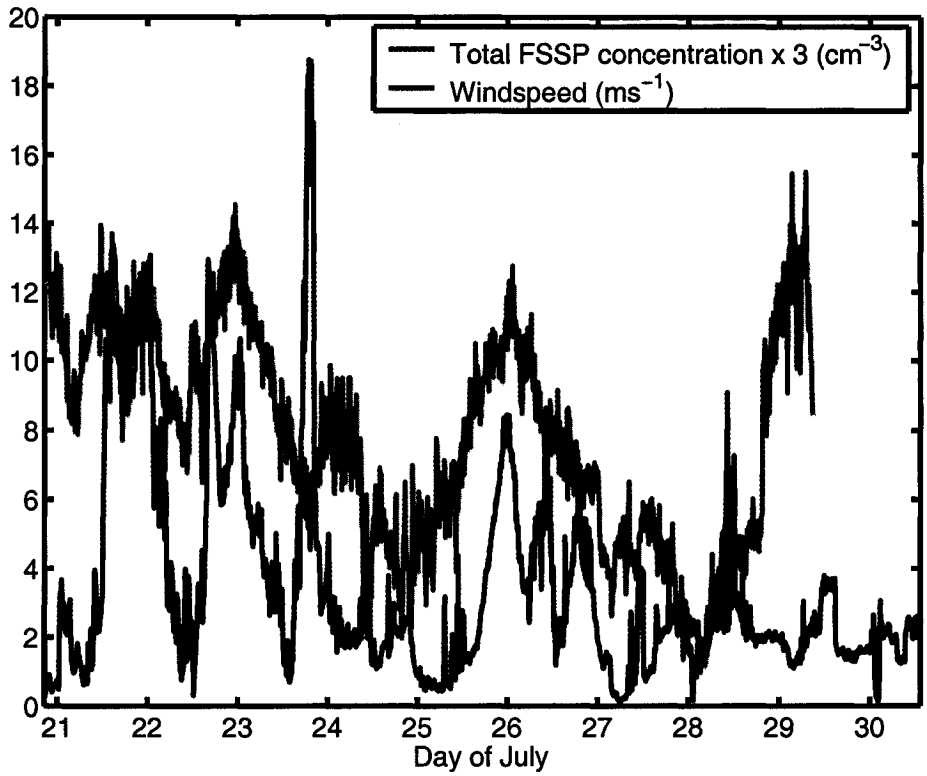

Figure 4.9: The wind speed (blue) and three times the total concentration measured by the FSSP (red). The anemometer data were not recorded from the morning of 29 July to the morning of 30 July.

with an average speed of 7.83 m s^{-1} and a direction of 231.4°over the sampling period.

4.2 Discussion

The angular truncation of the nephelometer can be a very large factor when the aerosol population contains a relatively high number of coarse particles, such as in a windy marine boundary layer. In such cases, optical properties calculated from measurements of the size distribution and chemical composition are able to provide a more accurate determination of the extinction properties than direct measurements. Without these other measurements, a condition-dependent coreection factor would have to be formulated. The difference between the measured values and those calculated using the chemical and physical measurements are striking in this case – for λ = 0.55 μm, the average measured σ_{sp} is 17 $\pm$ 3 Mm^{-1}, while the average calculated σ_{spc} is 320 $\pm$ 60 Mm^{-1}. The latter value is reduced to σ_{spt} = 13 $\pm$ 3 Mm^{-1} when the angular truncation of the nephelometer is taken into account.

The present data indicate a correction factor due to angular truncation far greater than that suggested in Anderson and Ogren [1998]. This is likely due to the size distribution of the particular case here. The correction factor given in Anderson and Ogren [1998] is relevant for some aerosol distributions, excluding those in a windy marine boundary layer.

The correction due to the non-Lambertian (non-uniform) nature of the light source was not considered here, neither was the finite bandwidth of the bandpass filters nor the deviation of the central wavelengths from the stated 450, 550 and 700 nm. All three of these effects are considered to be minimal [Anderson et al., 1996], and depend upon the specific instrument used. Based upon the work of Anderson et al. [1996] the central wavelength of the photomultiplier tubes differs by less than 3 nm from the ideal number, and the bandwith is within the 50 nm given in the manufacturer's specifications.

Table 4.4 gives some suggested correction factors for typical aerosol size distributions for a variety of environments. The aerosol size distributions are those suggested by Hess et al. [1998], with the aerosol types being water insoluble, water

Table 4.4: Suggested correction factors for specific environments based on theoretical aerosol distributions.

	Total scattering correction			Backscattering correction		
Environment	0.45 μm	0.55 μm	0.70 μm	0.45 μm	0.55 μm	0.70 μm
Clean continental	1.34	1.34	1.36	1.30	1.28	1.28
Continental average	1.33	1.33	1.35	1.29	1.27	1.27
Continental polluted	1.30	1.30	1.31	1.27	1.25	1.25
Urban	1.31	1.31	1.33	1.26	1.25	1.25
Desert	1.94	1.75	1.60	1.62	1.58	1.53
Maritime clean	1.71	1.53	1.55	1.50	1.47	1.40
Maritime polluted	1.54	1.45	1.47	1.45	1.43	1.37
Maritime tropical	1.75	1.56	1.54	1.50	1.48	1.40
Arctic	1.36	1.33	1.35	1.35	1.34	1.30
Antarctic	1.39	1.35	1.31	1.36	1.37	1.33

soluble, sea salt (accumulation mode and coarse mode), mineral dust (nucleation mode, accumulation mode, coarse mode, and transported), sulphate, and soot. The complex indices of refraction at each wavelength are taken from Koepke et al. [1997]. The correction factors in Table 4.4 are similar or slightly larger than the value suggested by Anderson and Ogren [1998]. Of particular interest is that correction factor for the clean maritime case did not significantly reduce the order of magnitude difference between the tabulated values and the correction factors from the present study. This is due to the fact that the coarse mode component of the measured size distribution is much greater in magnitude relative to the fine mode than the theoretical size distribution of Hess et al. [1998], as illustrated in Figure 4.10.

This substantial difference between the measured and "typical" aerosol size distributions suggests that the scattering coefficients predicted based upon latter may be underestimating the actual value. This has substantial implications for estimations of the direct aerosol effect. While the present results are not suggested to

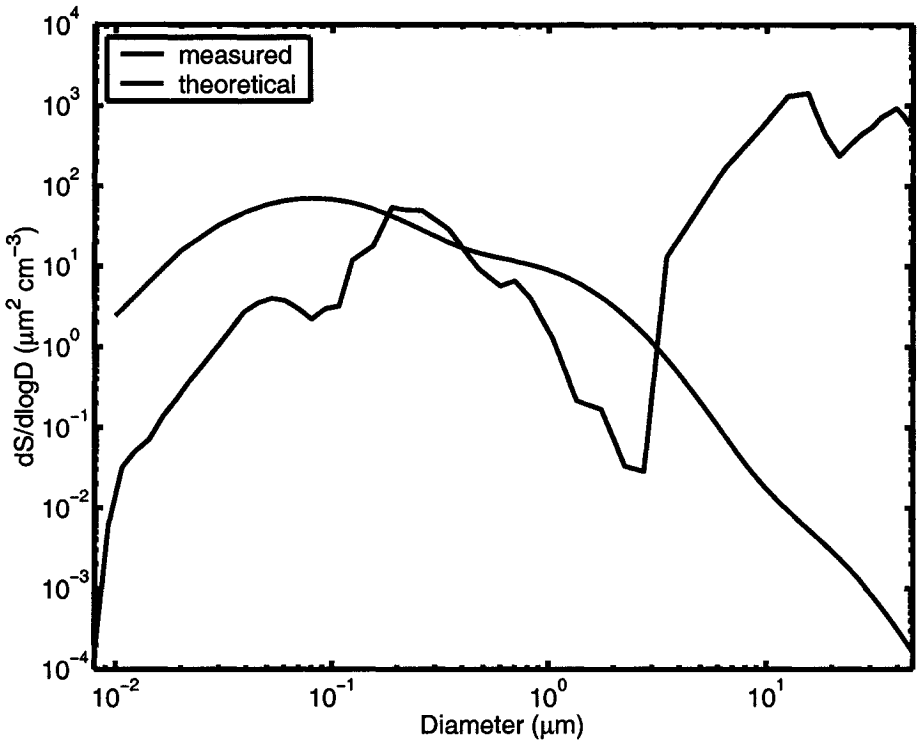

Figure 4.10: The measured differential aerosol surface area distribution (red) plotted alongside the theoretical distribution for a clean marine case (blue).

be representative of the global oceans on average, they indicate a potentially much greater role for sea salt in the direct effect than that suggested by the modelled climatological distributions of Hess et al. [1998]. The implications for high, coarse mode, sea salt concentrations in the marine boundary layer also extend beyond the direct effect to the indirect effect of aerosols, as shown by O'Dowd et al. [1999].

In order to more accurately model the direct effect based upon scattering measurements over the oceans, it is necessary to take into account the aerosol size distribution, chemical composition, relative humidity, and how these affect the scattering measurements. One method to approach this problem was suggested by Quinn and Coffman [1998], which requires the simultaneous measurement of the size distribution and chemical composition of the aerosol to enable the calculation of a correction factor at each time step, in a similar manner as was conducted here. The actual magnitude of this correction factor was not reported by Quinn and Coffman [1998]. This correction factor, c, would be the ratio of the calculated scattering coefficient to the calculated truncated value, as given in Equation 4.1:

$$c = \frac{\sigma_{spc}}{\sigma_{spt}}, \tag{4.1}$$

with a separately calculated correction factor for the backscattering coefficient, c_b, given in Equation 4.2:

$$c_b = \frac{\sigma_{bspc}}{\sigma_{bspt}}, \tag{4.2}$$

Chapter 5

The Flight Data

5.1 Measurements

From October 13 to 17 of 2003 six research flights were carried out over the waters around Nova Scotia. These flights were part of a C-SOLAS project and were carried out in conjunction with a research cruise in the area. The research platform was a Convair 580 belonging to the National Research Council of Canada. Measurements were collected in and around decks of stratocumulus, but for the purposes of this study only cloud-free measurements are being considered.

The plane was equipped with an array of instruments for the measurement of aerosol and cloud properties. The chemical composition of the aerosols was measured by an Aerodyne Aerosol Mass Spectrometer (AMS), as described in Table 3.1. The AMS provided time-series mass concentrations of aerosol groups including ammonium, sulphate, nitrate, and organics. By analyzing the times of flight of the various particles the AMS is also able to provide some information regarding the mass distribution of each species as a function of aerodynamic diameter. A description of the design and limitations of the AMS can be found in Jayne et al. [2000]. The AMS is not able to volatilize sea salt, and as such, it is not detected. Also, its transmission efficiency drops off sharply outside of the 0.07-0.6 μm vacuum aerodynamic diameter sampling range.

The aerosol size distribution measurements were provided by a TSI SMPS, a PMS FSSP, and a TSI Aerodynamic Particle Sizer (APS). The first two instruments were also used on the cruise, and a description of their properties can be found in Table 3.1. The APS was used to determine the aerosol size and number concentrations through analysis of the time-of-flight of the particles, an aerodynamic property. The sampled air is accelerated through a series of orifices and combined with filtered sheath air before entering the detection region. Here each particle

passes between a pair of overlapping laser beams, with the time between these passes being used to determine the aerodynamic particle size [Armendariz and Leith, 2002]. The APS and SMPS are both assumed to sample nearly dried particles due to the warming of air as it entered the aircraft and the use of dried sheath air [Leaitch et al., 2005].

The smallest particles from 0.1 to 0.28 μm were measured by the SMPS in 26 size bins. The larger aerosols were measured in 45 bins by the APS, with aerodynamic diameters ranging from 0.66 to 20.5 μm. Though in theory the instrument can measure aerodynamic diameters as small as 0.52 μm, the first three bins had highly erratic numbers due to particle counting statistics, and did not agree well with the FSSP mounted outside the plane. As such, these data were not used.

The aerodynamic diameters (D_a) are converted to geometric diameters (D_g) following Equation 5.1,

$$D_g = \frac{D_a}{\sqrt{\rho}}, \tag{5.1}$$

where ρ is the density of the particle in g cm^{-3}. The value assumed for ρ is different for submicron and supermicron particles, with the submicron assumptions based upon the chemical measurements. Since the AMS is able to measure the speciated mass fraction of submicron particles, the density assigned to the submicron particles is an average of the densities of ammonium sulphate, nitrate, and organics, weighted according to this speciation. Any mass unaccounted for is treated as sea salt. The density for the organic component is assumed to be 0.82 g cm^{-3}, the density of octacosanoic acid [Weast et al., 1972], a long chain fatty acid also known as montanic acid. The organic fraction was based on octacosanoic acid following Erlick et al. [2001].

The calculated densities for the submicron aerosols ranged considerably based upon the chemical measurements, from 1.13 to 2.17 g cm^{-3}, giving the APS a lower size range in geometric diameter ranging from 0.62 to 0.45 μm, based on Equation 5.1. For the supermicron mode the particles were treated as sea salt, with the appropriate density of 2.2 g cm^{-3} [Seinfeld and Pandis, 1998], giving the APS an upper size range of D_g=13.9 μm. So as to assure a smooth transition from submicron to supermicron ranges, the size bin bridging the two regions was assigned a

density which was the mean of the submicron and supermicron values.

After this conversion, a gap remains between largest size measured by the SMPS at 0.28 μm and the smallest size measured by the APS at 0.45 to 0.62 μm. These measurements were provided by the FSSP, which can measure between 0.3 and 20 μm. The FSSP is a passive instrument and the data were collected outside of the aircraft at ambient temperature. As such, hygroscopic corrections are necessary to account for the uptake of water on the particles. This correction employs a hygroscopic growth factor (HGF) which shifts the size range according to the relative humidity, as given in Equation 5.2:

$$D_g(dry) = \frac{D_g(RH)}{HGF(RH)} \tag{5.2}$$

Thus particles with diameters measured at the ambient RH ($D_g(RH)$) can be resized to their dry diameters ($D_g(dry)$). The HGF employed here is based on the parameters given in Table 5 of Maßling et al. [2003], which were determined from measurements of highly soluble larger particles ($D_g(dry)$ = 250 nm) taken during Aerosols99 over the Atlantic Ocean. The HGF is calculated as:

$$HGF(RH) = A(1 - RH)^{\gamma} \tag{5.3}$$

where γ = -0.284, A = 1.0544. This formula for the HGF was chosen over more precise laboratory experiments using NaCl or sea salt, such as those by Tang [1996], as it may better represents the behaviour of ambient marine aerosol by incorporating such things as internally mixed organic compounds which have been shown to reduce the HGF of sea salt particles [Randles et al., 2004].

The choice to use the APS data rather than those from the FSSP for the measurement of the large aerosol size spectra was based on the location of the instruments. The FSSP was mounted outside the aircraft, unlike the instruments measuring chemical composition and scattering coefficients. In order to have a meaningful comparison between the various measurements it is better that the sampled air passes through the same inlet and experiences similar resultant losses.

The total scattering and backscattering coefficients at three visible wavelengths (450, 550 and 700 nm) were again measured by the TSI 3563 Integrating Nephelometer. A size cut was not employed. With the exception of the APS, which

is described in this section, a description of all these instruments can be found in Table 3.1.

The inlet was a shrouded, nearly isokinetic diffuser, mounted ahead of the engine and approximately 15 cm off the starboard side of the fuselage of the aircraft. The shroud was designed so as to direct a minimally turbulent flow of air and particles into the intlet. From the inlet, 1 cm OD (outer diameter) stainless steel tubing was used to bring the sample air to the on-board instruments (the SMPS, APS, nephelometer, and AMS). The AMS was located approximately 5 m from the intake, while the other three instruments were within about 1 m of the intake.

For this closure experiment all the above mentioned quantities were averaged over the 5 minute sampling time of the AMS. All of the segments which consisted of level, sustained, cloud-free flight were then assessed for point closure. Any segment where the air pressure was less than 800 hPa (corresponding to an altitude of ~2000 m) was not considered, as the SMPS had sampling problems in these regions due to the lower dielectric constant of the air. The five minute segments immediately adjacent to in-cloud samples were not considered, so as to avoid potential spurious measurements of small particles due to the fragmentation of cloud droplets upon impact with the inlet [Weber et al., 1998]. In another effort to avoid in-cloud sampling, segments where the mean relative humidity of the air exceeded 95% were omitted, following the procedure of Shinozuka et al. [2004]. In total there were 49 segments which met all the requirements for analysis. The flight path of the plane is shown in Figure 5.1, with the mean location of each of the segments indicated in red.

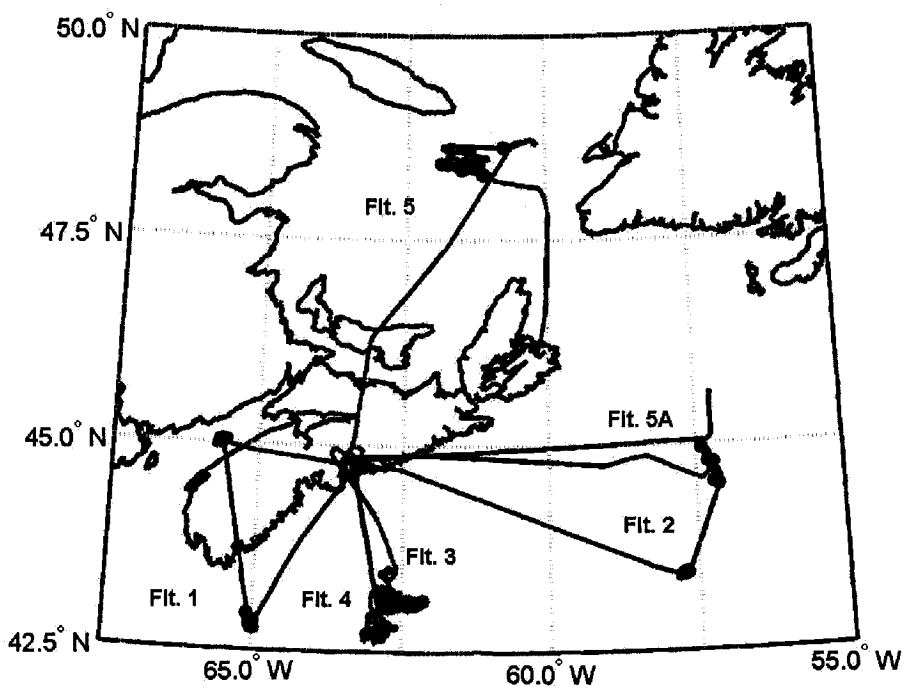

Figure 5.1: The path of the flights from October 13-17. The regions discussed here are marked in red. The data collection software was not functioning for most of the flight marked 5A from Halifax to Sidney, and as such these data are not analyzed.

Chapter 6

The Closure Experiment

6.1 Analysis

6.1.1 A Case Study

In order to illustrate clearly the method used, all of the measurements and calculations will be explained for one of the points considered for closure, the first data point from Flight #1. Firstly, the aerosol number concentration distribution averaged over this time is shown in Figure 6.1, along with the surface area distribution. As compared to Figure 3.5, the coarse mode is greatly attenuated, with almost no particles being measured above 2 μm. This loss appears to be due to the effect of the inlet, which is in keeping with the findings of Blomquist et al. [2001], who found that for the NCAR Community Aerosol Inlet had a 3 μm 50% size cut, and 70-90% of the sea salt mass was lost. As it is an inlet effect, it affects all the measurements taken inside the aircraft on all days, including the nephelometer. As such, closure should still be attainable within this limited size regime.

The next thing to be considered is the chemical constituents measured over the course of this time period. The total mass measured by the AMS and that inferred from the mass concentration distributions agree well when considering only those particles with an diameter less than 0.6 μm, which corresponds to the region which the AMS can measure. With a submicron density of 1.62 g cm^{-3} (based upon the chemical speciation) the size distribution gives a mass concentration of 4.5 μg m^{-3}, while the AMS measures 4.2 μg m^{-3}. These agree within less than 10%, which is well within the uncertainties of the two methods. However they should not necessarily agree as the AMS is unable to measure sea salt. The mass concentration distribution using each method can be seen in Figure 6.2, with the individual species masses for the AMS constituents included as well. This particular segment shows

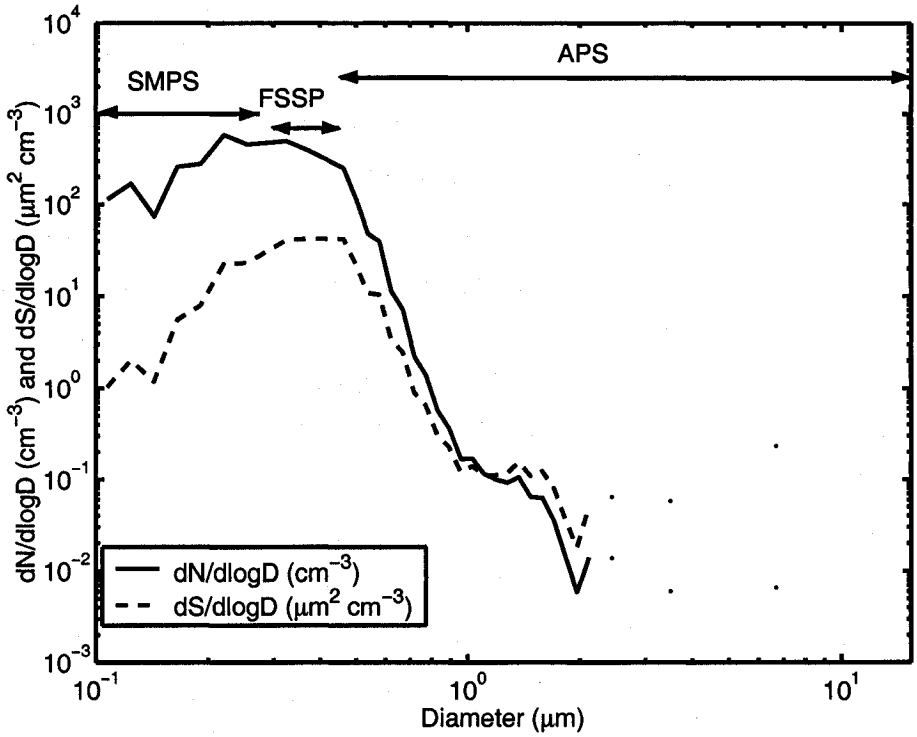

Figure 6.1: The number and surface area concentrations for the example case chosen from Flight #1. The diameter regions measured by each of the sizing instruments, the SMPS, FSSP and APS, are indicated with the arrows.

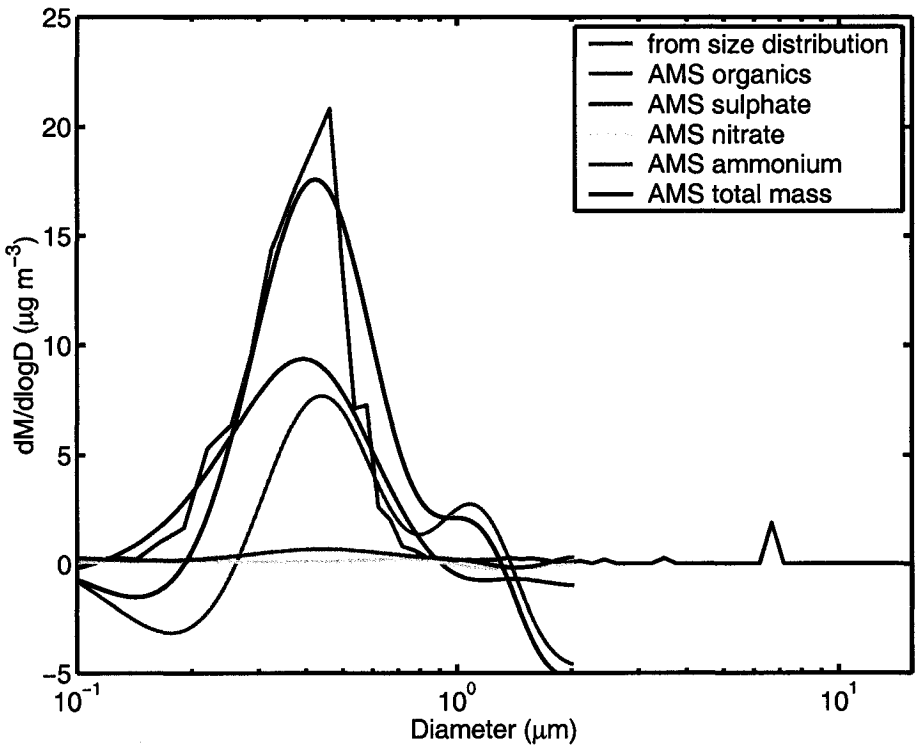

Figure 6.2: The mass concentration distributions as calculated based upon the size distributions (blue) and from the AMS measurements (black) for the case chosen from Flight #1. The mass concentrations of individual species are shown as well: ammonium (brown), nitrate (orange), sulphate (red), and organics (green).

a high concentration of organics along with the dominant sulphate.

In general the size distributions agree quite well. Since the mass distributions for the AMS are inferred from very few particles, the statistics are not very robust when considering only one record, as is the case here. The individual species show unphysical negative mass concentrations at certain sizes as a result of this, but the sum over the whole size range is positive. As such, the submicron fractional contribution of each AMS-derived constituent is based upon the size-integrated mass concentrations. Again, any missing mass is attributed to sea salt, which cannot be measured by the AMS. All supermicron particles are treated as sea salt, which is reasonable for the marine environment (e.g., Murphy et al. [1998]). These fractional contributions are then directly employed in the scattering calculations.

Table 6.1: The assumed values for the real and imaginary parts of the index of refraction of the organic component, n and k respectively, calculated according to Erlick et al. [2001].

λ (μm)	n	k
0.45	1.437	3.129×10^{-4}
0.55	1.432	3.754×10^{-4}
0.70	1.430	4.380×10^{-4}

With these assumptions as to the chemistry of the aerosols as well as the size distributions as given above, the scattering and backscattering coefficients can now be calculated. The complex indices of refraction for ammonium sulphate, sea salt and nitrate are known (for example Tang [1997], Toon et al. [1976]), whereas assumptions need to be made as to the organic constituents. Here the model of Erlick et al. [2001] is followed, where the real part of the refractive index of organic carbon is based on that of octacosanoic acid at 550 nm from Weast et al. [1972], and it is assumed to vary with respect to wavelength in the same manner as does water [Seinfeld and Pandis, 1998]. The imaginary part is taken as the imaginary part of water-soluble components given in d'Almeida et al. [1991]. The complex indices of refraction used for the organic component are given in Table 6.1.

Based upon these data and Mie calculations, the resulting values for the calculated total scattering and backscattering coefficients (σ_{spc} and σ_{bspc} respectively) can then be calculated. In order to have a meaningful comparison with the measured values, the measured values must first be corrected for the problem of angular truncation. The method adopted here is that described by Equations 4.1 and 4.2, with which a correction factor, c, is determined based upon the ratio of the calculated scattering coefficient, σ_{spc}, and the calculated truncated scattering coefficient, σ_{spt}.

6.1.2 All the Data

The procedure described in section 6.1.1 was carried out for all 49 segments of clear, level flight. In all cases the measured results were multiplied by the correction

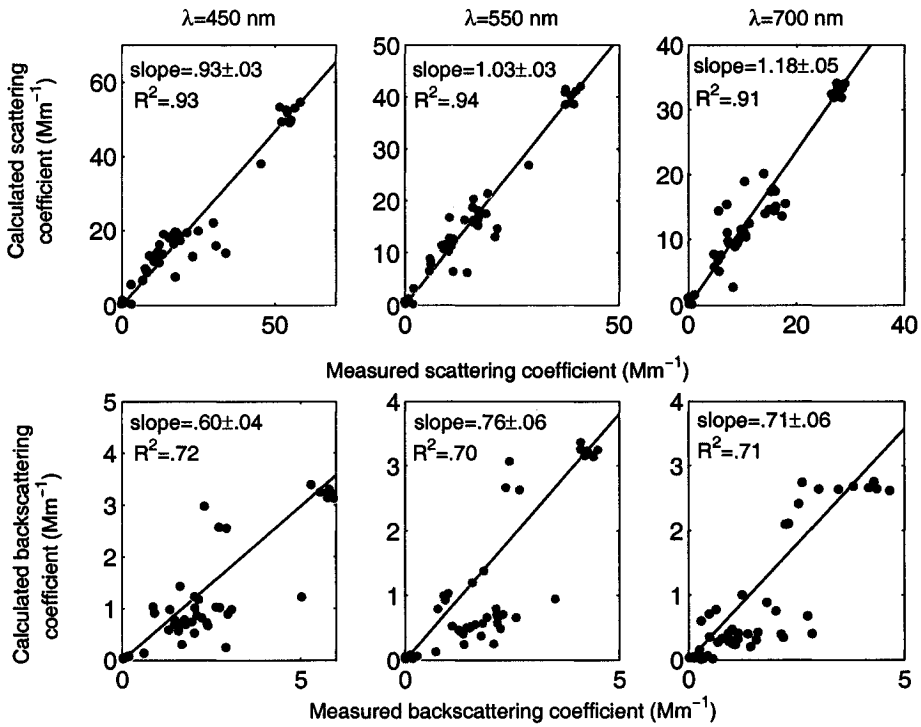

Figure 6.3: The upper three panels show calculated scattering coefficients plotted against the measured scattering coefficients for each of the three wavelengths, with linear fits plotted in black. The lower three panels show the same plots but for backscattering coefficients.

factor giving by Equations 4.1 and 4.2. The comparison of calculated and measured values for total scattering and backscattering is shown in Figure 6.3.

The slope and R^2 value of each scatter plot were determined through linear regression and these values appear on each of the panels in Figure 6.3. A y-intercept of zero was assumed. As can be seen, the total scattering shows significantly better correlation than does the backscattering, with the lowest R^2 value being 0.91, for λ=700 nm. Of the three total scattering cases, its slope also deviates the most from unity, with the calculated values being systematically high. On the contrary, the slope of the line for the blue total scattering case is less than one, suggesting that the calculated values are too low. In the centre is the case for green light, with the best agreement of the three. This systematic error as a function of wavelength suggests that the chemical speciation may be incorrect, as different constituents have

different wavelength dependence. The sensitivity of the calculated results to the chemical speciation is discussed in the following section.

The backscattering coefficients have much lower R^2 values and substantially lower slopes, with very poor agreement. The low slope values suggest that the backscattering coefficient is systematically underestimated by 30-65%. This significant difference is not something that can reasonably be compensated for through either different chemical speciation or uncertainties in the sizing. Previous studies analyzing point closure have also found consistent underestimation of calculated backscattering coefficients based on dry aerosol sampling in the marine environments [Fridlind and Jacobson, 2003, Quinn and Coffman, 1998, Quinn et al., 1995].

This may be due to assumptions about particle sphericity, which is fundamental to Mie calculations. Since the particles were dried during sampling by the SMPS, APS and nephelometer, their shapes are likely to have been somewhat non-spherical. Generally speaking, particle non-sphericity has a substantially greater impact on backscattering than total scattering (e.g. Pilinis and Li [1998], Mishchenko et al. [1997]), which might be able to explain the results here. Though previous studies had some success attaining closure with models of non-spherical particles, such as that of Pollack and Cuzzi [1980], no attempt was made here to model the particles as non-spheres. Since there are no measurements of the scattering phase function of the ambient aerosols, it is difficult to determine if the solution to the inverse problem assuming non-spherical particles would be correct. Such work is not undertaken here.

The poor agreeement in the case of the backscattering could also be related to the low signal-to-noise ratio. Though in ideal situations the detection limit of the nephelometer is on the order of 10^{-7}, the noise in the signal seen throughout the flights was much higher, and signals below $\sim 10^{-6}$ were indistinguishable from zero. As the mean ratio of the measured backscattering to total scattering was only 0.14 ± 0.08, the much smaller backscattering coefficient was more likely to have been obscured by the large amount of noise in the measurement.

6.2 Closure Analysis

In order to statistically assess the agreement between the measurements and the calculations it is necessary to accurately estimate the uncertainties in each. In order to do this, the difference between the calculated and measured values is compared to the magnitude of the estimated uncertainty in each. The condition for closure, based on Fridlind and Jacobson [2003], is expressed as:

$$-(\delta\sigma_{sp}^{-} + \delta\sigma_{spc}^{+}) < (\sigma_{spc} - \sigma_{sp}) < (\delta\sigma_{sp}^{+} + \delta\sigma_{spc}^{-}), \tag{6.1}$$

where $\delta\sigma_{sp}^{+/-}$ and $\delta\sigma_{spc}^{+/-}$ are the uncertainties in the measured and calculated scattering values respectively. The superscript, + or −, indicates whether the uncertainty is for overestimation or underestimation. Equation 6.1 is assessed for each point to test for closure. If the conditional statement is satisfied this means that any difference between the calculated and measured values is less than the sum of the estimated uncertainties in the two values, and closure is attained.

The uncertainty in the nephelometer measurement is simply the truncation corrected measured value multiplied by the estimated uncertainty range, here given as +15/−15%, after Fridlind and Jacobson [2003], whose uncertainty values were derived for aircraft data. The uncertainty in the calculated value is more complicated, as it represents the combination of uncertainties in particle sizing, counting, RH measurements, and analysis of chemical speciation. Firstly, estimations are made of the uncertainties in each of these measured values used as input to the calculations. Then the scattering calculations for each point are repeated based upon the upper and lower limit of each of these measured quantities in turn, giving an idea of the uncertainty in the calculated value based upon each of the measured values. Finally, the upper uncertainty boundary for each calculated value, $\delta\sigma_{spc}^{+}$, was calculated as the square root of the sum of the squared positive uncertainties, based on the different measured quantities. The lower uncertainty boundary, $\delta\sigma_{spc}^{+}$, was calculated likewise using the negative uncertainties of each measured value. Each of these uncertainties was calculated for each of the 49 points. The median uncertainty values, expressed as percentage of the calculated scatterin and backscattering coefficient values, are given in Table 6.2.

Table 6.2: Estimated uncertainties in the measured scattering values, and median uncertainties in the calculated scattering values based upon estimated uncertainties in the particle counting, particle sizing, relative humidity, chemical speciation, and a combination of these effects.

Total scattering			
λ (nm)	450	550	700
Quantity	$\delta\sigma_{spc}^{+/-}$(%)	$\delta\sigma_{spc}^{+/-}$(%)	$\delta\sigma_{spc}^{+/-}$(%)
particle counting (±10%)	10.0/10.0	10.0/10.0	10.0/10.0
particle sizing (±2.2-9.0%)†	18.2/16.4	17.5/15.5	17.3/14.9
relative humidity (±10%)	3.9/4.2	3.5/3.8	4.1/4.2
chemical speciation (±50%)‡	0.7/1.2	0.7/1.2	1.0/1.7
combined error (%)	21.2/20.0	21.0/19.3	20.5/18.6
Quantity	$\delta\sigma_{sp}^{+/-}$(%)	$\delta\sigma_{sp}^{+/-}$(%)	$\delta\sigma_{sp}^{+/-}$(%)
nephelometer (±15.0%)	15.0/15.0	15.0/15.0	15.0/15.0
Backscattering			
λ (nm)	450	550	700
Quantity	$\delta\sigma_{bspc}^{+/-}$(%)	$\delta\sigma_{bspc}^{+/-}$(%)	$\delta\sigma_{bspc}^{+/-}$(%)
particle counting (±10%)	10.0/10.0	10.0/10.0	10.0/10.0
particle sizing (±2.2-9.0%)†	14.5/13.2	13.0/12.0	10.7/9.7
relative humidity (±10%)	3.6/3.6	3.7/3.9	3.7/3.6
chemical speciation (±50%)‡	3.3/5.2	1.7/2.8	0.9/1.6
combined error (%)	18.1/18.3	17.1/16.8	15.6/14.9
Quantity	$\delta\sigma_{bsp}^{+/-}$(%)	$\delta\sigma_{bsp}^{+/-}$(%)	$\delta\sigma_{bsp}^{+/-}$(%)
nephelometer (±15.0%)	15.0/15.0	15.0/15.0	15.0/15.0

†The error on the sizing of the particles is half the bin width divided by the midpoint diameter.
‡Each of the four species measured by the AMS had the mass changed by ±50% in turn, and the effect of all four are here combined as the root of a sum of squares.

The uncertainty in the counting efficiency is estimated at ±10%. This results in an uncertainty in the calculated value of ±10% since the scattering coefficient is directly proportional to the number concentration, as is given in Equation 2.12. The uncertainty in the sizing of the particles is calculated as half the bin width divided by the midpoint diameter, giving an uncertainty in the geometric diameter ranging from ±2.2-9.0% depending upon the size bin. This number is magnified in the calculations however, since the scattering coefficient is proportional to the diameter to the power of two. The uncertainty in the measured RH is estimated at ±10%. This has only a small effect on the calculated values since only a few size bins in the distribution, those measured by the FSSP, are affected by the hygroscopic correction. The uncertainty in the chemical speciation was estimated to be quite large, based upon the fluctuations seen between consecutive measurements and the fact that only one AMS averaging period is used for each point. In order to explore the effect that this uncertainty might have, the mass of each chemical group was changed by ±50%, the mass fraction was recalculated, and the scattering calculation was repeated. The chemical groups in question are sea salt, ammonium sulphate, nitrate, and organics. The total mass was not changed, as that is calculated according to the size distribution, and the AMS speciation is used only to determine the submicron fraction of each chemical group. This was carried out for each of the four groups in turn, and the uncertainties derived from each were combined as the root of a sum of squares.

After this analysis, each point was analyzed for closure following Equation 6.1. For the total scattering coefficient, closure was attained for >70% of all the points, with the best agreement being for green light, with closure attained within uncertainties for 41 of 49 points. The results were much poorer for backscattering, as would be expected based upon Figure 6.3, with less than 40% of the points attained closure for backscattering. Again, the agreement was best for green light, though only 17 of 49 points agreed within uncertainty for the calculated and measured backscattering coefficients. These results are summarized in Table 6.3, along with the median difference between the calculated and measured values, with the percentage calculated relative to the measured value.

Table 6.3: The percentage of points which attained closure, the number of points which attainted closure, and the median error between the calculated value and the measured value are given for the entire campaign, as well as for each flight.

	Total scattering			Backscattering		
λ (nm)	450	550	700	450	550	700
Total for all flights (49 points)						
% with closure	73.5	83.7	71.4	14.3	34.7	22.4
points with closure	36	41	35	7	17	11
median error (%)	-2.1	2.6	12.6	-59.0	-65.5	-63.2
Flight #1 (10 points)						
% with closure	30.0	60.0	30.0	0.0	0.0	10.0
points with closure	3	6	3	0	0	1
median error (%)	-47.4	-11.9	45.9	-73.7	-79.6	-80.1
Flight #2 (10 points)						
% with closure	90.0	90.0	90.0	0.0	60.0	30.0
points with closure	9	9	9	0	6	3
median error (%)	-7.0	1.9	17.6	-45.6	-25.5	-36.4
Flight #3 (15 points)						
% with closure	86.7	100.0	100.0	0.0	0.0	0.0
points with closure	13	15	15	0	0	0
median error (%)	9.2	1.7	-1.8	-62.8	-68.8	-72.8
Flight #4 (5 points)						
% with closure	60.0	60.0	40.0	60.0	60.0	80.0
points with closure	3	3	2	3	3	4
median error (%)	-10.6	5.7	8.1	-13.7	11.8	-7.1
Flight #5 (9 points)						
% with closure	88.9	88.9	66.7	44.4	88.9	33.3
points with closure	8	8	6	4	8	3
median error (%)	13.2	15.3	23.0	-40.7	-1.1	-51.8

The results shown in Table 6.3 indicate that the agreement between the calculated and measured values varies greatly from day to day. Flights #2, #3 and #5 clearly show better agreement for total scattering than do Flights #1 and #4. In order to explore the difference between the closure for the various flights, the point closure, magnitude of error, and total scattering coefficient for λ=550 nm are compared as a function of altitude in Figure 6.4.

From Figure 6.4 it can be seen that six of the eight points for which closure was not attained occur above 700 m. This was above the stratocumulus cloud base for all of these flights, and generally there were fewer aerosols at these altitudes. This is seen in the drop off of the total scattering signal shown in the third panel of Figure 6.4. This accounts for the poor agreement for Flight #4 – the two points for which closure was not attained both occur above 1400 m. Since only five measurements were considered from this flight, only 60% closure is attained for green light.

In general, the calculated and measured values agreed better for measurements of larger magnitude. This could be related to the high amount of noise in the measurements, particularly the scattering measurements, as was discussed before to account for the poor closure seen for backscattering coefficients. Thus a smaller signal is more easily lost in the noise. This smaller measured signal at higher altitudes also accounts for the large percentage error value seen for these data as a relatively small absolute error can be many hundreds of percent of a small number.

As for the two measurements taken below cloud which did not attain closure, they are both from Flight #1 which, of all the flights, showed the poorest agreement between the measured and calculated values. In order to analyze this further, it is necessary to compare the aerosols measured on each of the days, both their size distributions and chemical constituents.

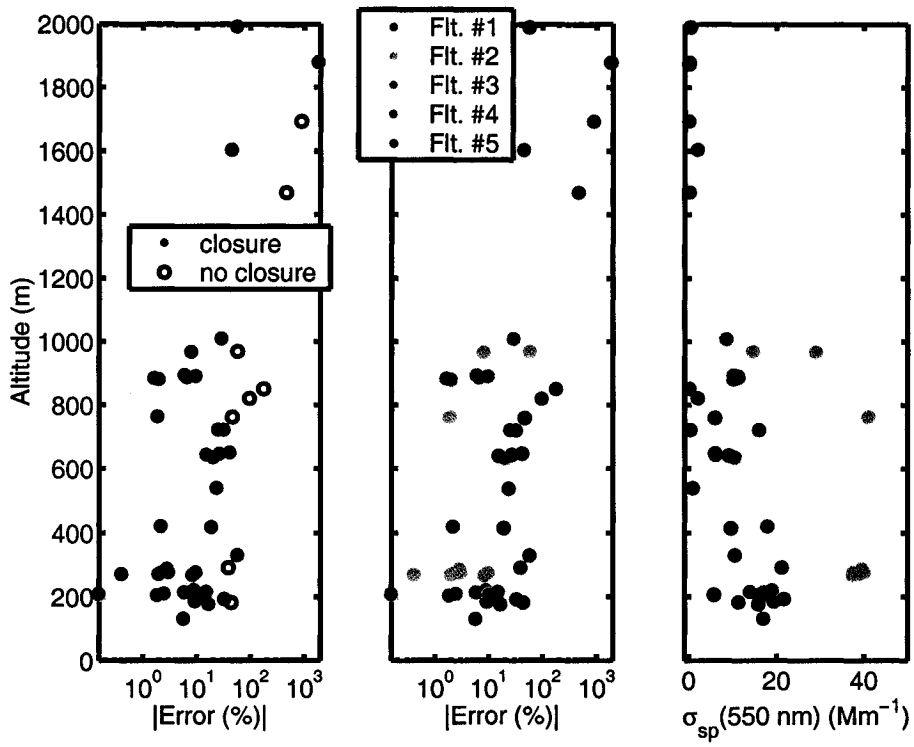

Figure 6.4: The leftmost panel shows the percentage absolute difference between the calculated and measured scattering coefficient, relative to the measured value, as a function of altitude. The points for which closure is attained are shown in blue, those for which closure was not attained within estimated uncertainties are shown as red circles. The centre panel shows the same points, coloured according to on which flight they were collected. The panel at the right shows the measured scattering coefficient as a function of altitude, again colour-coded according to flight. All data are for λ=550 nm. The errors are shown on a logarithmic scale, while the scattering coefficient is plotted on a linear scale.

6.3 Intercomparison of Measured Aerosols

6.3.1 Chemical Signatures of Different Flights

Though the flights analyzed in this study took place within five days of each other, they displayed somewhat different aerosol characteristics. The above cloud and below cloud points were averaged separately for each of the days, and the inferred mass fractionation and total mass, as determined from the averaged size distributions were compared. This comparison in shown in Figure 6.5, for both the above and below cloud samples. Two separate records are compared for Flight #1 as two different geographical regions were sampled; over the Bay of Fundy and above the waters southwest of Halifax, as can be seen in Figure 5.1. The data from these two regions are labelled 1A and 1B respectively in Figure 6.5.

With the exception of the data from the first flight, the mass fraction of each of the flights below cloud base is seen to be dominated by the supermicron particles, assumed to consist entirely of sea salt. The mass above cloud base is also dominated by sea salt for Flights #2 and #5, though the total mass concentration is substantially lower in both cases. Of note is the scarcity of aerosol mass above cloud during Flight #1, and the lack of supermicron aerosols below cloud as well. The aerosol mass on this day was dominated by submicron ammonium sulphate, with some contribution from organics. A stronger organic contribution was seen on both Flights #2 and #4. Flight #5 has the lowest below cloud mass contribution from organics and nitrate, with even the submicron mass dominated by sea salt.

In order to determine the source of the air, back-trajectories were calculated using the National Oceanic and Atmospheric Administration (NOAA) Air Resources Laboratory's HYbrid Single-Particle Lagrangian Integrated Trajectory (HYSPLIT, www.arl.noaa.gov). The back-trajectories for the 48 hours preceding the measurements are shown in Figure 6.6. Those shown in blue are measurements taken below cloud base while those in red are taken above cloud. The difference between the back-trajectories of the above and below cloud measurements is minor for all the flights. The trajectories also indicate that the altitude of each air mass is nearly unchanged over the past 48 hours (not shown), indicating stability.

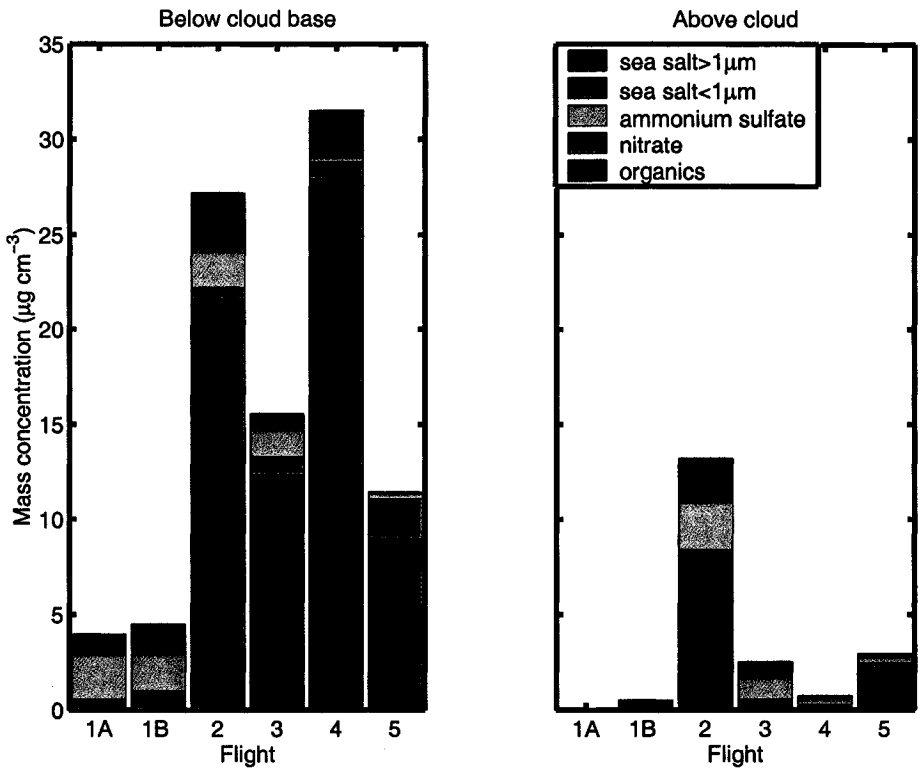

Figure 6.5: The plot on the left shows the mass concentration by species for the data collected below cloud base, while that on the right is for above cloud data. The labels 1A and 1B are to differentiate between data collected during Flight #1 over the Bay of Fundy (A) and over the waters southwest of Halifax (B). The submicron speciation is based upon AMS measurements, with any mass unaccounted for treated as sea salt. All supermicron mass is assumed to be sea salt.

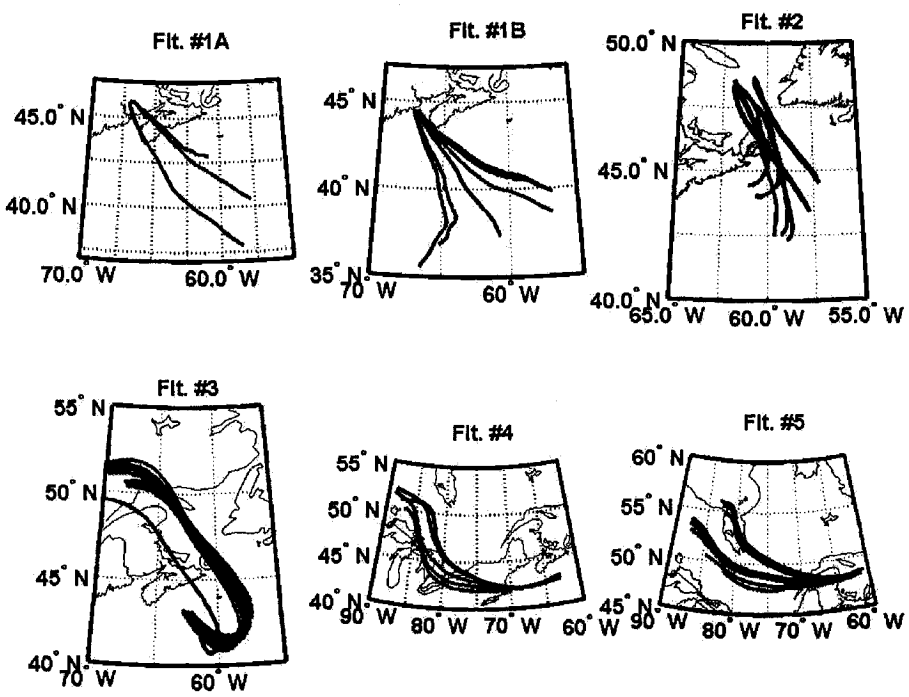

Figure 6.6: Plots of 48 hour back-trajectories generated using the NOAA HYSPLIT model. The lines in blue indicate the back-trajectories for the measurements taken below cloud base, while those in red are for the measurements taken above cloud. Flights #1A and #1B are following the same convention as in Figure 6.5.

Looking at the back-trajectories in Figure 6.6 it seems surprising that there was such little sea salt and supermicron mass attributed to Flight #1B, given that the air had spent the previous 48 hours over the ocean to the south of Nova Scotia. This is less true of Flight #1A, as the air passed over the western portion of Nova Scotia before reaching the Bay of Fundy. There is a slightly higher supermicron contribution to the mass on Flight #1B, but it is still an order of magnitude smaller than the other flights. This may be due to drizzle on this day washing out the large, hygroscopic sea salt aerosols. In analyzing 2-Dimensional Cloud Droplet Imaging Probe data from Flights #1 and #2, Lehr [2005] found an order of magnitude more drizzle-sized droplets measured within the clouds on the first flight. Analysis of cloud radar reflectivities also indicated many more regions where the reflectivity exceeded -15 dBZ, which is an indication of clouds likely to contain drizzle-sized droplets [Wang and Geerts, 2003].

The back-trajectory for Flight #2 shows the air mass changing directions, initially coming from the south as in Flight #1, passing over Cape Breton, then reversing headings and returning from the north. This indicates a primarily marine source with possible continental influence. This may be related to the high concentrations of organics on this day, though it is not clear if the organics are anthropogenic or biogenic. The back-trajectory for Flight # 3 begins over Eastern Quebec 48 hours before, then passes over the Gulf of St. Lawrence and Nova Scotia before ending up over the ocean. The back-trajectory for Flight #4 indicates a potential for continental pollution as it is shown to pass over the Great Lakes region and over the highly urbanized northeastern United States before continuing east to the waters south of Nova Scotia. However the data from this day have the lowest concentrations of ammonium sulphate and the highest concentration of sea salt. There is a substantial organic contribution as well. Finally, the back-trajectory from Flight #5 indicates that the air passed over northern Quebec and Ontario on its way to the Gulf of St. Lawrence west of Newfoundland.

An analysis of the wind speeds measured during the flights sheds some light on the difference between the the amount of sea salt on various days as shown in Figure 6.5. Figure 6.7 shows the wind speed as a function of altitude for each of

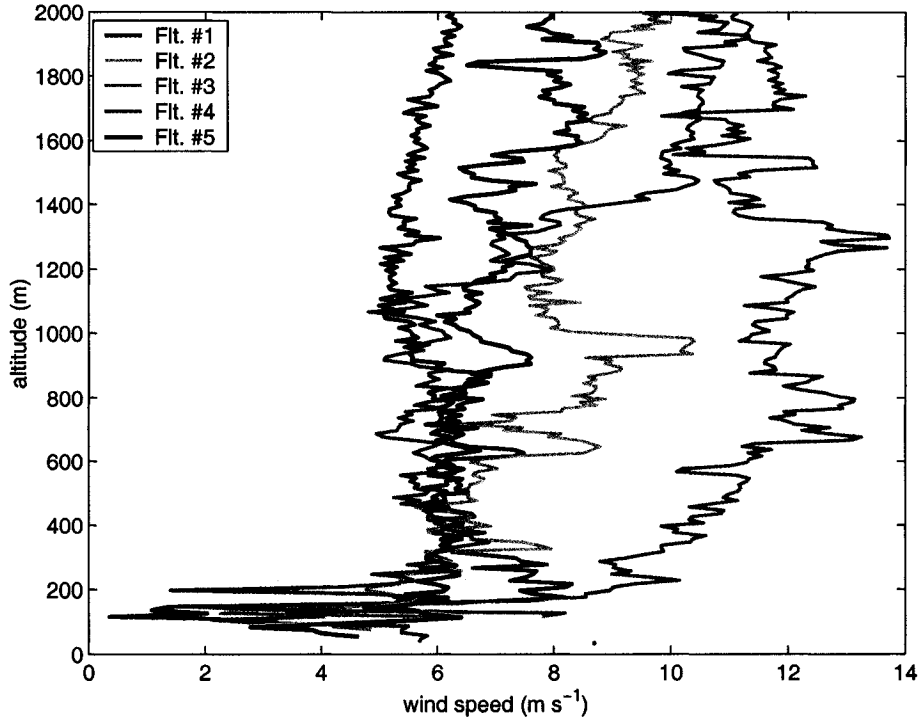

Figure 6.7: The wind speed as a function of altitude, with all the data on each day averaged in 10 m bins.

the flights at altitudes up to 2000 m. This is a combination of the measurements made throughout all the profiles, with the wind speeds binned and averaged into 10 m altitude increments. Though different flights had different lowest altitudes, a difference between the wind speeds at the lower altitudes can be seen. Looking at only the lowest altitudes measured for each day, the wind speed for Flight # 1 is clearly lower than on the other days. However this does not provide much insight into the wind speeds at the surface, where the droplet to particle conversion which produces sea salt aerosols takes place.

To determine the wind speeds closer to the surface, SSM/I (Special Sensor Microwave Imager) data were used. These data are preferable to buoy or radiosonde data as they cover more of the geographical regions in which the data were collected. The wind speed at 10 m above sea level is inferred based upon the microwave brightness temperatures measured at 7 wavelengths by an instrument

mounted on a polar-orbiting satellite. The data discussed here were collected by satellites F14 and F15 during morning scans on October 13 to 17. SSM/I data are produced by Remote Sensing Systems and sponsored by the NASA Earth Science REASoN DISCOVER Project. Data are available at remss.com.

The results are shown in Figure 6.8, with the approximate sampling regions indicated on each of the plots. The scattered pixels with missing data (in black) are due to precipitation during the sampling or proximity to the shoreline, while the larger areas in black are regions which the satellite did not pass during its samples that day. The 10 m wind speed in the more southerly region sampled during Flight #1, on October 13, was approximately 5-7 m s^{-1}. (The other region sampled on this day, the Bay of Fundy, is not large enough to be sampled with this method.) This wind speed is considerably lower than those seen on the other days, which were roughly 10-15 m s^{-1}. Lower wind speeds are also seen during the day preceding Flight #1 (not shown), suggesting further that this could be the cause of the lower concentrations of sea salt particles on that day.

6.3.2 Size Distributions of the Different Flights

The size distributions were averaged in the same way as the mass concentrations, into above and below cloud measurements for each of the regions studied. The results for the below cloud measurements are shown in Figure 6.9, and those for the above cloud measurements are shown in Figure 6.10.

For the below cloud data the large difference between the supermicron aerosol concentrations for Flight #1 and those on the other days can be clearly seen, with as much as a thousand times more particles counted between 1-3 μm on Flight #3 as on Flight #1. This of course impacts both the mass concentration and the scattering calculations.

The above cloud aerosol size distributions shown in Figure 6.10 show a substantial reduction in supermicron aerosol number concentration from the below cloud distributions in Figure 6.9, particularly in the data from Flight #1. In fact almost no aerosols were measured at all for Flight #1A, and the submicron concentrations during Flight #1B dropped by over an order of magnitude. This low

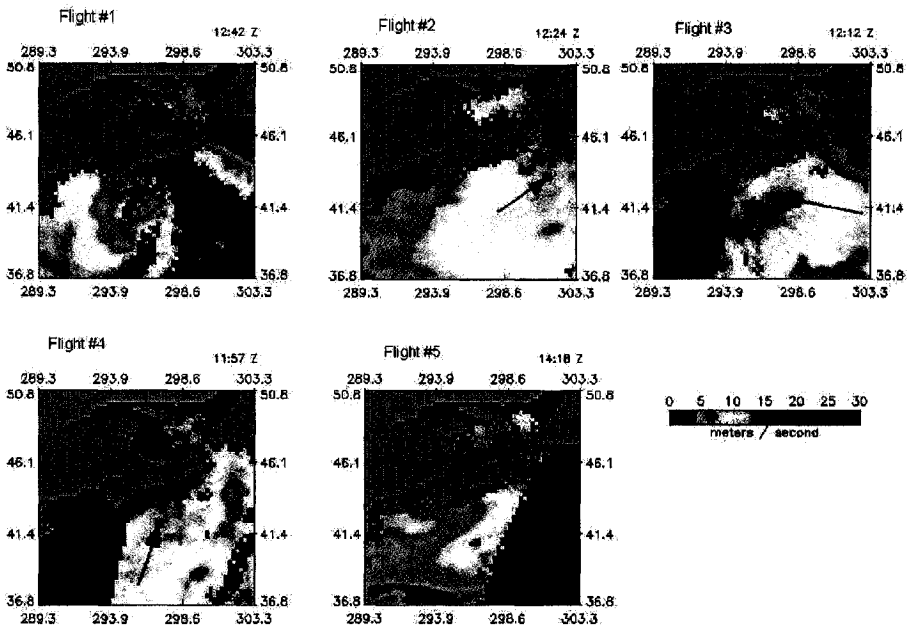

Figure 6.8: The wind speed for each of the days as determined by satellite measurements of microwave brightness temperatures. The time of the scan is shown at the upper right of each map, in UTC. The approximate regions at which the aircraft measurements were taken are indicated with the red arrows.

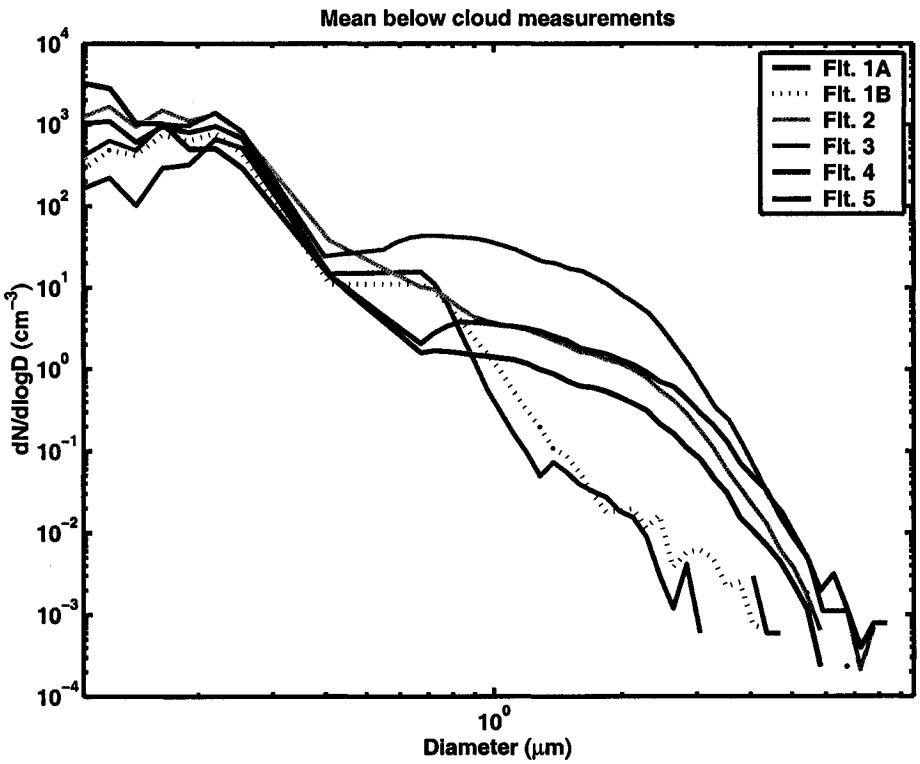

Figure 6.9: The dN/dlogD aerosol concentrations averaged for the below cloud data measured on each of the flights. The data from Flight #1 is subdivided into #1A and #1B in the same manner as in Figure 5.1.

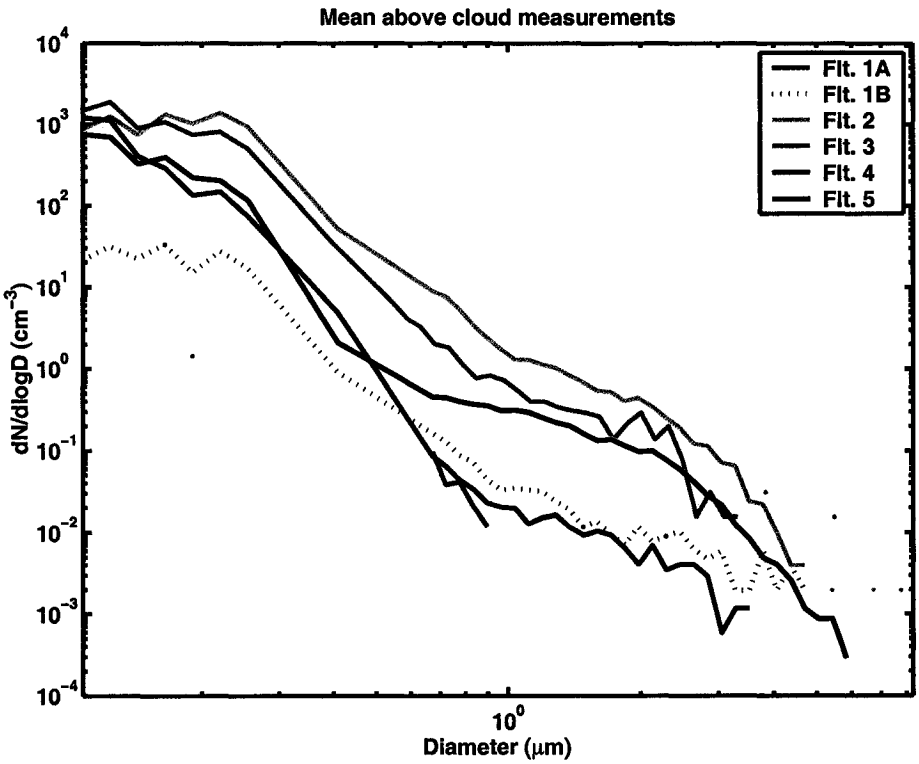

Figure 6.10: The same information as in Figure 6.9, but for the above cloud data.

concentration of larger particles during Flight #1 is likely due to the lower surface wind speeds, as shown in Figure 6.8. This reduces the rate of droplet to particle formation of sea salt aerosols, and allows more aerosols to settle out. The other flights also indicate a reduction in the number concentration, though the effect is more clearly seen for supermicron particles. The small number of particles measured during Flight #1 also makes the data somewhat less statistically reliable, which may also have contributed to the poor closure results on this day.

6.3.3 Scattering Apportionment by Size

To compare the contribution of the different sized particles to the calculated scattering and backscattering coefficients, the scattering coefficient distributions are plotted against the diameter of the particle. Again, the data are averaged according to above and below cloud values for each region.

The data shown in Figure 6.11 indicate that below cloud, the total scattering is dominated by the submicron mode, though there is a strong signal in the supermicron mode on Flights #2, #4 and #5. The calculated backscattering is dominated by the supermicron particles for those same three flights as well. As for the above cloud data, shown in Figure 6.12, the small signal from Flight #1 is not even visible. The submicron component dominates the total scattering for all the flights, though a very strong supermicron component to the backscattering coefficient is seen for Flights #2 and #5.

6.4 Accounting for the Unmeasured Aerosols

Looking at the size distributions plotted in the previous section, it is often apparant that there is a sharp decrease in particle concentrations for sizes above 2 μm. As previously mentioned, this is attributed to losses due to the inlet, and affects all the instruments inside the aircraft. Though this allows for consistent comparison between these instruments, it does not necessarily provide an accurate picture of the ambient aerosol, or its scattering properties.

In order to estimate what sort of effect this might have, the size distributions

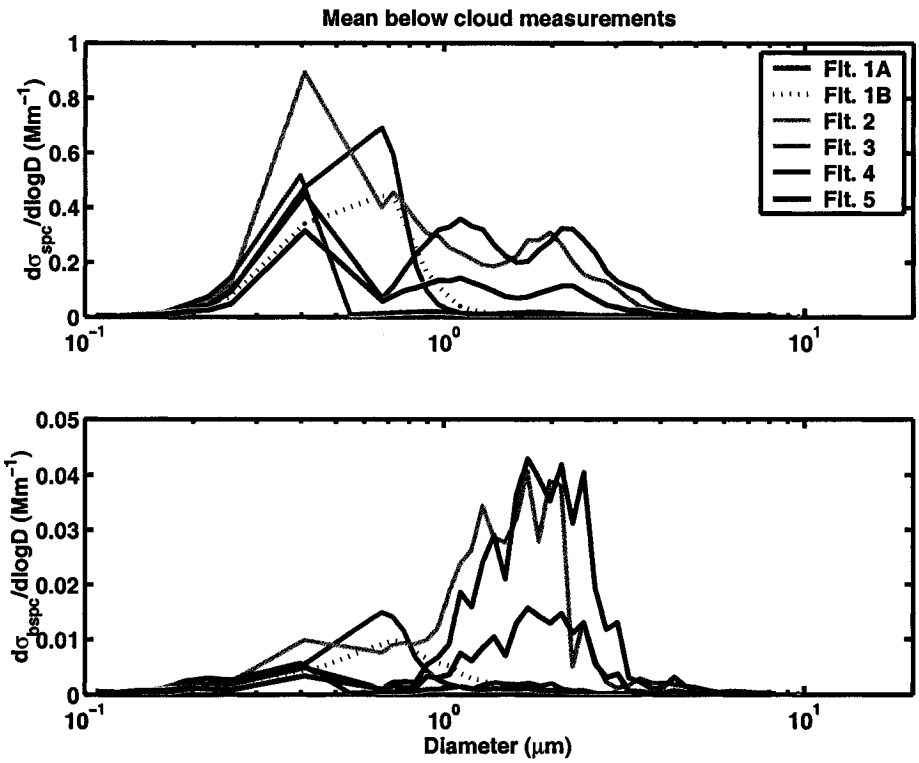

Figure 6.11: The calculated scattering and backscattering coefficients as a function of diameter for each of the regions studied. The data are averaged over the measurements taken below cloud base for λ=550 nm.

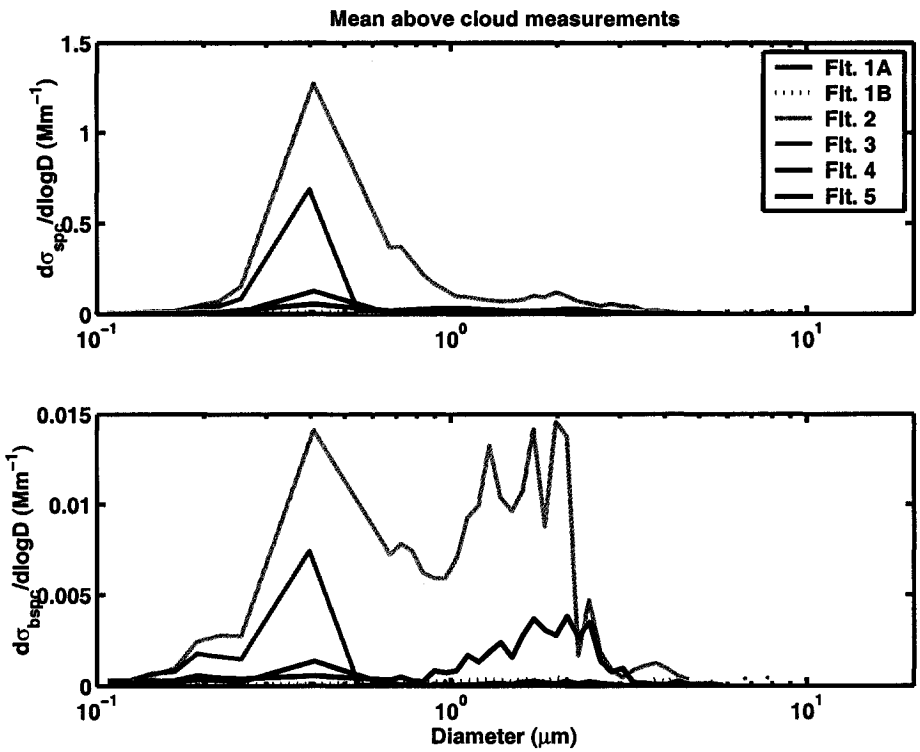

Figure 6.12: The calculated scattering and backscattering coefficients as a function of diameter for each of the regions studied. This plot shows the mean data collected above cloud for λ=550 nm.

were recreated and the scattering and backscattering coefficients were recalculated using the size distributions provided by the FSSP rather than the APS for particles larger than 0.30 μm. Since the FSSP was mounted outside of the aircraft it would not experience the losses associated with the inlet. As previously described, the FSSP distribution was corrected for hygroscopic effects using Equation 5.3, and the dry diameter is considered here.

To give an example of the kind of effect that this can have, the below cloud size distribution and the contribution to σ_{spc} and σ_{bspc} as a function of diameter are replotted for the below cloud data of Flight #3 using both the original size distribution as well as that utilizing the FSSP for all particles larger than those measured by the SMPS. The result is shown in Figure 6.13.

Clearly, the calculated scattering and backscattering coefficients when summed over all the diameters will be higher for the FSSP size distribution than for the APS size distribution. This suggests that the actual ambient total scattering and backscattering coefficients may be considerably higher than the nephelometer is able to measure due to sampling losses in the inlet or tubing.

To assess the possible impact of these losses, the following quantities were calculated for each flight segment for both size distributions: aerosol number concentration, aerosol mass concentration, fine fraction of mass, σ_{spc}, σ_{bspc}, and fine fraction contribution to scattering. The percentage change for each of these numbers due to the new size distribution is given in Table 6.4. All percentages are calculated relative to the initial APS-derived size distribution. All values given are for λ=550 nm, though similar results are found for the other two wavelengths as well.

The results for the below cloud measurements in Table 6.4 indicate that changing the size distribution to reflect the aerosols outside of the plane rather than inside has quite a significant effect on the calculated scattering coefficients, increasing the below cloud levels for green light anywhere from 14 to 184%. The calculated backscattering coefficient was also found to increase substantially for the measurements made below the cloud base. Generally speaking the effect was the smallest for Flight #1 during which there were not a lot of supermicron aerosols

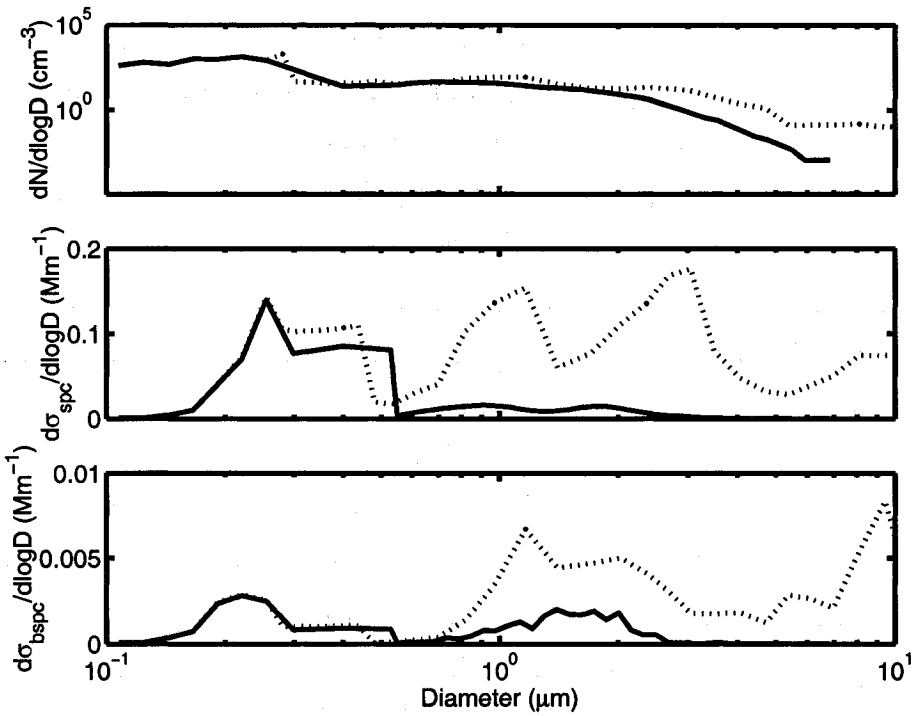

Figure 6.13: The aerosol size distribution (top panel), contribution to total scattering coefficient as a function of particle diameter (middle panel) and backscattering coefficient as a function of diameter (bottom panel). All data shown are for the below cloud mean distribution on Flight #3, and the scattering data are for λ=550 nm. The solid line indicates the original size distribution using the APS, while the dotted line shows the size distribution using the FSSP measurements instead.

Table 6.4: The percentage change in a variety of aerosol quantities due to the use of the FSSP data in the size distribution rather than the APS. Both below cloud and above cloud measurements are presented, and the scattering calculations are for λ=550 nm.

Flight segment	1A	1B	2	3	4	5
Below cloud data						
Number concentration	+14.0	+6.2	+0.1	+0.1	+0.1	+3.0
Mass concentration	+83.4	+131.5	+137.6	+390.6	+231.3	+97.3
Mass fine fraction	-42.7	-83.0	-67.8	-76.0	-70.0	-79.4
σ_{spc}	+14.4	+24.1	+20.0	+182.9	+115.1	+77.4
σ_{spc} fine fraction	-16.1	-42.8	-32.6	-26.8	-3.0	-58.5
σ_{bspc}	+2.4	+19.3	+20.2	+37.0	+15.9	+10.4
σ_{bspc} fine fraction	-68.9	-54.9	-56.5	-51.8	-73.7	-67.0
Above cloud data						
Number concentration	+15.0	+24.8	+1.3	+0.1	0.0	+0.3
Mass concentration	+7.7	+84.4	+74.4	+6.6	-5.8	-6.8
Mass fine fraction	-36.2	-42.6	-32.7	06.7	+2.0	-17.1
σ_{spc}	+41.2	+65.4	+16.3	-6.4	-18.4	-26.3
σ_{spc} fine fraction	-13.1	-51.3	-17.6	-1.2	+7.1	-5.1
σ_{bspc}	+46.9	+8.5	+30.7	-20.3	-4.7	-31.6
σ_{bspc} fine fraction	-27.9	-41.7	-25.2	+2.7	+22.3	+12.0

measured by either the APS or the FSSP.

Table 6.4 also gives the calculated change in the fine particle ($D < 1\mu$m) contribution to both the mass and the scattering and backscattering coefficients. The new size distribution, using the FSSP clearly shows a decrease in the fine particle contributions, indicating that the increase in mass and scattering coefficients is due primarily to higher concentrations of particles greater than 1μm rather than an increase in the concentration of particles between 0.28 and 1.0 μm.

The results for the use of the FSSP for the above cloud measurements are also included in Table 6.4, though here the change is not so constant throughout the flights. This is due to the smaller number of supermicron particles found above the clouds, so that the addition of particles greater than 2 μm has less of an impact. In some cases the calculated scattering and backscattering coefficients are even found to decrease, and the fine fraction contribution to mass and scattering to increase. These anomalous results are believed to be related to uncertainties in the measurements. As there are fewer aerosols at higher altitudes and fewer total measurements taken above cloud the statistics are not as robust.

6.5 Comparison with Cruise Data

From the analysis of the cruise data in Chapter 4 one of the most notable findings was the large correction factor, c, required to account for the angular truncation of the nephelometer. In the data reported from the flights these correction factors have been applied in the reported measured quantities, but merit further attention. Table 6.5 gives the mean values for c and c_b for all three wavelengths, along with the maximum and minimum value for each. The uncertainty given on the mean is one standard deviation.

The numbers are much smaller than those reported for the cruise data, given in Table 4.3, and are more in keeping with those calculated for the theoretical clean or polluted maritime aerosol distributions, as in Table 4.4. However, these correction factors are based upon size distributions using the APS for the supermicron aerosols. As previously discussed, since this instrument was mounted on board the aircraft, aerosols larger than $\sim$2 μm were not well sampled by the inlet. Since

Table 6.5: The mean values of the correction factor for the total scattering and backscattering coefficients, along with their maximum and minimum values, c_{max} and c_{min} respectively. The uncertainty given is one standard error. The first section is based upon the size distribution using the APS for the supermicron aerosols, and the second uses the FSSP instead.

Total scattering			
λ (nm)	450	550	700
size distribution using APS			
mean c	1.45±0.04	1.45±0.03	1.40±0.02
c_{max}	2.03	2.08	2.01
c_{min}	1.16	1.15	1.16
size distribution using FSSP			
mean c	3.28±0.59	3.05±0.47	2.70±0.35
c_{max}	23.8	19.2	15.0
c_{min}	1.15	1.17	1.17
Backscattering			
λ (nm)	450	550	700
size distribution using APS			
mean c	1.39±0.01	1.33±0.01	1.27±0.01
c_{max}	1.52	1.51	1.41
c_{min}	1.15	1.14	1.15
size distribution using FSSP			
mean c	1.55±0.03	1.50±0.03	1.47±0.03
c_{max}	2.08	2.06	2.32
c_{min}	1.16	1.15	1.15

the supermicron particles were primarily responsible for the large correction factors in the cruise data, the loss of these particles may be making their number unreasonably small. To test this the values of c and c_b calculated for the size distributions using the FSSP are also reported in Table 6.5.

The correction factors based upon the FSSP size distribution have larger mean values; roughly twice as large for the total scattering but only slightly larger for the backscattering. This is likely due to the pronounced forward lobe in their scattering phase function of the larger particles, as seen in Figure 4.3, which does not affect the backscattering efficiency. Where the effect of the different size distribution is more notable is in the high value of c_{max}, and the large standard deviation in the mean. This is due to the measurements taken at lower altitudes on flights when there were many large particles, similar to the cruise measurements.

The altitude dependence of the correction factors based upon the two different size distributions is shown in Figure 6.14, for both the total scattering and the backscattering at a wavelength of 550 nm. Also shown is the percentage of the total scattering and backscattering coefficient calculated to result from particles greater than one micron in diameter. Some correlation can be seen between the correction factor and the percentage of the scattering from coarse particles for both the total scattering and the backscattering. The increase in the correction factor due to the use of the FSSP for the measurement coarse particles is clear for both the total scattering and the backscattering, while the increase in the coarse particle contribution to scattering is more pronounced for total scattering than for backscattering. This is also seen in the results in Table 6.4.

At higher altitudes, above about 1 km, the change due to the use of the FSSP measurements is not as clear. In some cases the percentage of scattering due to coarse particles actually decreases, and there is only one measurement for which the coarse particles are responsible for more than 50% of the total scattering and backscattering for green light.

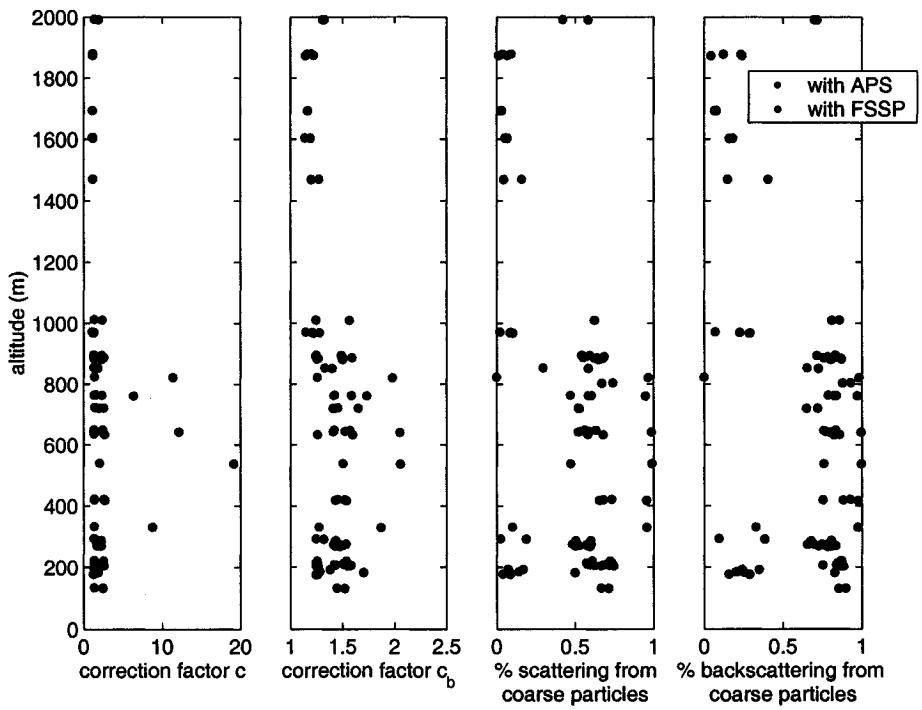

Figure 6.14: The first panel shows the calculated correction factor for total scattering, c, as a function of altitude for both the APS-derived size distribution (in blue) and the FSSP-derived size distribution (in red). The second panel has the same information regarding the correction factor for backscattering (c_b). The third panel shows the percentage of the calculated total scattering attributed to supermicron particles for both size distributions, and the fourth panel has the same quantity for backscattering.

Chapter 7

Absorption by Activated Aerosols

7.1 Background

Up to here, this thesis has focussed on the analysis of measured data from marine environments which, typically, have very high aerosol single-scattering albedos, indicating a scarcity of highly absorbing aerosol species. This is not true of all environments however, particularly in regions where dust or BC – optically absorbing particles – are common.

These absorbing particles can have a very strong effect on climate. Whereas the direct effect of aerosols is typically thought to be a cooling effect, models have estimated that lowering the single-scattering albedo (ω) only slightly changes this forcing from a cooling to a warming effect. If the clouds in the model remain fixed (i.e. no feedbacks), this critical value at which the model's surface temperature rises is found to be approximately 0.90 or 0.85 (Cook and Highwood [2004], Hansen et al. [1997] respectively). If cloud feedbacks are allowed, this value rises up to 0.93 or 0.91. When restricted to the case of marine stratocumulus, Johnson et al. [2004] found a threshold value as high as 0.985, suggesting that even mildly absorbing aerosols can result in a positive forcing. Results from Johnson [2005] suggest that this difference may be due to the difference between using a GCM – as did Cook and Highwood [2004] and Hansen et al. [1997] – or using a large-eddy simulation model, as did Johnson et al. [2004] and Ackerman et al. [2000]. Such low values of ω are not uncommon, with the accumulation mode of measured pollution plumes in southeast Asia having a ω value of approximately 0.84, going down to approximately 0.74 during high-dust events [Clarke et al., 2004].

The effect that this absorption has on clouds is largely uncertain, and seems to depend a great deal on the location of the absorbing aerosols in the atmosphere.

Johnson et al. [2004] found that in the case of marine stratocumulus, placing absorbing aerosol above the boundary layer increased the liquid water path (LWP) leading to a negative semi-direct forcing, whereas placing the absorbing aerosol in the boundary layer decreased the LWP and led to a strong positive forcing.

But these studies are looking at only interstitial BC aerosols, i.e. those not activated and in cloud droplets. Some work has been done examining the role of absorption by activated black carbon. For instance, Chýlek et al. [1996] examined activated black carbon and found it to have a higher specific absorption (absorption per unit mass of BC) than interstitial, or unactivated black carbon. Chuang et al. [2002] developed a parameterization to calculate the ω value for clouds containing BC particles, based upon the volume fraction of BC in the droplets in AGCM simulations and the effective radius of the cloud. This parameterization approximated the results of Mie scattering, without requiring costly iterative calculations each time the result is required. When used in an AGCM the result needs to be calculated at each time step and for each grid box, so the number of calculations can be quite large.

The approach adopted here is similar to that of Chuang et al. [2002], however in place of the parameterization is a look-up table, with values determined based upon Mie calculations. Thus rather than making an approximate calculation each time the result is required, a range of representative values are calculated more precisely once, and one only needs to interpolate between values each time the result is needed.

7.2 Determining the Single-Scattering Albedo of the Cloud

In order to model the properties of clouds containing activated black carbon it is necessary to determine the single-scattering albedo, ω, of a single BC-containing water droplet. Adopting the approach of Chuang et al. [2002], ω is estimated using an effective medium approximation. This approach allows the composite droplet of highly absorbing BC and predominantly scattering water to be treated as a homogeneous "effective medium" with moderate absorptive properties. This is illustrated in a schematic in Figure 7.1.

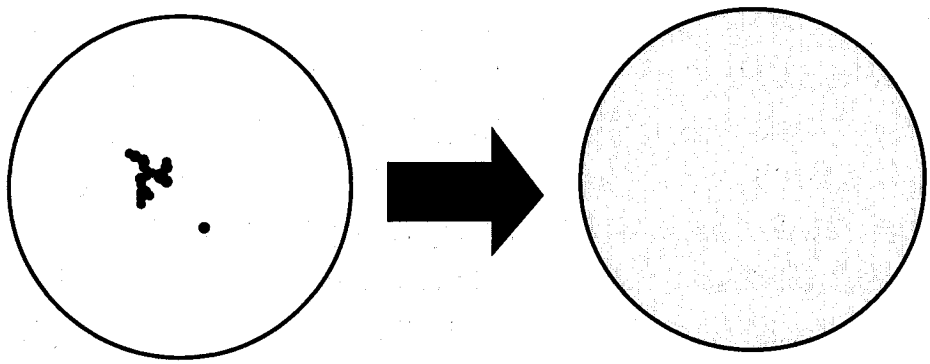

Figure 7.1: A schematic diagram illustration of an effective medium approximation, whereby a composite particle composed of materials of varying optical properties – in this case one highly absorbing and the other not – are treated as a homogeneous material with optical properties determined by a weighted average.

The effective medium approximation used in this case is the Maxwell-Garnett mixing rule [Bohren and Huffman, 1998], which has been shown by Chýlek and Videen [1998] to provide a reasonable estimate for ω for a droplet with randomly positioned carbon inclusions. The Maxwell-Garnett mixing rule is given in Equation 7.1, where f is the volume fraction of BC to that of water, m_{BC} is the complex index of refraction of BC, and m_w is that of water.

$$m = \sqrt{m_w^2 \frac{m_{BC}^2 + 2m_w^2 + 2f(m_{BC}^2 - m_w^2)}{m_{BC}^2 + 2m_w^2 - f(m_{BC}^2 - m_w^2)}} \tag{7.1}$$

Since indices of refraction are wavelength dependent, m is actually a function of λ. The wavelength-dependent values of m_w were taken from Hale and Querry [1973] and Ray [1972], while those of m_{BC} are from Twitty and Weinman [1971] and Shettle and Fenn [1979]. Once this is established it is possible to model the composite droplet using Mie theory as previously described.

It is at this point that the approach described herein varies from that of Chuang et al. [2002], who used some regime-based simplifications to describe the scattering and absorption behaviour and then parameterized it to a simpler calculation that could be performed much more quickly. The drawback to their approach is that it somewhat unphysical - for instance, it does not reproduce the exact results for pure water when $f = 0$. Also, it is very specific to the shortwave radiation bands

employed in their model, and not easily generalized. Finally, it replaces the entire calculation of ω in the radiation code, which makes it slightly more difficult to implement or remove.

In contrast, the method used here explicitely calculates all of the scattering and absorption behaviour based upon Mie theory, a more physical approach. The drawback here is that these calculations are very time-consuming when carried out for a wide range of radii, wavelengths, and values of f. To counteract this, the calculations were instead carried out for a range of representative values, and stored in a look-up table. Also, rather than creating a table of ω values, a perturbation term, ω^* was used, where

$$\omega^* = \omega_0 - \omega, \tag{7.2}$$

and ω_0 is the single-scattering albedo of an equivalent sized water droplet without the BC inclusion.

It was then necessary to determine the representative range of values to be used as the basis for the look-up table. The wavelength range was determined by the four shortwave bands used in the CCCma AGCM, namely 0.2-0.69 μm, 0.69-1.19 μm, 1.19-2.38 μm, and 2.38-4.00 μm.

In order to produce a value representative of the range of each wavelength band, the calculations were carried out at a higher resolution of 25 wavelengths, and the results were fit to the four bands. The higher resolution calculations were averaged, weighting them according to the irradiance (in W m^{-2}) of the solar spectrum between each wavelengths following to Equation 7.3:

$$weight_{AB} = \frac{\sum_{i=A}^{B}(\lambda_{i+1} - \lambda_{i-1}) \times E(i)}{\sum_{j=1}^{j_{max}}(\lambda_{j+1} - \lambda_{j-1}) \times E(j)} \tag{7.3}$$

where $weight_{AB}$ is the weight assigned to the wavelength band going from λ_A to λ_B, the lower and upper values of the wavelength bands used, λ_x is the higher resolution wavelength of the solar spectrum data, and $E(x)$ is the solar irradiance at λ_x (in W m^{-2} μm^{-1}). The sum over i, in the numerator, determines the irradiance over the coarser resolution wavelength band used for the calculations, and it is normalized by the sum over j, in the denominator, over the entire shortwave spectrum considered here (from 0.20 to 4.00 μm).

The coarse-resolution wavelength bands were determined by the resolution at which the values of $m_{BC}(\lambda)$ and $m_w(\lambda)$ were known, with 25 values falling between 0.20 and 4.00 μm. These values were converted to the four wavelength bands required for the model using a weighted average, based upon the weights calculated using Equation 7.3.

The choice of the range for cloud droplet effective radius, r_{eff}, was determined by the range employed by the CCCma AGCM: 2.0-30.0 μm. Since the lower values occur more frequently, the spacing between successive r_{eff} values was chosen to be logarithmic, with 30 values in all. The Mie calculations were not carried out only for the single value of r_{eff}, but rather for many points along the cloud droplet distribution, the shape of which is given in Equation 7.4:

$$N(r) = A \times r^{\alpha} e^{-\beta r} \tag{7.4}$$

where A controls the amplitude of the distribution and $N(r)$ is the number density as a function of radius. α and β are functions of the effective radius, r_{eff}, and the variance, v, of the distribution and are given in Equations 7.5 and 7.6:

$$\alpha = \frac{1}{v} - 3 \tag{7.5}$$

$$\beta = \frac{\alpha + 3}{r_{eff}} \tag{7.6}$$

The value of v, the variance of the cloud droplet size distribution, is 0.171. The droplet size distribution and the value for v are those used in the CCCma AGCM, as described in Linder and Li [2000].

The Mie calculations were carried out for many radii along this distribution and then combined in a weighted average based upon the magnitude of the droplet size distribution at a given radius relative to the integral of the distribution. The cloud droplet size distribution was integrated following Simpson's rule [Adams, 1996, e.g.]. The total number of calculations required to attain the desired precision was quite large due to the resolution in r, Δr, and the maximum value of r, r_{max}. This is because of the highly fluctuating functions $Q_{scat}(r)$ and $Q_{abs}(r)$ which are needed to calculate $\omega(r)$, using Equation 2.20.

The required resolution was determined for a few test cases, and was defined as the point at which a doubling of r_{max} or a halving of Δr did not change the resultant σ_{scat} or σ_{ext} within 5 significant digits. In the end, the values chosen were Δr=0.001 μm and r_{max}=7.5$\times r_{eff}$. This meant that each calculation for the largest value of r_{eff}, 30.0 μm, calculations were carried out at 225 000 different radii.

In order to determine the appropriate values to choose for f, it was first necessary to look at how much BC might be found in the atmosphere in general. For this, the CCCma AGCM was employed, as is described in the following section.

7.3 The Black Carbon Fields in the Model

To estimate the range of values to represent the BC that might be found in clouds, the BC fields in the CCCma GCM were used. The emissions used are those of Liousse et al. [1996] and Penner et al. [1993], with emissions of 13.1 Tg C/yr, a burden of 0.23 Tg C, and a lifetime of 6.5 days.

The model used for this portion of the study is the fourth generation CCCma AGCM. The horizontal structure of temperature, specific humidity, pressure, vorticity, divergence, chemical tracers and the mass mixing ratios of liquid and ice water are represented with the spectral transform method with triangular truncation at wave number 47. There are 35 vertical levels, defined as a hybrid pressure-sigma grid, and the model equations are solved for each of them. Non-spectral quantities describing nonlinear processes and physical terms are calculated with 3.75°$\times$3.75°horizontal resolution. The time step between successive calculations is 20 minutes. A more complete description of the model is given in von Salzen et al. [2005].

The model contains an interactive sulfur cycle (Lohmann et al. [1999], von Salzen et al. [2000]), which can influence the radiative balance through the direct effect and the first and second indirect effects. The model's BC aerosols do not take part in these effects at present, nor are they implemented in the direct effect. The BC fields are represented by two prognostic variables, the soluble and insoluble BC mass mixing ratios. A more complete description of the BC fields can be found in Croft et al. [2005].

To estimate how much of the BC might be activated it was necessary to determine what fraction of it was hydrophilic. For this, the combined condensation-coagulation-oxidation scheme described in Croft et al. [2005] was used. This scheme determines the rate of conversion from insoluble BC to soluble or mixed state BC. Once the carbon is in this latter, hydrophilic state, it can be expected to act as CCN.

Once the carbon fields and ageing process are implemented in the GCM it is possible to determine the mass of this hydrophilic BC, BC_y, in each grid box. The volume fraction of BC estimated to be found within the cloud droplets, f, is determined as:

$$f = \frac{M_{BC_y} \rho_w b}{M_w \rho_{BC}}, \tag{7.7}$$

where M_{BC_y} and M_w are the masses of BC_y and liquid water respectively found within the grid box, ρ_{BC} and ρ_w are the densities of these constituents, and b is the fractional cloud cover found within the grid box. This assumes that the BC_y is evenly distributed throughout the grid box, with equal concentration in both cloudy and clear regions, while the liquid water is, for all practical purposes, entirely localized within the cloud boundaries. This also assumes that all BC_y found within the cloudy region has been activated, which may be an overestimation. Still, it would be expected that the larger BC_y particles, which dominate the mass, would be more likely to be activated. As such, the overestimation is not likely to be great.

Once this volume fraction, f, was determined, it was possible to set a basic range of typical values found within water clouds. Though the value over much of the earth is very low, on the order of 10^{-9}-10^{-8}, it was found to occasionally reach numbers on the order of 10^{-1}. An example of the BC fields, a monthly average at 900 mb for the month of June, is shown in Figure 7.2. The background values for most of the northern hemisphere is seen to be $\sim 10^{-9}$, with volume fractions of 10^{-6} over much of Europe and Asia. The values in the southern hemispere are consistently lower. Peak values are seen as high as 10^{-2}. The concentrations are seen to be higher over most of Europe and Asia, as would be expected, and there are some high values consistent with BC from ship exhaust emission inventories,

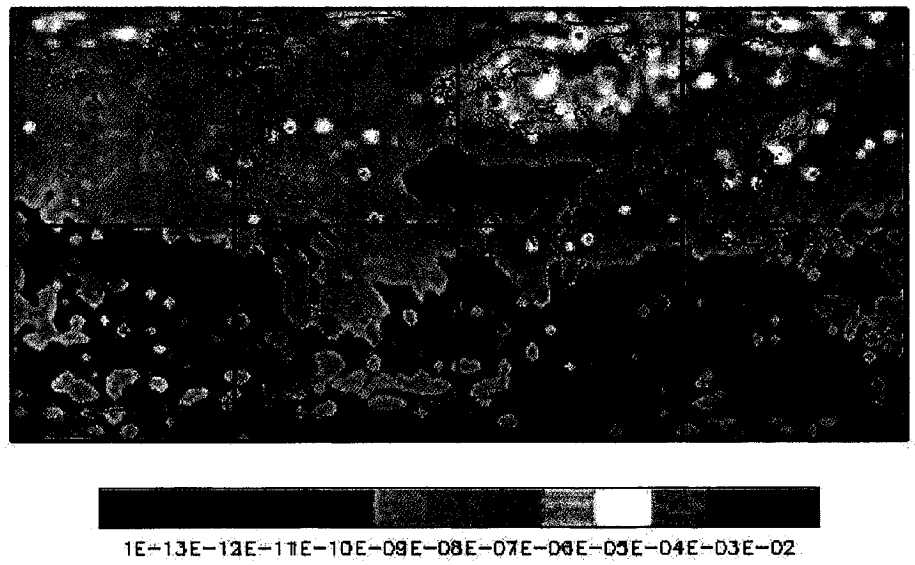

Figure 7.2: An example of a plot of the volume fraction of BC_y to water calculated according to Equation 7.7. This figure is a monthly mean for June, at a pressure of 900 mb.

such as in the middle of the Atlantic Ocean. The monthly values were used to determine the range of values for the look-up table as they provide a higher spread of data, both high and low, than do annual means.

As this volume fraction spans quite a large range of values, a logarithmic series was chosen to represent it in the look-up table, with 36 values ranging from 10^{-8} to 10^{-1}. 10^{-8} was chosen as a minimum value as its calculated ω is essentially that of pure water, and very little effect is seen for smaller volume fractions.

7.4 The Look-Up Table

Thus, a look-up table was created, with ω^* values calculated for four wavelength bands, with 30 representative values of r_{eff} ranging logarithmically from 2.0-30.0 μm, and with 36 f values ranging logarithmically from 10^{-8} to 10^{-1}. The single-scattering coalbedo as defined in Equation 2.21, $\overline{\omega}$, is shown in Figure 7.3, with one panel for each of the four wavelength bands. $\overline{\omega}$ is plotted rather than ω, as most of

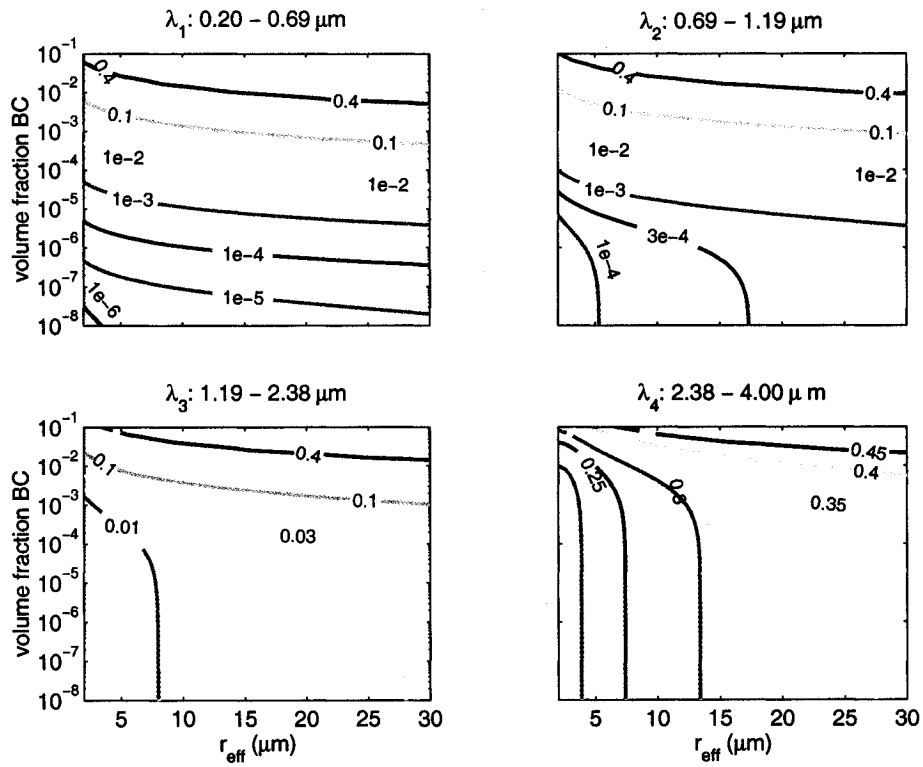

Figure 7.3: Plots of the $\overline{\omega}$ values, with one panel for each of the four wavelength bands, as labelled. $\overline{\omega}$ is calculated for the combined water and BC droplet.

the values are close to one.

In order to create the desired look-up table of ω^* values, as defined in Equation 7.2, one must determine the difference between $\overline{\omega}^*$ and the single-scattering coalbedo of pure water, $\overline{\omega_0}$. This can be seen through the combination of Equations 2.21 and 7.2:

$$\omega^* = \omega_0 - \omega = (1 - \overline{\omega_0}) - (1 - \overline{\omega}) = \overline{\omega} - \overline{\omega_0} \tag{7.8}$$

The $\overline{\omega_0}$ values are shown in Figure 7.4. With the exception of λ_4, the value of ω_0 is very close to unity. The comparison of Figures 7.3 and 7.4 show that except for at very high values of f ($> 10^{-4}$), the absorption by the water dominates the absorption for wavelength band λ_4.

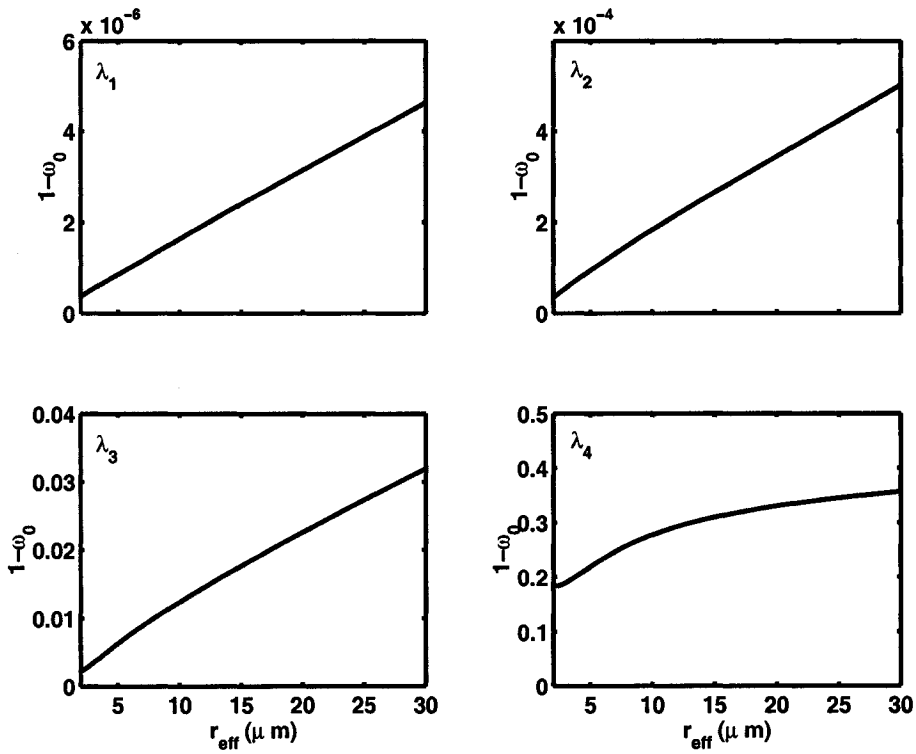

Figure 7.4: The single-scattering coalbedo of a distribution of pure water droplets ($\overline{\omega_0}$). The coalbedo is plotted rather than the albedo for ease of display since, with the exception of λ_4, the value of ω_0 is very near to unity.

Chapter 8

Application of the Look-Up Table

8.1 1-D Radiation Modelling

Now that the look-up table has been established, it can be implemented into climate models to determine the effect of the activated black carbon on radiative balance. In order to better understand this effect and to perform sensitivity tests in a simpler, more controlled model, it is first implemented in a 1-D radiation model based upon the radiative code used in the CCCma AGCM. The radiation code uses the parameterization of Dobbie et al. [1999], which calculates the radiative properties for water clouds over the shortwave portion of the solar spectrum.

The 1-D radiative model is very simple, and essentially calculates radiative quantities for one time step for a single point, based upon a prescribed temperature and relative humidity profile, and prescribed clouds. There is no evolution of the cloud based upon its radiative properties, and the cloud is not physically generated, but has a prescribed effective radius, liquid water content, and thickness. Though not necessarily physical, this does allow one to easily test the sensitivity of the effect to changes in these characteristics.

The model was tested for both low and mid-level clouds for temperature profiles representing mid-latitude summer and the tropics, as these are cases where water clouds might be expected. The physical characteristics of the assumed two cloud types, low and mid-level, are given in Table 8.1. (The fractional values of cloud base and cloud thickness correspond to integer numbers of pressure levels as defined by the mid-latitude summer atmospheric profile.)

With the clouds prescribed in Table 8.1 and a range of values for f, the 1-D radiation model was run. Two dimensional linear interpolation was employed to determine the value of ω^* based upon the values of r_{eff} and f. The results for the low-level clouds are shown in Figure 8.1, and the results for the mid-level clouds

Table 8.1: Physical characteristics of the low and mid-level clouds used for the 1-D radiation model.

	low-level cloud	mid-level cloud
$r_{eff}(\mu m)$	5.89	6.20
liquid water content (g m^{-3})	0.22	0.28
cloud base (m)	278.6	355.2
cloud thickness (m)	33.7	56.6
cloud fraction	1.0	0.5

are shown in Figure 8.2. The variables plotted are the downward flux absorbed by the ground and the downward flux at the surface broken down into diffuse, visible and near infra-red radiation, all in units of W m^{-2}.

These plots indicate that the effect of the black carbon addition is quite dramatic, with the region of steepest change seen for BC volume fractions between approximately 10^{-5} and 10^{-4}. The effects are stronger for the low cloud, but that is mostly due to the difference in cloud fraction, at 1.0 for low clouds and 0.5 for mid-level clouds. The effect of temperature, as seen in the difference between the tropical and mid-latitude case, is rather minor. The effects at high volume fractions are very strong, and would not be sustainable physically; analysis of the solar heating rate profiles indicate a maximum solar heating rate for the low cloud case of over 400 K/day for the low cloud case with $f > 10^{-2}$, and a maximum solar heating rate for the mid-level cloud of over 200 K/day for the same volume fraction of BC. This would not be a sustainable heating rate in a real cloud, and would lead to the dissipation of the cloud. This cannot be explored with the 1-D radiation model used here, but some insight may be found with the implementation of the effect into the AGCM. Still, the 1-D model allows for sensitivity testing for the cloud characterisitics found in Table 8.1.

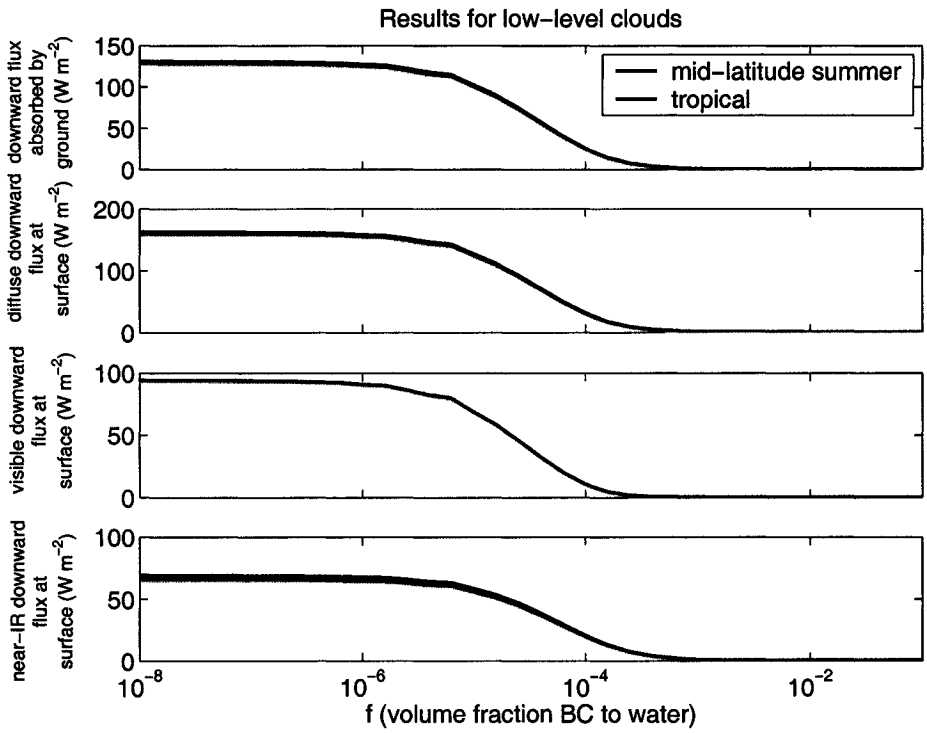

Figure 8.1: Some calculated radiative results from the 1-D model for low clouds with the characteristics given in Table 8.1 for a variety of values of f. The blue line is for a temperature profile representative of mid-latitude summer and the green line is for the tropics, though the two are often indistinguishable.

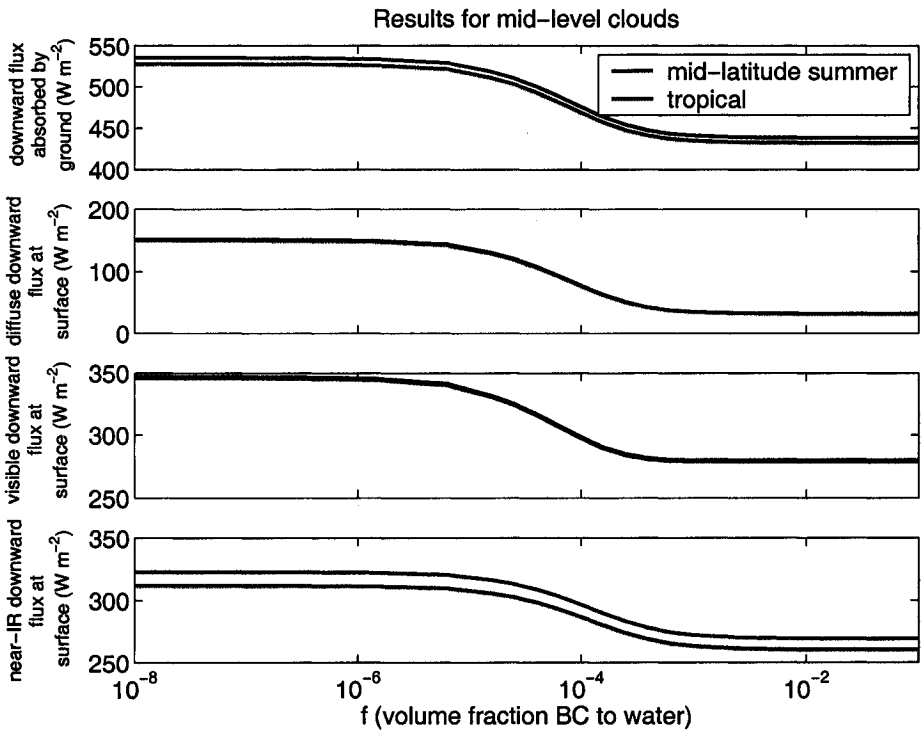

Figure 8.2: The same quantities as in Figure 8.1 but for the mid-level cloud prescribed by the quantities in Table 8.1.

8.2 Sensitivity Testing

In order to examine the effect of the effective radius, solar zenith angle, liquid water content, and cloud thickness on the effect of the black carbon inclusions, they were each varied in turn and the radiative properties were again computed.

The first quantity to be examined is the effective radius of the cloud droplet spectrum. Figure 8.3 shows the same quantities given in Figure 8.1, but plotted for a range of values of r_{eff}. All other cloud characteristics are taken from Table 8.1, and the temperature profile used is that of mid-latitude summer. The effect is similar for mid-level clouds and the tropical atmospheric profile. It can be seen that for low levels of BC in the cloud less radiation reaches the surface for smaller effective radii. This difference is due to the first indirect aerosol effect, as the albedo of the cloud is higher for a smaller effective radius. As the volume fraction of black carbon increases however, the difference due to the effective radius is lessened, and the absorption dominates.

Next, the effect of the solar zenith angle is examined in Figure 8.4. As in the case of varying effective radius, the lowest values of f show the effects of the solar zenith angle most clearly, with the most radiation reaching the ground for the smallest solar zenith angle. As the amount of BC in the cloud increases, the absorption effect dominates the behaviour.

The next variable to be tested is the liquid water content (LWC) of the cloud, which was varied from 0.10 to 0.85 g m^{-3}. The radiative quantities for representative cases ranging from 0.10 to 0.55 g m^{-3} are shown in Figure 8.5, again with the other physical characteristics taken from the low cloud described in Table 8.1. Here it is interesting to note that the effect is noticeable at smaller values of f for the higher LWC values, but that the change is most dramatic for the lowest value of LWC.

Finally, the effect of varying the thickness of the cloud was explored. This is shown in Figure 8.6, with cloud thicknesses (CTs) ranging from 25.9 to 325.9 m plotted. These numbers correspond to integer numbers of pressure levels based on the mid-latitude summer atmospheric profile, all with a cloud base at 278.6 m as in Table 8.1. Here, as in the case of the varying LWC of Figure 8.5, the thinnest

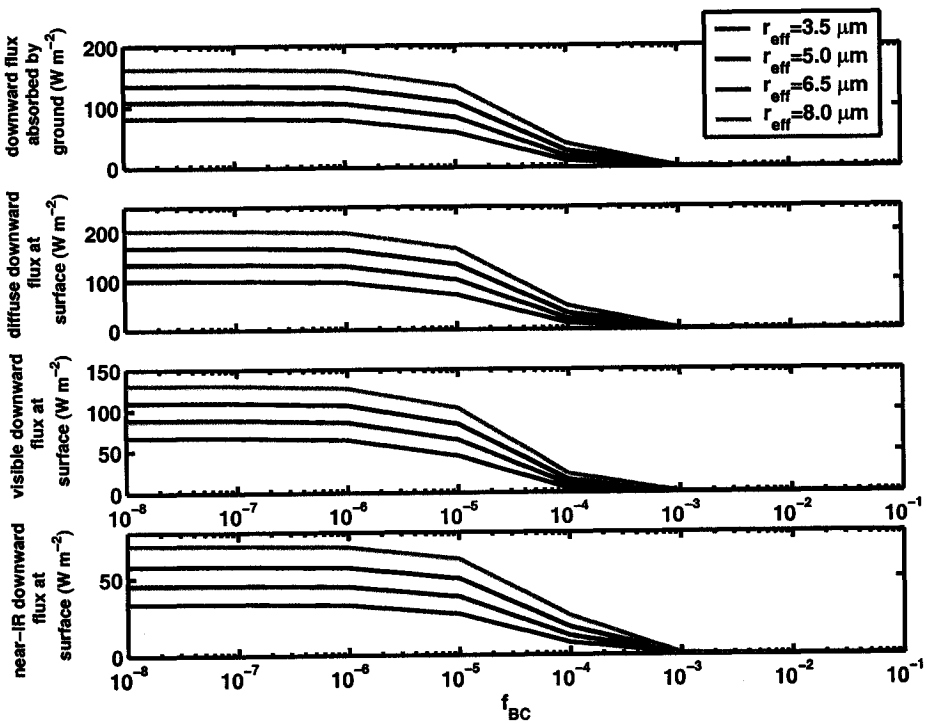

Figure 8.3: The same quantities are plotted as in Figure 8.1 but each is calculated for a range of effective radii, as indicated. The mid-latitude atmospheric profile is used, and all other cloud characteristics are taken from the low cloud column of Table 8.1.

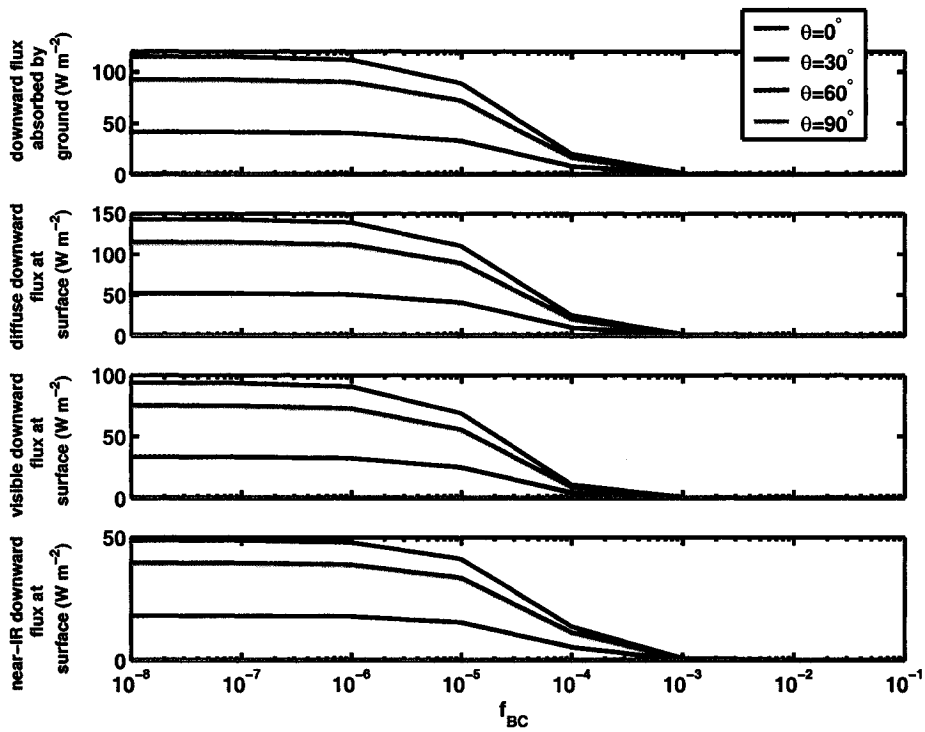

Figure 8.4: The same quantities are plotted as in Figure 8.3 but each is calculated for the solar zenith angles 0°, 30°, 60°and 90°.

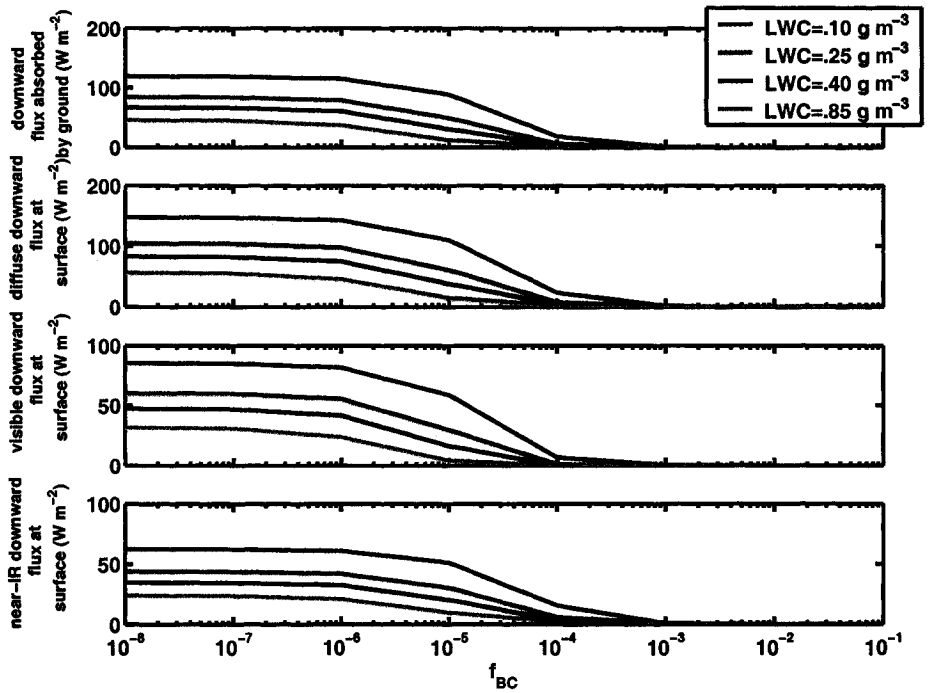

Figure 8.5: The same quantities are plotted as in Figure 8.3 but each is calculated for cloud liquid water contents (LWCs) of 0.10, 0.25, 0.40 and 0.55 g m^{-3}.

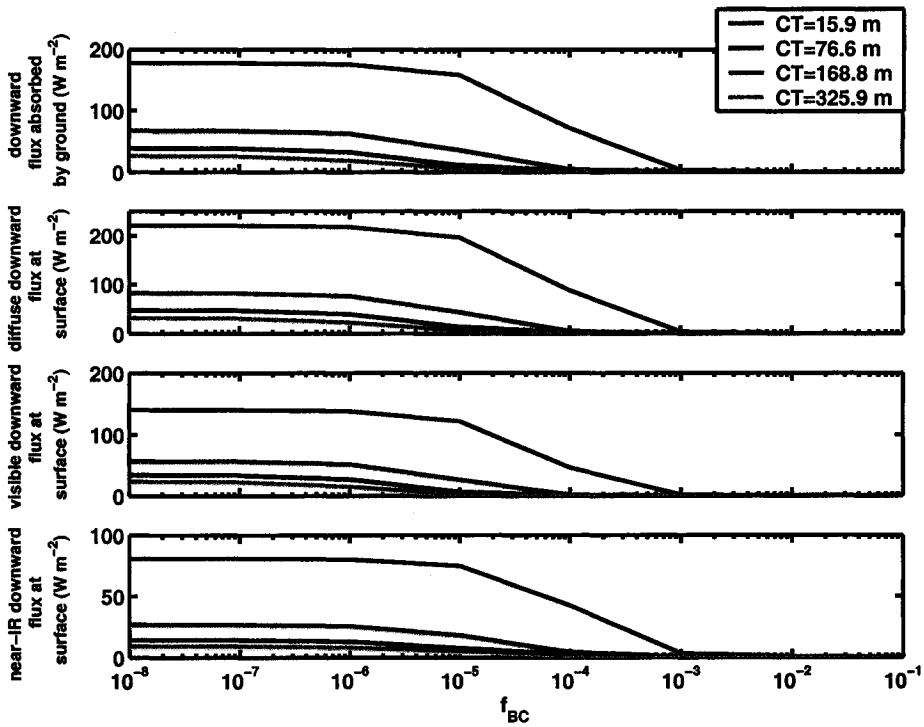

Figure 8.6: The same quantities are plotted as in Figure 8.3 but each is calculated for cloud thicknesses (CTs) of 15.9, 76.6, 168.8 and 325.9 m.

cloud (or the cloud with the lowest LWC) shows the most dramatic change with the addition of BC, though not much change is seen for f values lower than 10^{-5}.

8.3 The Effect of Non-Absorbing CCN in the Cloud

One of the assumptions made in the 1-D modelling to this point, and made in the parameterization of Chuang et al. [2002], is that the absorbing aerosols are distributed evenly throughout the cloud droplet size spectrum, with a constant volume fraction in each droplet. This may not be the case, as it is possible that only 10% or 50% of the cloud droplets have any absorbing aerosol in them at all, while the remainder of the cloud droplets would have non-absorbing aerosols as CCN, with a single-scattering albedo comparable to that of pure water. This means that there would be fewer droplets containing BC, but that these fewer droplets would have a higher volume fraction of BC than is predicted in Equation 7.7.

If the fraction of cloud droplets containing BC is given as F, then this new volume fraction, f^*, would be given as:

$$f^* = \frac{f}{F} \tag{8.1}$$

where f is calculated as in Equation 7.7. This requires a new calculation of ω and ω^*, of course. The value of ω is then given as:

$$\omega = \frac{(1-F)Q_{scat}(f=0) + FQ_{scat}(f^*)}{(1-F)Q_{ext}(f=0) + FQ_{ext}(f^*)} \tag{8.2}$$

calculated for a given value of r_{eff}, λ, F, and f. The assumption here is that cloud droplets containing the absorbing and non-absorbing aerosols have the same size distribution, and that the fractional number densities of each are equal to the fractional volumes. Q_{ext} and Q_{scat} are calculated using Mie theory, with the values weighted according to the solar spectrum and the cloud droplet spectrum as discussed in the previous chapter.

The results from this calculation are shown in Figure 8.7 for an effective radius of 10.75 μm. This figures indicates that the assumption that the activated BC is spread throughout all the droplets with a constant volume fraction gives the strongest effect, and that the fewer droplets are calculated as containing BC, the weaker the effect will be.

This is an interesting result, and reflects the fact that most of the absorption by the BC takes place within the outer $\sim$0.2 μm of the particle [Chýlek et al., 1996]. This means that for the same total volume of BC, a larger number of small BC particles will absorb more radiation than a smaller number of large BC particles. (This is not to say that the cloud droplet size is bigger or smaller, simply that the size of the absorbing particle within the cloud droplet is bigger or smaller.)

The question remains of what value to assume for F in the CCCma AGCM runs. Ideally this number could be provided by an AGCM, based upon realistic and interactive distributions of both absorbing and non-absorbing aerosols, which could be validated against data from field projects. At this point, the BC fields in the CCCma AGCM are not yet interactive with clouds, and some approximation would have to be made.

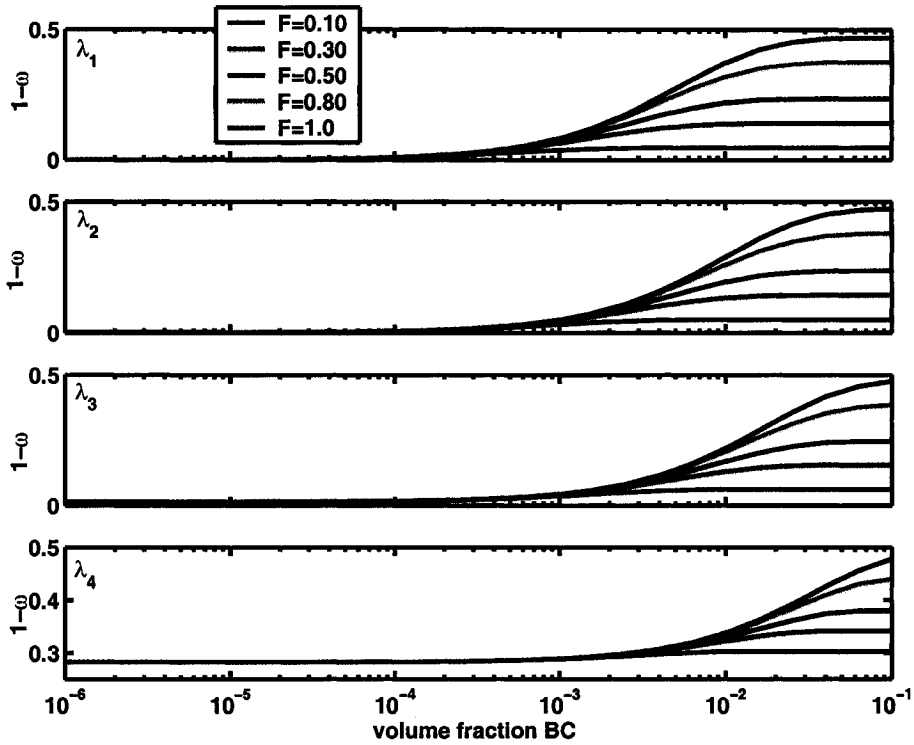

Figure 8.7: The calculated value of $\overline{\omega}$ is presented based upon different assumptions for the fraction of cloud droplets over which the BC is distributed, ranging from 0.1 to 1.0.

Since this value of F can have such a remarkable effect on the value of $\overline{\omega}$, as seen in Figure 8.7, its assigned value should be carefully considered. Setting F to one can at least offer an upper bound to this effect.

8.4 Future Work: Implementation in the CCCma AGCM

Now that the parameter space has been explored through the development of the look-up table and the implementation of this perturbation to the cloud albedo in a 1-D model, the next logical step is the use of the look-up table in the Atmospheric General Circulation Model (AGCM) of the Canadian Centre for Climate modelling and analysis (CCCma). This means that the clouds would no longer be unphysically prescribed, as in the 1-D radiation model, but would rather be a result of the atmospheric conditions in the model. This would also allow the activated BC to affect the characteristics of the cloud. For instance, the increased solar heating rates as a result of the absorption will change the temperature profile of the atmosphere, which will have an effect on the diagnostically-determined cloud.

Chapter 9

Conclusions

9.1 From the Research Cruise

The optical properties (σ_{sp}, σ_{bsp} and σ_{abs}) of the aerosols in a remote marine area were measured over a ten day period coincident with measurements of the aerosol particle size distribution and chemical composition. The particle size and chemical data were applied in a Mie scattering model in an effort to examine optical closure. The resulting calculated and measured extinction parameters did not compare well before considering the angular limitations of the nephelometer. Taking those limitations into account led to agreement to within 15% in most cases.

Scattering apportionment by size indicates that the vast majority of the scattering and backscattering during the SERIES cruise in the north Pacific was due to coarse particles, with the majority attributed to particles greater than 10 μm in diameter. The large correction factor needed to account for the angular limitations of the nephelometer (median of approximately 17) suggests that to estimate (untruncated) scattering and backscattering coefficientsfrom coarse particles the best approach currently available may be to calculate it from independent measurements of the size distribution and chemical composition of the aerosol. New techniques (e.g. cavity ring-down, Strawa et al. [2003]) may provide a direct solution to this problem.

9.2 From the Flight Campaign

A series of six research flights were carried out on board a Convair 580 belonging to the National Research Council's Institute for Aerospace Research. The flights took place from October 13 to 17, 2003, in and around stratocumulus off the coast

of Nova Scotia as part of a C-SOLAS project in the region. The aerosol size distribution, size-resolved chemical speciation, and total scattering and backscattering coefficients were measured. Again, an optical closure study was undertaken.

Closure was attained for more than 70% of the total scattering measurements, with the poorest results on Flight #1, which had very few large particles compared to the other flights. This flight had particlularly low near-surface wind speeds, which would reduce the formation of large sea salt aerosols via droplet to particle conversion. On the whole, agreement was not found between the calculated and measured backscattering coefficients. This may be due to particle non-sphericity due to crystallization while drying, though a low signal to noise ratio in the nephelometer may have also played a role.

Based upon the measurements taken inside the aircraft, roughly half the total scattering and most of the backscattering in the marine environment surrounding Nova Scotia is due to the contribution from supermicron particles to an altitude of approximately 1000 m. This was true for four of the five flights, with the exception of Flight #1. Above 1000 m the scattering and backscattering coefficients are significantly lower and are primarily due to scattering by submicron particles. However there are few measurements above 1000 m, and it is difficult to say if this is always the case, particularly on days with different synoptic conditions.

Most of the aerosol particles larger than $\sim$2 μm were not sampled by any of the instruments on board the aircraft due to sampling loss at the inlet. In order to assess the effect that this might have, the results calculated using an instrument outside the aircraft, the FSSP, for the particles larger than 0.275 μm. These results suggest a stronger dominance of the scattering coefficient from supermicron aerosols, and led to in an increase in the calculated total and backscattering coefficients for the measurements taken below cloud base. The increase in calculated below cloud total scattering ranges from 14 to 183% for green light, with a corresponding increase in backscattering from 2 to 37%. The difference as a result of the size distribution measured outside of the aircraft was not as clear at higher altitudes as in general there are fewer large particles there.

9.3 From the Modelling of Activated Black Carbon

A look-up table was developed to represent the change in the shortwave single-scattering coalbedo of water clouds due to the presence of activated BC aerosols within the cloud droplets. The table has three dimensions: the effective radius of the cloud droplet spectrum, the fraction of the volume of hydrophilic BC to the volume of liquid water within the cloud, and the wavelength band. The effective radius ranges from 2.0-30.0 μm, based upon the range of values used in the CCCma AGCM. The four shortwave bands also match those used in the AGCM. The volume fraction of BC in the table ranges from 10^{-8} to 10^{-1}, based upon the values seen in the CCCma AGCM, using Equation 7.7 and the BC fields of Penner et al. [1993] and Liousse et al. [1996], with an ageing scheme based on Croft et al. [2005]. The Maxwell-Garnett mixing rule was employed to determine the index of refraction of the combined water-BC droplet, and the values of ω were calculated using Mie theory.

Once this table was established, it was implemented into a one dimensional radiation model based upon the parameterization of Dobbie et al. [1999]. The effect on the volume fraction of black carbon on the transmitted radiation of both low and mid-level clouds was investigated, and the sensitivity to the prescribed solar zenith angle, cloud thickness, cloud droplet effective radius, and liquid water content were explored. Finally, the sensitivity to the percentage of cloud droplets assumed to contain BC was tested. It was found that the fewer droplets the volume of BC was distributed over, the weaker the overall effect on the computed value of ω.

9.4 Outlook

The field experiments discussed in this thesis illustrated some of the problems with experimental data, through instrument non-idealities and inlet losses, both of which lead to significant underestimations of the measured scattering coefficient. In order have more reliable measurements for the optical properties of ambient aerosols these problems should be addressed. To correct for some of the problems

with the nephelometer new instruments are being developed, such as the use of continuous wave cavity ring-down (CW-CRD, Strawa et al. [2003]), which is able to simultaneously measure the absorption and extinction coefficients of a sample without angular truncation effects.

In future, the look-up table is set to be implemented into the CCCma AGCM in order to test the global and regional impact activated BC might have on the earth's radiation budget, as well as potential cloud feedbacks associated with it. In addition to this, the direct and semi-direct effect of BC will be included in the AGCM in order to better understand the complex effect of these absorbing aerosols.

Bibliography

A. S. Ackerman, O. B. Toon, D. E. Stevens, A. J. Heymsfield, V. Ramanathan, and E. J. Welton. Reduction of tropical cloudiness by soot. *Science*, 288:1042–1047, 2000.

R. A. Adams. *Calculus of Several Variables*. Addison-Wesley, 3rd edition, 1996.

B. Albrecht. Aerosols, cloud microphysics, and fractional cloudiness. *Science*, 245: 1227–1230, 1989.

T. L. Anderson, D. S. Covert, S. F. Marshall, M. L. Laucks, R. J. Charlson, A. P. Waggoner, J. A. Ogren, R. Caldow, R. L. Holm, F. R. Quant, A. Wiedensohler, N. A. Ahlquist, and T. S. Bates. Performance characteristics of a high-sensitivity, three-wavelength total scatter/backscatter nephelometer. *J. Atmos. Oceanic Technol.*, 13:967–986, 1996.

T. L. Anderson and J. A. Ogren. Determining aerosol radiative properties using the TSI 3563 integrating nephelometer. *Aerosol Sci. Technol.*, 29:57–69, 1998.

A. J. Armendariz and D. Leith. Concentration measurement and counting efficiency for the aerodynamic particle sizer 3320. *J. Aerosol Sci.*, 33:133–148, 2002.

B. W. Blomquist, B. J. Huebert, S. G. Howell, M. R. Litchy, C. H. Twohy, A. Schanot, D. Baumgardner, B. Lafleur, R. Seebauch, and M. L. Laucks. An evaluation of the community aerosol inlet for the NCAR C-130 research aircraft. *J. Atmos. Oceanic Technol.*, 18:1387–1397, 2001.

C. F. Bohren and D. R. Huffman. *Absorption and Scattering of Light by Small Particles*. Wiley, 1998.

T. C. Bond, T. L. Anderson, and D. Campbell. Calibration and intercomparison of filter-based measurements of visible light absorption by aerosols. *Aerosol Sci. Technol.*, 30:582–600, 1999.

C. M. Carrico, M. J. Rood, and J. A. Ogren. Aerosol light scattering properties at Cape Grim, Tasmania, during the First Aerosol Characterization Experiment. *J. Geophys. Res.*, 103:16 565–16 574, 1998.

C. C. Chuang, J. E. Penner, J. M. Prospero, K. E. Grant, G. H. Rau, and K. Kawamoto. Cloud susceptibility and the first aerosol indirect forcing: Sensitivity to black carbon and aerosol concentrations. *J. Geophys. Res.*, 108: doi:10.1029/2000JD000215, 2002.

P. Chýlek, G. B. Lesins, G. Videen, J. G. D. Wong, R. G. Pinnick, D. Ngo, and J. D. Klett. Black carbon and absorption of solar radiation by clouds. *J. Geophys. Res.*, 101:23 365–23 371, 1996.

P. Chýlek and G. Videen. Scattering by a composite sphere and effective medium approximations. *Opt. Comm.*, 146:15–20, 1998.

A. D. Clarke, Y. Shinozuka, V. N. Kapustin, S. Howell, B. Huebert, S. Doherty, T. Anderson, D. Covert, J. Anderson, X. Hua, K. G. Moore II, C. McNaughton, G. Carmichael, and R. Weber. Size distributions and mixtures of dust and black carbon aerosol in Asian outflow: Physiochemistry and optical properties. *J. Geophys. Res.*, 109:doi:10.1029/2003JD004378, 2004.

J. Cook and E. J. Highwood. Climate response to tropospheric absorbing aerosols in an intermediate general-circulation model. *Q. J. R. Meteorol. Soc.*, 130:175–191, 2004.

B. Croft, U. Lohmann, and K. von Salzen. Black carbon ageing in the Canadian Centre for Climate modelling and analysis atmospheric general circulation model. *Atmos. Chem. Phys.*, 5:1931–1949, 2005.

G. A. d'Almeida, P. Koepke, and E. P. Shettle. *Atmospheric Aerosols: Global Climatology and Radiative Characteristics*. A. Deepak, 1991.

J. S. Dobbie, J. Li, and P. Chýlek. Two- and four- stream optical properties for water clouds and solar wavelengths. *J. Geophys. Res.*, 104:2067–2079, 1999.

C. Erlick, L. M. Russell, and V. Ramaswamy. A microphysics-based investigation of the radiative effects of aerosol-cloud interaction for two MAST Experiment case studies. *J. Geophys. Res.*, 106:1249–1269, 2001.

A. M. Fridlind and M. Z. Jacobson. Point and column aerosol radiative closure during ACE 1: Effects of particle shape and size. *J. Geophys. Res.*, 108: doi:10.1029/2001JD001553, 2003.

S. L. Gong, L. A. Barrie, and J. P. Blanchet. Modeling sea-salt aerosols in the atmosphere, 1. Model development. *J. Geophys. Res.*, 102:3805–3818, 1997.

G. M. Hale and M. R. Querry. Optical constants of water in the 200 nm to 200 μm wavelength region. *Appl. Opt.*, 12:555–563, 1973.

J. E. Hansen, M. Sato, and R. Ruedy. Radiative forcing and climate response. *J. Geophys. Res.*, 102:6831–6864, 1997.

J. M. Haywood, V. Ramaswamy, and B. J. Soden. Tropospheric aerosol climate forcing in clear-sky satellite observations over the oceans. *Science*, 283:1299–1303, 1999.

J. Heintzenberg, R. J. Charlson, A. D. Clarke, C. Liousse, V. Ravaswamy, K. P. Shine, M. Wendisch, and G. Helas. Measurements and modelling of aerosol single-scattering albedo: Progress, problems and prospects. *Beitr. Phys. Atmos.*, 70:249–263, 1997.

M. Hess, P. Koepke, and I. Schult. Optical properties of aerosols and clouds: The software package OPAC. *Bull. Amer. Meteor. Soc.*, 79:831–834, 1998.

R. Jaenicke and T. Hanusch. Simulation of the optical particle counter Forward Scattering Spectrometer Probe-100 (FSSP-100) - consequences for size distribution measurements. *Aerosol Sci. and Tech.*, 18:309–322, 1993.

J. T. Jayne, D. C. Leard, X. Zhang, P. Davidovits, K. A. Smith, C. E. Kolb, and D. R. Worsnop. Development of an aerosol mass spectrometer for size and composition analysis of submicron particles. *Aerosol Sci. and Tech.*, 33:49–70, 2000.

B. T. Johnson. The semi-direct aerosol effect: Comparisons of a single-column model with large eddy simulation for marine stratocumulus. *J. Clim.*, 18:119–130, 2005.

B. T. Johnson, K. P. Shine, and P. M. Forster. The semi-direct aerosol effect: Impact of absorbing aerosols on marine stratocumulus. *Q. J. R. Meteorol. Soc.*, 130:1407–1422, 2004.

P. Koepke, M. Hess, I. Schult, and E. P. Shettle. Global Aerosol Data Set. *MPI Meteorologie Hamburg*, 243:44, 1997.

W. R. Leaitch, N. C. Shantz, M. Mozurkewich, K. L. Hayden, J. W. Strapp, D. Toom-Sauntry, M. Wasey, U. Lohmann, P. Lehr, J. Marshall, T. Garrett, D. Waugh, J. Jayne, D. Worsnop, and M. Wolde. Evidence for an indirect effect of the organic aerosol. *J. Geophys. Res.*, submitted, 2005.

P. J. Lehr. The role of aerosols in drizzle formation in marine stratocumulus. *Dalhousie University, M.Sc. thesis*, 2005.

S. Li, K. B. Strawbridge, W. R. Leatich, and A. M. Macdonald. Aerosol backscattering determined from chemical and physical properties and lidar observations over the east coast of Canada. *Geophys. Res. Lett.*, 25:1653–1656, 1998.

T. H. Linder and J. Li. Parameterization of the optical properties of water clouds in the infrared. *J. of Climate*, 13:1797–1805, 2000.

C. Liousse, J. E. Penner, C. Chuang, J. J. Walton, and H. Eddleman. A global three-dimensional model study of carbonaceous aerosols. *J. Geophys. Res.*, 101:19 411–19 432, 1996.

P. S. K. Liu, W. R. Leaitch, J. W. Strapp, and M. A. Wasey. Response of Particle Measuring Systems airborne ASASP and PCASP to NaCl and latex particles. *Aerosol Sci. and Tech.*, 16:83–95, 1992.

U. Lohmann and J. Feichter. Can the direct and semi-direct aerosol effect compete with the indirect effect on a global scale? *Geophys. Res. Lett.*, 28:159–161, 2001.

U. Lohmann, J. Feichter, C. C. Chuang, and J. E. Penner. Prediction of the number of cloud droplets in the ECHAM GCM. *J. Geophys. Res.*, 104:9169–9198, 1999.

W. T. Luke. Evaluation of a commercial pulsed fluorescence detector for the measurement of low-level SO_2 concentrations during the Gas-Phase Sulfur Intercomparison Experiment. *J. Geophys. Res.*, 102:16 255–16 265, 1997.

V. A. Marple, K. L. Rubow, and S. M. Behm. A Micro-Orifice Uniform Deposit Impactor (MOUDI) - description, calibration, and use. *Aerosol Sci. and Tech.*, 14: 434–446, 1991.

J. Marshall, U. Lohmann, W. R. Leaitch, N. Shantz, L. Phinney, D. Toom-Sauntry, and S. Sharma. Optical properties of aerosol particles over the northeast Pacific. *J. App. Meteor.*, 44:1206–1220, 2005.

A. Maßling, A. Wiedensohler, B. Busch, C. Neusüß, P. Quinn, T. Bates, and D. Covert. Hygroscopic properties of different aerosol types over the Atlantic and Indian Oceans. *Atmos. Chem. Phys.*, 3:1377–1397, 2003.

M. I. Mishchenko, L. D. Travis, R. A. Kahn, and R. A. West. Modelling phse functions for dustlike tropospheric aerosols using a shape mixture of randomly oriented polydisperse spheroids. *J. Geophys. Res.*, 102:16831–16847, 1997.

D. M. Murphy, J. R. Anderson, P. K. Quinn, L. M. McInnes, F. J. Brechtel, S. M. Kreidenweis, A. M. Middlebrook, M. Posfai, D. S. Thomson, and P. R. Buseck. Influence of sea-salt on aerosol radiative properties in the Southern Ocean marine boundary layer. *Nature*, 392:62–65, 1998.

C. D. O'Dowd, J. A. Lowe, and M. H. Smith. The relative importance of non-sea-salt sulphate and sea-salt aerosol to the marine cloud condensation nuclei population: An imroved multi-component aerosol-cloud droplet parameterization. *Quart. J. Roy. Meteor. Soc.*, 125:1311–1314, 1999.

J. E. Penner, H. Eddleman, and T. Novakov. Towards the development of a global inventory for black carbon emissions. *Atmos. Environ.*, 27A:1277–1295, 1993.

J. E. Penner, S. Y. Zhang, and C. C. Chuang. Soot and smoke aerosol may not warm the climate. *J. Geophys. Res.*, 108:doi:10.1029/2003JD003409, 2003.

L. Phinney, W. R. Leaitch, U. Lohmann, H. Boudries, D. R. Worsnop, J. T. Jayne, D. Toom-Sauntry, M. Wadleigh, S. Sharma, and N. Shantz. Characterization of aerosol over the sub-arctic NE Pacific during SERIES. *Deep-Sea Res. II*, submitted, 2005.

P. Pilewskie and F. Valero. Direct observation of excess solar absorption by clouds. *Science*, 267:1626–1629, 1995.

C. Pilinis and X. Li. Particle shape and internal homogeneity effects on the optical properties of tropospheric aerosols of relevance to climate forcing. *J. Geophys. Res.*, 103:3789–3800, 1998.

J. B. Pollack and J. N. Cuzzi. Scattering by nonspherical particles of size comparable to a wavelength: a new semi-empirical theory and tis application to tropospheric aerosols. *J. Atmos. Sci.*, 37:868–881, 1980.

P. K. Quinn, T. L. Anderson, T. S. Bates, R. Dlugi, J. Heintzenberg, W. von Hoyningen-Huene, M. Kulmala, P. B. Russell, and E. Swietlicki. Closure in tropospheric aerosol-climate research: A review and future needs for addressing aerosol direct shortwave radiative forcing. *Beitr. Phys. Atmos.*, 69:547–577, 1996.

P. K. Quinn and D. J. Coffman. Local closure during the First Aerosol Characterization Experiment (ACE 1): Aerosol mass concentration and scattering and backscattering coefficients. *J. Geophys. Res.*, 103:16575–16596, 1998.

P. K. Quinn, S. F. Marshall, T. S. Bates, D. S. Covert, and V.N. Kapustin. Comparison of measured and calculated aerosol properties relevant to the direct radiative forcin of tropospheric sulfate aerosol on climate. *J. Geophys. Res.*, 100:8977–8991, 1995.

C. A. Randles, L. M. Russell, and V. Ramaswamy. Hygroscopic and optical properties of organic sea salt aerosol and consequences for climate forcing. *Geophys. Res. Let.*, 31:doi:10.1029/2004GL020628, 2004.

P. S. Ray. Broadband complex refractive indices of ice and water. *Appl. Opt.*, 11: 1836–1844, 1972.

J. H. Seinfeld and S. N. Pandis. *Atmospheric Chemistry and Physics*. Wiley, 1998.

E. P. Shettle and R. W. Fenn. Models for the aerosols of the lower atmosphere and the effects of humidity variations on their optical properties. *AFGL-TR-79-0214*, page ADA085951, 1979.

Y. Shinozuka, A. D. Clarke, S. G. Howell, V. N. Kapustin, and B. J. Huebert. Seasalt vertical profiles over the Southern and tropical Pacific oceans: Microphysics, optical properties, spatial variability, and variations with wind speed. *J. Geophys. Res.*, 109:doi:10.1029/2004JD004975, 2004.

C. Sioutas, E. Abt, J. M. Wolfson, and P. Koutrakis. Evaluation of the measurement performance of the scanning mobility particle sizer and aerodynamic particle sizer. *Aerosol Sci. and Tech.*, 30:84–92, 1999.

A. Smirnov, Y. Villevalde, N. T. O'Neill, A. Royer, and A. Tarussov. Aerosol optical depth over the oceans: Analysis in terms of synoptic air mass types. *J. Geophys. Res.*, 100:16 639–16 650, 1995.

S. R. Smith, M. A. Bourassa, and R. J. Sharp. Establishing more truth in true winds. *J. Atmos. Oceanic Technol.*, 16:929–952, 1999.

G. L. Stephens and S. C. Tsay. On the cloud absorption anomaly. *Q. J. R. Meteorol. Soc.*, 116:671–704, 1990.

A. W. Strawa, R. Castaneda, T. Owano, D. S. Baer, and B. A. Paldus. The measurement of aerosol optical properties using continuous wave cavity ring-down techniques. *J. Atmos. Oceanic Technol.*, 20:454–465, 2003.

I. N. Tang. Chemical and size effects of hygroscopic aerosols on light scattering coefficients. *J. Geophys. Res.*, 101:19245–19250, 1996.

I. N. Tang. Thermodynamic and optical properties of mixed-salt aerosols of atmospheric importance. *J. Geophys. Res.*, 102:1883–1893, 1997.

O. B. Toon, J. B. Pollack, and B. N. Khare. The optical constants of several atmospheric aerosol species: Ammonium sulfate, aluminum oxide, and sodium chloride. *J. Geophys. Res.*, 81:5733–5745, 1976.

J. T. Twitty and J. A. Weinman. Radiative properties of carbonaceous aerosols. *J. Appl. Meteor.*, 10:725–731, 1971.

S. A. Twomey. The influence of pollution on the shortwave albedo of clouds. *J. Atmos. Sci.*, 34:1149–1152, 1977.

K. von Salzen, H. G. Leighton, P. a. Ariya, L. A. Barrie, S. L. Gong, J.-P. Blanchet, L. Spacek, U. Lohmann, and L. I. Kleinman. Sensitivity of sulfate aerosol size distributions and CCN concentrations over North America to SO_x emmisions and H_2O_2 concentrations. *J. Geophys. Res.*, 105:9741–9765, 2000.

K. von Salzen, N. A. McFarlane, and M. Lazare. The role of shallow convection in the water and energy cycles of the atmosphere. *Climate Dynamics,*, submitted, 2005.

J. Wang and B. Geerts. Identifying drizzle within marine stratus with w-band radar reflectivity. *Atmos. Res.*, 69:1–27, 2003.

G. N. Watson. *A Treatise on the Theory of Bessel Functions*. Cambridge University Press, 1944.

R. C. Weast, M. J. Astle, and W. H. Beyer, editors. *CRC Handbook of Chemistry and Physics*. CRC Press, 53rd edition, 1972.

R. J. Weber, A. D. Clarke, M. Litchy, J. Li, G. Kok, R. D. Schillawski, and P. H. McMurry. Spurious aerosol measurements when sampling from aircraft in the vicinity of clouds. *J. Geophys. Res.*, 103:28337–28346, 1998.